3-31-2006

Ignition delay of oxygenated fuel droplets: development of a 1 second drop tower and initial 1-g test results

Matthew Hammill
Rowan University

Ignition Delay of Oxygenated Fuel Droplets: Development of a 1 Second Drop Tower and Initial 1-g Test Results

Matthew Hammill

A THESIS

PRESENTED TO THE FACULTY

OF ROWAN UNIVERSITY

IN CANDIDACY FOR THE DEGREE

OF MASTER OF SCIENCE

RECOMMENDED FOR ACCEPTANCE

BY THE DEPARTMENT OF MECHANICAL ENGINEERING

COLLEGE OF ENGINEERING

March 2006

Ignition Delay of Oxygenated Fuel Droplets: Development of a 1 Second Drop Tower and Initial 1-g Test Results

Prepared by:

Matthew Hammill

Approved by:

Dr. Anthony J. Marchese
Rowan University
Thesis Advisor

Dr. John C. Chen
Rowan University
Chair, Dept. of Mechanical Engineering

Dr. Krishan K. Bhatia
Rowan University

Abstract

United States' dependency on petroleum fuels, much of it imported, has remained at the same level even as alternative fuels become more readily available to the consumer market. One alternative to petroleum based fuel is biodiesel. Biodiesel has been shown to have lower carbon monoxide, hydrocarbon, and particulate matter emissions than standard fuels, but show an increase in the formation of nitrous oxide gases. It has been theorized that several of the physical properties, which are governed by the chemical makeup of the fuel, have an adverse affect on NO_x production. But until that time when a thorough chemical kinetic mechanism is developed for biodiesel, a means in which to lower NO_x emissions will continue to elude the scientific community.

Unfortunately, the chemical makeup of most biodiesel fuels is very complex. Instead, surrogate fuels must be used which have similar chemical structure to biodiesel, but are simple enough to allow for the development of a detailed chemical kinetic mechanism. At this time, there has been relatively little research in the combustion of biodiesel surrogate fuels. One fuel which has been proposed as a surrogate fuel for biodiesel is methyl butyrate. A detailed chemical kinetic mechanism for methyl butyrate has recently been developed, but it has yet to be substantially validated due to the lack of experimental data available on methyl butyrate combustion. In the present study, droplet ignition delay times of methyl butyrate and methanol are investigated. A bench experiment, conducted in normal gravity, was constructed and used to determine the ignition delay times of each fuel. Normal gravity experiments were conducted on both the methanol and methyl butyrate fuels. The methanol ignition delay results showed significant scatter. However, the methyl butyrate data exhibits expected trends.

Experiments conducted in microgravity are expected to show higher repeatability. Accordingly, as part of this thesis, a drop tower facility was constructed in order to allow for testing in a microgravity environment. The microgravity environment is necessary to ensure that the experiments are spherically symmetric.

A numerical model for methanol was also used to run simulations under prescribed conditions. The numerical model was originally developed at Princeton University and has been used to model methanol, methanol/water, heptane and heptane/hexadecane droplet combustion. The ignition delay times gathered from each set of simulations was compared against the experimental data obtained in the lab.

Future work will entail incorporating the methyl butyrate mechanism into the droplet combustion model and comparing the model against the methyl butyrate experiments. By examining the ignition delay times of methyl butyrate under a range of temperatures and initial diameters, the chemical kinetic mechanism can be verified and, if possible, reduced in size. The overall goal is to determine a simplified chemical kinetic model that can be implemented into a CFD program which mimics the conditions present in a standard engine.

For my family

Acknowledgements

I would like to thank Dr. Anthony Marchese, my thesis advisor, for all of his help and for offering this project to me when I was unsure of how I was going to continue my education. I would also like to thank Tim Vaughn, my fellow graduate student on this project, for all of his help (especially when something needed to be built). Thanks as well to Dr. John Chen and Dr. Krishan Bhatia for reading this thesis and providing valuable feedback. I'd also like to thank the undergraduate students whom contributed to this project: Fred Bellottie, Colleen Boland, Scott Jurewicz, Justin Pusey, and Greg Soriano.

Special thanks go out to my parents, Kevin and Linda Hammill, for their support (and for the free room and board) while I finished my research, as well as the rest of my family who were always impressed even at times when I felt like the work was mundane and tedious (welcome to the real world, right?). Thanks go to Tom Smith, Jesse Cugliotta, and Dan Smith. Without them, I might have skipped out on continuing my education and gone straight to work. Thanks to all my friends, especially Jessica Morgan, who probably puts up with a lot of my quirkiness without complaint. Finally, I'd like to thank my officemates Doug Gabauer, Pete Niehoff, and the undergraduate, Jen Lake. The three of them helped make this experience more fun than it probably should have been.

Finally, I'd like to thank the Dr. Avedisian of Cornell University and graduate student Isaac Boxx of the University of Texas at Austin for their advice that guided us through the construction of our own drop tower. The work described in this thesis was

made possible by NSF Grant CTS-042084, and without it, none of this would have been possible.

Table of Contents

List of Figures

List of Tables

Chapter One

Introduction

Section 1.0 – Overview

In recent years, there have been advances in the area of alternative fuels, such as biodiesel, ethanol and others. While there is still much work to be done, the emergence of these fuels has created possibilities for decreasing our dependence on fossil fuels as our sole energy source. Since there is still more work to be done to prove the viability of alternative fuels, fossil fuels remain the main source of energy in the United States. Fossil fuels make up approximately 85% of all energy consumed in the US. This percentage has changed very little in the last decade, and it doesn't appear to be likely to change anytime soon. Petroleum fuel, in general, makes up roughly 40% of the total energy consumed, including a remarkable 97% of the total energy used by the transportation sector [1].

The major problem, of course, is that fossil fuels are a non-renewable source of energy, and if its use continues in this way, fossil fuel deposits will soon be depleted. Fossil fuels also release carbon dioxide into the atmosphere, which has been shown to be a greenhouse gas that most scientists believe is the major source of global warming. Renewable fuels, biodiesel release nearly no net carbon dioxide emissions since the plants from which they are derived were produced from carbon dioxide already in the atmosphere.

Biodiesel has been shown to reduce carbon monoxide (CO), hydrocarbons (HC) and particulate matter (PM) emissions from diesel engines. There is also added benefit in

that using biodiesel limits the country's reliance on imported petroleum products, while at the same time, creating new markets for agricultural products such as soybeans [2]. However, studies have shown that while decreasing the above emissions, the use of biodiesel promotes the release of nitrous oxide (NO_x) [3], as can be seen in Figure 1.1. While these observations have been made, it is still not fully understood as to why this increased NO_x production occurs. It is possible that the increased NO_x emissions can be a result of differences in the physical properties between biodiesel and petroleum diesel. Biodiesel has a higher boiling point than traditional diesel, which allows the fuel droplets in an engine penetrate further into the cylinder. This results in more fuel droplets in the premixed ignition process, bringing about more fuel consumption, which in turn results in an increase in heat release, which is instrumental in creating additional NO_x emissions [4,5].

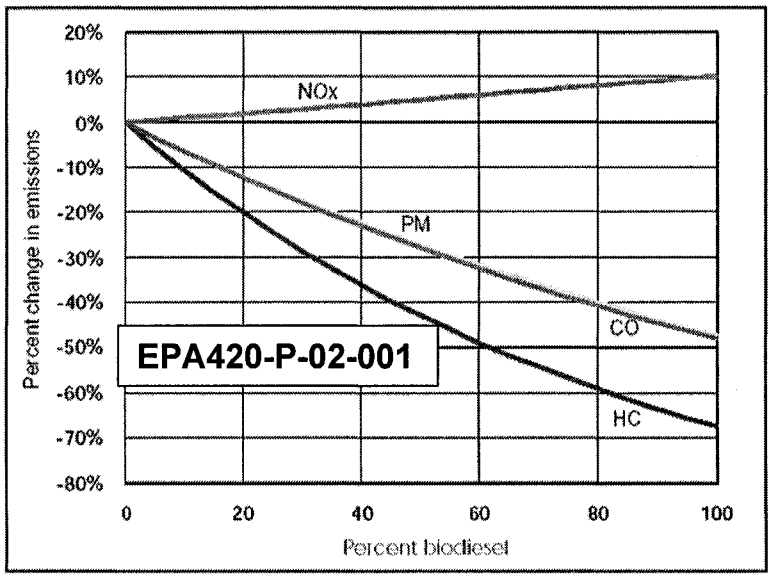

Figure 1.1: Reduction in emissions using biodiesel fuels.

Increased NO_x is also thought to be a result of the higher bulk modulus of biodiesel fuel and its effect on advancing fuel injection timing [6]. This advance in injection timing increases the time before the reaction is quenched by the volume expansion in the cylinder, thereby increasing both the reaction time and temperature, both of which promote NO_x production [7].

Besides these two mechanisms, there are differences in the chemical oxidation mechanisms between biodiesel and petroleum diesel which may either promote or retard NO_x production. However, both fuels are complex and contain a variety of chemical structures, which are difficult to analyze. As a result, there are no detailed chemical kinetic models for either biodiesel or petroleum diesel.

While it is still not yet possible to do a direct comparison between biodiesel and petroleum diesel, it is possible to compare several different biodiesel types to each other. McCormick and coworkers performed a comprehensive study to determine the effect of the chemical structure of various types of biodiesel on NO_x and PM emissions [8]. Specifically, they focused on the effects of carbon chain length and the number of double bonds on emissions. In their study, they used 21 different biodiesel fuels on a single diesel engine. Each fuel was produced from a different source material; 7 or which were produced from real-world feedstocks, and the other 14 from pure fatty acids. Engine dynamometer tests were performed on a 1991 Series 60 six cylinder, four stroke engine rated at 345 bph at 1800 RPM. Based on their observations, NO_x emissions decreased with increasing carbon chain length and decreasing number of double bonds.

The chemical structure of biodiesel fuels is very complicated, consisting of mixtures of saturated and unsaturated oxygenated methyl esters, containing carbon chains

15-20 or more atoms in length. As a result, NO_x production as a result of different chemical kinetics has received relatively little attention thus far. Instead of trying to determine the chemical kinetics of these complicated, long chained molecules, it is advantageous to identify surrogate fuels that contain features similar to that of biodiesel fuels. In that regard, Fisher and coworkers have proposed methyl butyrate ($nC_3H_7C(=O)OCH_3$), as a surrogate fuel. The group developed a detailed chemical kinetic mechanism consisting of 264 species and 1219 reversible reactions for methyl butyrate oxidation and compared it with the limited experimental data available [9].

More recently, Marchese and coworkers have taken the methyl butyrate chemical kinetic model developed by Fisher and coworkers and further tested the mechanism by performing methyl butyrate flow reactor experiments using the Princeton Variable Pressure Flow Reactor [10]. The group ran experiments at 12.5 Atm over a range of 500 to 900 K and equivalence ratio of 0.35 to 1.60. Results of these experiments show that the predicted fuel reactivity at stoichiometric conditions agreed well with experiments but the model either underpredicted the observed reactivity (fuel lean conditions) or overpredicted it (fuel rich conditions).

Along with the growing use of alternative fuels, there is another solution to decreasing the dependence on imported oil: increased efficiency of engines. Engines can be made more efficient through better design of a variety of systems, from fuel delivery to combustion to exhaust systems. Each of these areas can be addressed through a better understand combustion theory and application. Currently, the main argument for alternative fuels is the reduction of exhaust gas pollutants and greenhouse gases. The argument against alternative fuels is the maximum power output of the modified engines.

Fossil fuels, which produce higher levels of pollutants and greenhouse gases, also typically produce more horsepower than alternative fuels. In an effort to better understand the underlying processes of internal combustion, the vaporization and combustion of liquid droplet and sprays has been studied for more than 50 years the present work will use droplet combustion as a means of studying the combustion of biodiesel surrogate fuels [11].

So why study liquid droplets and sprays? In most vehicles, fuel is introduced into the combustion chambers (i.e., the pistons) as a spray from the fuel injection system. Depending on the type of engine, the fuel is either premixed with air prior to ignition (in spark ignition engines) or is ignited near the point of injection (diesel engines, jet engines, etc.). Both instances still mask the underlying processes, which include chemical reactions, thermodynamics considerations, and transport processes.

In order to fully understand the intricacies of combustion, as stated above, laboratory experiments must be conducted. Unfortunately, it is very difficult to study the exact setup and circumstances that are present in an internal combustion engine. This is due to the complexity of the actual spray process and the turbulent flow field. Accordingly, many researchers have employed experiments on a single, isolated fuel droplet as a means to better understand liquid combustion phenomena [12,13,14]. While this technique ignores the effects of fuel droplets interacting with one another, its advantages make this setup acceptable. In this setup, the single, isolated fuel droplet is considered to be spherically symmetric, which allows most of the underlying phenomena to be modeled in full detail using complex chemical kinetics and also allows for the development of simplified theoretical models. It is this setup that has served as a basis

for all tests run on fuel droplets, and is the basis for the droplet combustion theory [13,14].

In the present work, droplet ignition experiments were chosen as a means to test oxygenated fuel kinetic mechanisms. The overall goal of these experiments is to test the chemical kinetic mechanisms of these fuels, which have not been sufficiently tested under these conditions prior to the present work. Eventually, these fuels will be put into a CFD model of an engine; however, a detailed chemical kinetic model is too complex for current computers to handle in this setup. Therefore, a reduced chemical kinetic model that maintains the same ignition phenomenon must be developed.

This thesis is the result of experimental testing and modeling simulations run on oxygenated fuel droplets, including methanol and methyl butyrate. Methanol was chosen, because it is arguably the simplest oxygenated liquid fuel, a detailed validated chemical kinetic methanol mechanism currently exists and methanol also has been used as an alternative fuel. Methyl butyrate was chosen because it is a methyl ester (like biodiesel), but the hydrocarbon chain is short enough to permit the development of a detailed chemical mechanism.

The numerical model considers the spherically symmetric ideal case of methanol droplets; however, all initial experimental results were taken on a bench system and therefore deviate from spherical symmetry. Fuel droplets were injected into a tube furnace containing atmospheric air at temperature up to 950 C. The ignition event was characterized by measurement of UV emission from hydroxyl radical (OH*) chemiluminescence. As part of the work conducted for this thesis, a microgravity drop tower facility was constructed which will enable droplet combustion experiments to be

conducted with spherical symmetry. To date, microgravity experiments have yet to be completed. These tests will be the subject of a thesis that is currently under preparation by Vaughn [15]. The following section includes a review of droplet combustion theory and previous experimental results.

Section 1.1 – Droplet Combustion Theory

Combustion of a single, isolated droplet has long been studied and these studies have resulted in the formulation of numerous theories. The most well-known of these theories is the "classical" d^2-law for droplet combustion. First introduced as early as the 1950s, the d^2-law for droplet combustion has been continually modified in order to accurately predict physical phenomena. The original formulation [16,17] of the d^2-law begins with the assumption of a spherically symmetric droplet placed within an infinite oxidizing environment. This configuration results in fuel vaporizing at the droplet surface. While the vapor diffuses outward into the oxidizing environment, the oxidizer diffuses inward. At some point, the fuel and oxidizer will be in stoichiometric balance and react with each other, resulting in a flame. In the classical model, this reaction is assumed to be infinitely fast with respect to diffusion. The heat from the flame then travels both outward and inward. The outward bound heat is of little significance, since the environment is assumed to be infinite; however, the inward bound heat causes an increase of heat on the droplet surface, causing evaporation of the liquid droplet into a vapor state [11]. A schematic of this configuration can be seen in Figure 1.2.

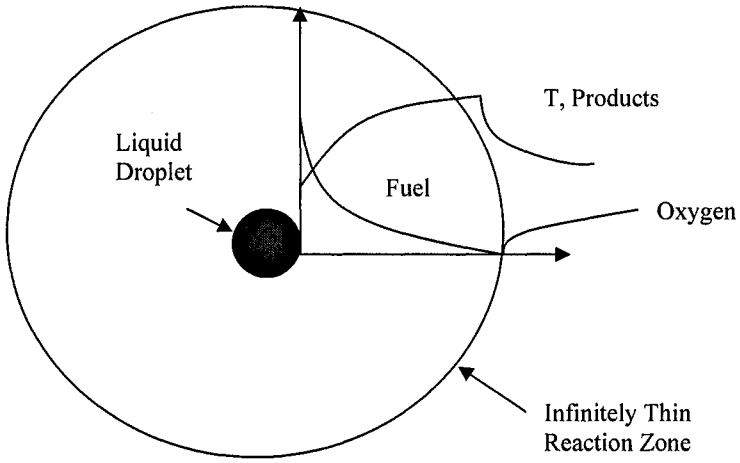

Figure 1.2: Classical d^2-law combustion model. [16,17]

However, there are limitations of the d^2-law. Most notably, the formulation cannot simultaneously predict the burning rate, flame position, and flame temperature. This is a result of the numerous assumptions that were made in the law's formulation. These assumptions are as follows [14]:

- Spherical Symmetry
- Isolated droplet in infinite medium
- Isobaric process
- Chemical reaction infinitely fast with respect to diffusion
- Constant gas phase transport properties and heat capacity
- Gas phase quasi-steadiness
- Constant, uniform droplet temperature (no droplet heating)
- Neglect Soret effect, Dufour effect and radiation
- Unity Lewis number for all gaseous species ($\rho_g D_{g,i}=\lambda_g/C_{p,g}$)
- Negligible buoyancy
- Negligible radiation

Despite all of the assumptions that are necessary for derivation of d^2-law, it has been repeatedly shown to be an extremely useful theory, at least qualitatively.

Quantitatively, however, it has been shown to have many limitations. The "classical" law predicts that the droplet burning rate, the flame stand-off position, and the flame temperature mean all remain constant throughout the entire burn. Physical evidence, however, disputes these claims. First, the droplet burning rate does not remain constant. Instead, the burning rate of the droplet at the onset of ignition is much lower than the d^2-law predicts, as evidenced by the small change in droplet size. The droplet burning rate is also affected by the extinction of the envelope diffusion flame. This has been noticed to occur at finite droplet diameters, and results in the rapid decrease of the droplet burning rate [18,19,20,21,22]. Finally, the flame stand-off ratio is not constant. Depending on the oxygen concentration of the ambient environment, the flame stand-off ratio varies with time. In the case of low oxygen concentration, the flame stand-off ratio continually increases, whereas in the presence of high oxygen concentrations, the stand-off ratio increases at the start, and then eventually reaches a constant value [21,23].

In order to resolve these issues, it is necessary to relax some of the d^2-law assumptions. Law, *et al.* [23,24] worked out the flame variation and the droplet heating problems by doing so while still assuming infinitely fast chemistry with respect to diffusion. By including initial transient heating of the fuel droplet, it is possible to account for the initial slower burning rate of the droplet. A simple energy balance conducted at the droplet surface verifies this conclusion.

$$Q_{cond,surface} = Q_{cond,inside} + Q_{vaporization} \tag{1.1}$$

Basically, the heat conducted to the surface of the liquid droplet is redirected in two different routes: heating the droplet, and vaporization. Initially, the droplet is relatively cool, and most of the heat conducted to the surface continues into the interior of

the droplet. Eventually, the droplet will be at a higher, uniform temperature, at which time the burning rate will increase due to the increased amount of fuel vapors that are formed. Note that the above equation neglects radiation. By relaxing another assumption of the d^2-law (negligible radiation), a radiation term can be added to the above equation. Obviously, radiation occurs in both directions, but generally, the radiation term would appear on the left side of the above equation. This is expected since it is assumed that the ambient environment is at a higher temperature than the fuel droplet itself.

The varying flame position can be accounted for based on the accumulation of fuel vapor between the droplet surface and the flame itself. The above energy balance formulation continues to affect the entire system. Since much of the heat is initially used to heat the droplet interior instead of vaporizing the liquid surface, there is very little fuel vapor in the immediate area. In order to stoichiometrically burn, therefore, the flame must be close to the droplet in order to have the right fuel-to-air ratio. However, once the flame establishes itself, the extra head added to the droplet surface results in faster vaporization, leading to an abundance of fuel vapor in the area between the flame and the droplet. In order to maintain a stoichiometric reaction, it is necessary for the flame position to move further from the droplet. As stated earlier, where the flame ultimately ends depends on the oxygen concentration of the ambient environment. To reiterate, a low oxygen concentration will result in the flame position continually moving out to infinity, whereas a high oxygen concentration will cause the flame position to eventually reach a quasi-steady position. These relaxations of the assumptions of the d^2-law can be seen in Figure 1.3.

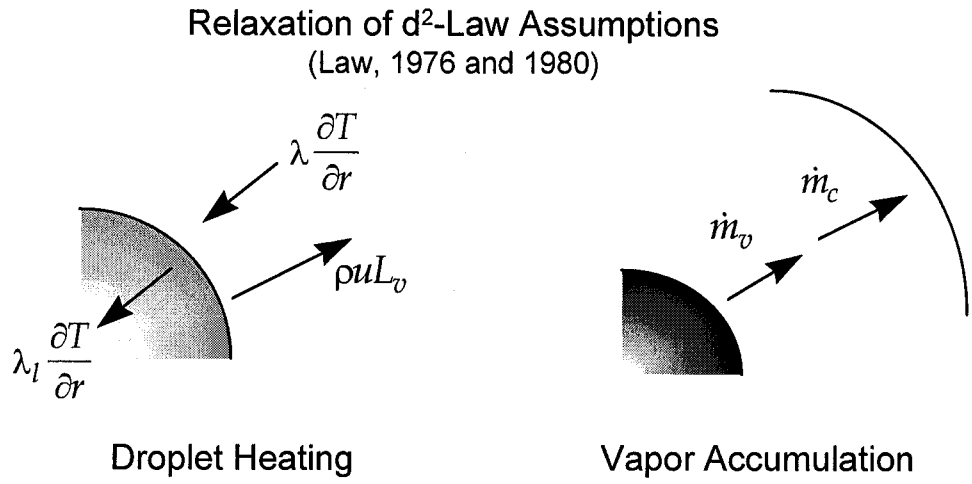

Figure 1.3: Relaxing the d^2-law assumptions. [11]

There is one final limitation of the "classical" d^2-law: the assumption of an infinitely fast chemical reaction. This assumption cannot predict the transient phenomena of droplet ignition and extinction; therefore, it is necessary to consider finite rate chemical kinetics, which has been studied in numerous ways. A single-step activation energy asymptotic analysis was used by Law [25,26]. By developing ignition and extinction criteria, it is possible to determine an entire family of steady state droplet combustion and vaporization solutions. There are also several methods that examine the effects of multi-step reduced chemistry and full detailed chemistry. And while studies using multi-step chemistry on n-heptane have not produced definitive conclusions [27], methanol, with its simpler, yet full, detailed mechanism retains sufficient detail with respect to the overall oxidation scheme [28,29].

This simpler mechanism is one of the reasons that methanol has been chosen to be numerically modeled in this current study. The full, detailed chemical kinetics should allow for accurate prediction of ignition delay times.

Section 1.2 – Droplet Combustion Experiments

1.2.1 – Droplet Combustion in Normal Gravity

One of the assumptions of the d^2-law is that the droplet and vapor are spherically symmetric. However, it is very difficult to achieve such a state experimentally. Due to the presence of buoyancy in normal gravity, the spherically symmetric assumption cannot be reached. Attempts have been made to achieve a state as close as possible to the spherically symmetric condition, but as will be seen, there are still problems with each experimental setup.

One of the earlier methods used involved a porous ceramic sphere hooked up to a fuel line. The line would continually feed the liquid into the center of the sphere, in an attempt to grow a droplet on the outside of the sphere. While this type of experiment was adequate in determining steady state concentrations and temperature profiles [30,31], the droplet never achieves spherical symmetry due to the presence of the fuel line. Buoyancy effects are still present as well, pulling the droplet away from a spherically symmetric state. Finally, since the fuel supply tube is constantly feeding fuel into the center of the sphere, the experiment will reach steady state. However, it has become apparent that a typical fuel droplet will never reach a steady state condition. Instead, its entire burn history will be affected by transient conditions.

In an effort to alleviate the steady state drawback and to take into consideration transient phenomenon, experiments run without a fuel supply line were conducted. By suspending a fuel droplet on the end of a fiber, the droplet would experience a fully transient burn history. Once again, however, the presence of the fiber and bead distort the droplet from a spherically symmetric state. The fiber also serves as a means of heat

loss via conduction. Buoyancy effects could also distort the droplet, but it has been shown that by simply reducing the ambient temperature, buoyancy effects can be reduced [18,23,32].

A third method in which to run droplet experiments involves allowing the droplet to be in free fall. Since the days of Galileo, it has been observed that as a droplet is released into free fall, the surface tension will allow the droplet to become closer to the shape of a sphere [33]. While in free fall, the droplet is ignited by passing by a hot wire, a heated stream, or some form of furnace. The obvious problem is that of convection. Convection effects increase as the relative velocity of the droplet increases. To reduce these effects, it is necessary to use small droplet sizes (on the order of 100 microns). This will reduce the convection effects nicely; however, it is difficult to get accurate droplet size data by this means due to the small droplet sizes and the short burn times that result [34]. These three methods can be seen in Figure 1.4.

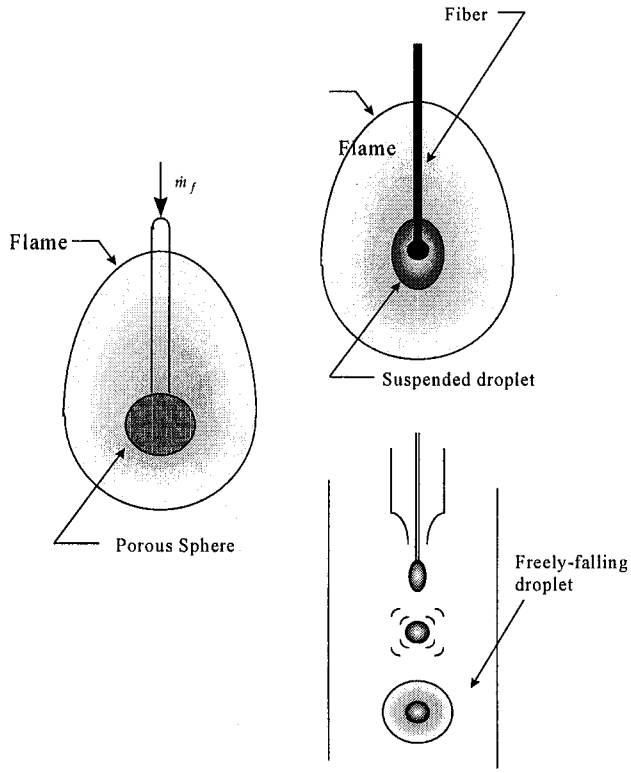

Figure 1.4: Classical droplet combustion experiments. [11]

The above sets of experiments are just a handful of attempts in classical droplet combustion experiments. However, it can be concluded that methods such as these are not the best solution. While each method can provide some amount of data, none of them can provide all the desired data. As the next section will discuss, there are conditions that can be met to reduce the effects of buoyancy, as well as other obstacles.

1.2.2 – Microgravity Considerations

In the above experiments, it was nearly impossible to produce a spherically symmetric liquid droplet. As a result, it wasn't feasible to compare the experimental data obtained to any theoretical or numerical model since most theories and models assume a

spherically symmetric system. There is also one other major problem with the previous experiments: all of them were under the influence of buoyancy. In a typical flame, large temperature gradients can appear over very small distances, and these temperature gradients result in density gradients. Density gradients in turn result in hydrodynamic flows, since the lighter material tends to rise and the denser material tends to fall. These flows obscure what is really happening to the liquid droplet, its vapor, and the flame around it. Therefore, it is necessary to achieve some level of microgravity, which will reduce the effects of buoyancy on the isolated droplet. A classical example of the difference in running an experiment in microgravity as opposed to normal gravity is the burning candle [34]. If you were to light a candle anywhere on earth, the flame would form the common cone shape and burn yellow, which everyone can recognize. However, if the same candle were burned in a very low gravity environment and lit with the same type of match, the resulting flame would no longer take the familiar cone shape. Instead, a blue flame in the shape of a hemisphere emerges. This phenomena can be seen in Figure 1.5.

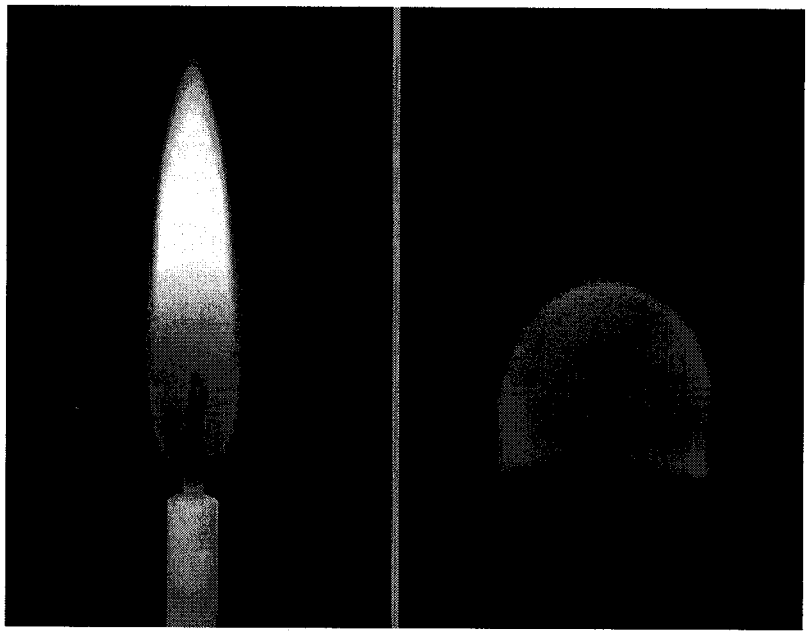

Figure 1.5: Buoyancy effect on candles.

Fortunately, it is possible to quantitatively identify the effects of buoyancy. To do this, it is necessary to think of the Grashof number as a comparison between a buoyant velocity and a diffusion velocity [35]. The resulting equation for the Grashof number is as follows:

$$Gr = \frac{(buoyant\ velocity)^2}{(diffusion\ velocity)^2} = \frac{(\Delta\rho / \rho)gL}{D_g^2 / L^2} = \frac{(\Delta\rho / \rho)gL^3}{D_g^2} \tag{1.2}$$

where $\Delta\rho$ is the characteristic density change, ρ is the mean density, L is the characteristic length scale, D_g is the mass diffusivity, and g is the acceleration due to gravity. In addition to the Grashof number, the Richardson number can be used as well. It also is a comparison with the buoyant velocity, but instead of the diffusion velocity, it is compared to the convection velocity. The Richardson number follows:

(1.3) $$Ri = \frac{(buoyant\ velocity)^2}{(convection\ velocity)^2} = \frac{(\Delta\rho / \rho)gL}{v^2}$$

Law and Faeth [35] concluded that to make the effects of buoyancy small, and therefore negligible, both the Grashof number and the Richardson number need to be on the order of 10^{-1}.

However, after additional calculations and considerations [11], it becomes apparent that the Grashof number is the parameter that determines spherical symmetry. For a 1 mm droplet, in order to achieve a Grashof number on the order of 10^{-1}, the gravity levels must be in the area of 10^{-4}. There are several methods in which to generate this low level of gravity. The most obvious case would be to run the experiments in Earth orbit. However, due to the high costs (and currently, lack of trips to space) this method is not the most feasible. Alternative methods include parabolic flight aircraft, drop towers, and sounding rockets. Of these three, the drop tower is the most feasible, due to the difficulty in running isolated droplet tests in sounding rockets, and the relatively high g-levels present while in an aircraft flying in parabolas. The following table compares all four methods based on microgravity level and test duration.

Table 1.1: Microgravity methods

Method	Gravity Level	Test Duration
Drop Tower	10^{-4} g – 10^{-6} g	1-10 s
Parabolic Flight Pattern	10^{-3} g – 10^{-4} g	5-15 s
Sounding Rockets	10^{-4} g	200-900 s
Orbiting Spacecraft	10^{-5} g	1000-10000 s

As can be seen, putting the experiment into orbit provides not only the lowest gravity levels, but the longest test times. On the other end, drop towers have the shortest run times, but due to convenience, they are the most widely used method. A drop tower

is a facility that is designed to provide microgravity conditions by dropping an object into free fall at the top of the structure and recovering said object at the bottom. There exist many drop towers in the world, each of them unique in one aspect or another. The following table compares a sample of drop towers [36,37,38,39,40,19].

Table 1.2: Comparison of various drop towers.

Drop Tower	**JAMIC**	**Toki City**	**ZARM**	**NASA GRC**	**Univ. of Texas**	**Cornell Univ.**
Location	Hokkaido, Japan	Toki City, Japan	Bremen, Germany	Cleveland, Ohio	Austin, Texas	Ithaca, New York
Height	500 m	100 m	110 m	29.5 m	9.5 m	10 m
Test Duration	10 s	4.5 s	4.75 s	2.2 s	1.1 s	1.2 s
g-level	10^{-5}	10^{-5}	10^{-5}	10^{-4}	10^{-4}	10^{-4}

The next section provides summaries of previous studies done on various drop towers, including some of the above listed towers.

1.2.3 – Microgravity Experiments

As was stated above, the best two methods in which to run microgravity experiments are the drop tower setup and the space-based missions. These scenarios allow for the valid assumption of a spherically symmetric fuel droplet and boundary layer, which in turn allow for the comparison of experimental data to numerical calculations.

Kumagai, *et al.* [42], performed their tests by growing a liquid fuel droplet onto the end of a fiber. This fiber was then quickly retracted, deploying the droplet prior to the entire chamber being released into free fall. At roughly the same time, a single spark positioned beneath the droplet is used to ignite the droplet, also before the chamber is released.

Over the years, many ways of successfully producing liquid droplets have emerged, all of which can fall under one of two categories: fiber-supported droplets and free-falling droplets. Ideally, the use of a free-isolated droplet is desired, since the addition of a fiber can change the physical properties of the entire system. Depending on the situation, however, it can be easier to implement a fiber supported system. Green and coworkers devised a means to produce mono-disperse fuel droplets [43]. The basic function of this aerodynamic device is as follows: the liquid fuel flows through a capillary tube, which in turn is surrounded by an outer concentric in which gas flows through. The fuel is forced through the capillary tube via a metering pump, while the gas flow is produced by a flow controller. The gas flow is the most important aspect of the entire system, as the velocity of the gas has a direct impact on the droplet size, velocity, and intervals at which they are produced. Essentially, the moving gas grabs a hold of the fuel in the capillary tube, and once its force is great enough, the droplet is released into free fall. While very near the capillary tube, the newly released droplet is deformed and oscillating, its surface tension will cause it to take the shape of a sphere in time to run the experiments.

Avedisian, *et al.* [19], developed a means to accurately and repeatedly produce droplets in free fall. The device used to generate the droplets consists of a piezoelectric transducer attached to a glass nozzle. By applying a specified voltage to the transducer, a droplet or stream of droplets would be ejected through the nozzle. Each droplet is fired upward at a prescribed angle. Knowing the angle and the initial velocity of the droplets allows for the calculation of the apex of the droplet's trajectory. At that time, the entire experiment is released into free fall, allowing the droplet to experience as much

microgravity as possible. Since the droplet's vertical velocity is zero at the apex, it is possible to keep the droplet in the camera's field of view. Alternatively, Jackson and Avedisian [44] used the same basic setup, but instead introduced a fiber located at the approximate location of the droplet's apex, thereby catching the droplet and maintaining it in the field of view of the camera. Avedisian, *et al.*, investigated heptane and toluene droplets to varying degrees of success. The heptane droplet clearly showed evidence of flame extinction; however, the toluene droplets were less clear. Both fuels, however, produce soot, which had previously been thought to bring about flame extinction earlier by suffocating the droplet.

Jackson and Avedisian investigated the effect of soot formation on burning rate. Previously, a value of 0.78 mm^2/s had been assumed to be the benchmark figure for the burning rate of n-heptane in air [45]. However, Jackson and Avedisian, using both freely falling droplets and fiber supported droplets, found that the burning rates of n-heptane were substantially lower than the previous benchmark value. In fact, for droplet sizes above 0.6 mm, they saw a 20% decrease in the burning rate. Their work agreed well with work done on the subject just a few years earlier by Choi, *et al.* [45]. In that study, Choi, *et al.*, changed the typical setup of the droplet experiment. Instead of growing and deploying the fuel droplet before the free fall period, they did so while already in free fall. This cut the total experiment run time roughly in half, but by using the 2.2 Second Drop Tower at NASA LeRC, this did not result in any loss of information. It was in this experiment that the traditional value of 0.78 mm^2/s for the burning rate of n-heptane was discovered to be too high. The group found that burning rates as low as 0.50 mm^2/s resulted. To explain this, Choi and coworkers hypothesized that the soot formation was

the primary cause. Many studies have been conducted investigating the effect of soot formation on droplets in microgravity [46,47,48,49,50].

Despite the abundance of fuel droplet studies, relatively little has been done with oxygenated fuels such as methanol. It wasn't really until the last 15 years that studies have focused on oxygenated fuels (see section 1.0 for an overview). Held and Dryer [51] investigated the oxidation of methanol over a wide range of temperatures and pressures. Their tests run at atmospheric pressure agreed well with the limited amount of data available on methanol, but it was the first time that methanol experiments were run under higher pressures, upward of 20 atmospheres. The group also successfully developed a computational method to predict the experimental data.

Several space-based, and earth-based, observations were made by Marchese, *et al.* [52]. The group investigated the characteristics of n-alkanes and methanol. By slightly modifying the chemical kinetic models of n-heptane and n-hexadecane, a better representation of the experimental data was found. The numerical modeling agreed well with the experimental data of tests run on drop towers. Larger droplets were possible on board space shuttle missions STS-73 (November, 1995), STS-83 (April 1997), and STS-94 (July 1997). With the introduction of a slightly more complicated theory of chemical kinetics, the computed flame diameters determined by the team were much closer to those found experimentally. The team also found that the effect of radiative loss for n-heptane and methanol combustion becomes significant for droplet sizes greater than 1.0 mm.

The first droplet ignition experiments were conducted by Faeth and Olson [41], and the current study is very similar. In their work, major assumptions used in previous

models were investigated. A comparison between constant properties and variable properties showed that the assumption of constant properties can have a large error associated with it. Therefore, Faeth and Olson used variable properties in their model. Secondly, the assumption of a uniform, time-dependent temperature of the droplet was questioned. They compared this temperature profile to that of a radial and time-dependent temperature profile. The results of this analysis were inconclusive, as the uniform temperature assumption showed large errors when the droplet size was large, but smaller errors with decreasing droplet size. Faeth and Olson ran their experiment in an air-tight chamber that was released into free fall. The experiment itself was enclosed within the chamber, greatly reducing the effects of convection. In the experiment, a fuel droplet was suspended on a glass filament via a hypodermic syringe and the hot ambient environment was produced by a movable cylindrical furnace cup. Tests were run on iso-octane to determine the effect of droplet size, furnace temperature, and pressure inside the chamber. These tests agreed well with their model.

Section 1.3 – Thesis Organization

This thesis presents the results of numerical modeling and experimentation of oxygenated fuel droplets. In Chapter 2, the new 1 Second Drop Tower located in Rowan Hall is described. Also described is the drop rig, based off of NASA size specifications, that was also developed at Rowan University.

Chapter 3 describes the bench-top system used to gather preliminary data on the ignition delay of methanol and methyl butyrate fuel droplets. Also included in Chapter 3 are the results of tests conducted on the two fuels at various sizes and temperatures. All

tests in this chapter are run at atmospheric conditions (i.e., pressure, gravity levels). These experiments do not allow for the accurate assumption of a spherically symmetric system, but provide a baseline for further tests, as well as a means to coordinate all aspects of the experiment without continually dropping the rig from the 1 Second Drop Tower.

Chapter 4 introduces the numerical modeling used to determine the ignition delay time of a freely floating methanol fuel droplet located inside a furnace of ambient temperature. The numerical modeling assumes a low gravity environment in which the droplet is burning. Buoyancy and convection effects are negligible, and simulations are run neglecting and including radiation effects. Also in Chapter 4 are the results of a series of simulations on a methanol droplet of various sizes under varying conditions of ambient temperature, droplet emissivity, and furnace emissivity.

Chapter 5 compares the results of the numerical modeling with that of the methanol experiments. Also included are conclusions that can be drawn from the current study and future plans, including the move of the bench-top system to a microgravity system to be used in the 1 Second Drop Tower.

Chapter Two

Development of the 1 Second Drop Tower

Section 2.0 – Overview

In order to create a microgravity simulation on Earth, two methods exist. One such method is the employment of the KC-135 Weightless Wonder. This plane, operated by NASA and flown out of Johnson Space Center in Houston, offers around 30 seconds of microgravity conditions as the plane flies in a parabolic pattern. This amount of time in microgravity is more than sufficient for the time of interest studied in this thesis. However, the availability of the KC-135 is limited. Travel to and from the testing facility also is a problem.

An alternative to this method is the drop tower. A drop tower is a facility designed to allow for an object to be released into free fall for a period of time. During this time, the object experiences microgravity conditions. The following is a simple schematic of the drop tower located at the University of Texas at Austin [40].

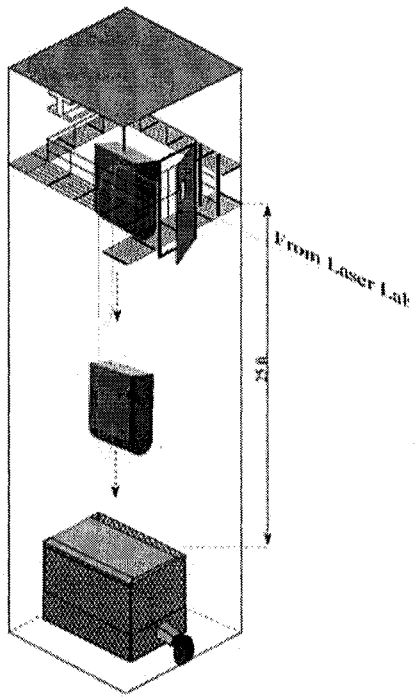

Figure 2.1: Simple schematic of the drop tower at the University of Texas at Austin [40].

There are numerous drop towers operating all over the world, and while they are more readily available than the KC-135, setting up days in which to run experiments can still be troublesome. To accommodate researchers in the New Jersey, Pennsylvania and Delaware Region, a new drop tower has been constructed on site at Rowan University. This facility will increase the availability to microgravity greatly by providing up to 1 second of microgravity time to conduct the experiments on combustion and fluid mechanics. As is the case in most open-ended problems, there are an infinite number of possibilities and ideas that could be used in the fabrication of a drop tower. Hence, there were initially numerous different approaches that were investigated before a final decision on its design was agreed upon. Several outside sources influenced the final design of the Rowan University 1-second Drop Tower, most notably the drop towers

located at NASA GRC [39], Cornell University [19], and the University of Texas at Austin [40]. The Rowan University 1-Second Drop Tower is, in essence, a hybrid of the three towers listed above.

Early in the design process, the drop tower was divided into two separate systems, and each system contained its own set of problems to overcome. These two systems are the hoist/release mechanism, which is responsible for raising the drop rig to its initial position and then releasing it smoothly, and the deceleration device, responsible for the safe landing of the rig. In the final design, these two systems are entirely separate from each other, although their design must be performed in concert because of the physics of free fall.. Essentially, any change in the total height difference between the bottom of the release mechanism and the top of the deceleration device has an effect on the velocity of the rig just before it hits the deceleration device, as well as the amount of time spent in free fall (see Figure 2.2). The goal is to have the drop rig in a state of free fall for as much time as possible, thereby increasing the amount of time that a microgravity experiment onboard could have to run. Both of these systems will be looked at in closer detail in the following sections. Appendix A contains detailed calculations that were performed in support of the drop tower design.

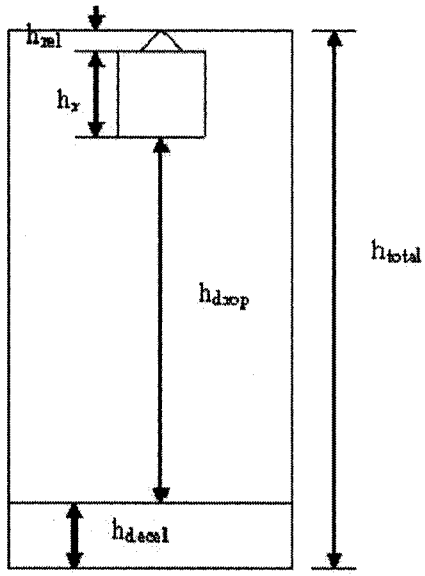

Figure 2.2: Basic representation of the drop tower.

Section 2.1 – Hoist/Release Mechanism

Since the final design of the deceleration device is dependant on the amount of time spent in free fall, which in turn is affected by the design of the hoist/release mechanism, it was decided to investigate the hoist/release mechanism first. Numerous ideas were evaluated for their effectiveness and ease of manufacture and installation. The first idea that was accepted and later installed is described below.

The ceiling of the High Bay Laboratory in Rowan Hall (the laboratory which houses the drop tower) contains a series of exposed structural I-Beams. The hoist/release mechanism design called for two additional I-beams to be placed across the span of adjacent structural I-beams. For ease of installation, the smallest span possible was used as a basis thereby limiting the weight of the additional I-beams so that they could be installed by one or two people. The span was a mere two-and-a-half feet wide. Two W4x13 I-beams were purchased to span the gap between the structural I-beams. In an

effort to maximize the drop height, steel risers were welded to the bottoms of the W4x13 I-beams. Attached to the undersides of the I-beams were two flat mount block pulleys (4 in. O.D., Tuf-Tug model SB3000FM). These pulleys can support up to 3000 pounds on a wire rope of 3/8 in. maximum diameter. The support structure can be seen in Figure 2.3.

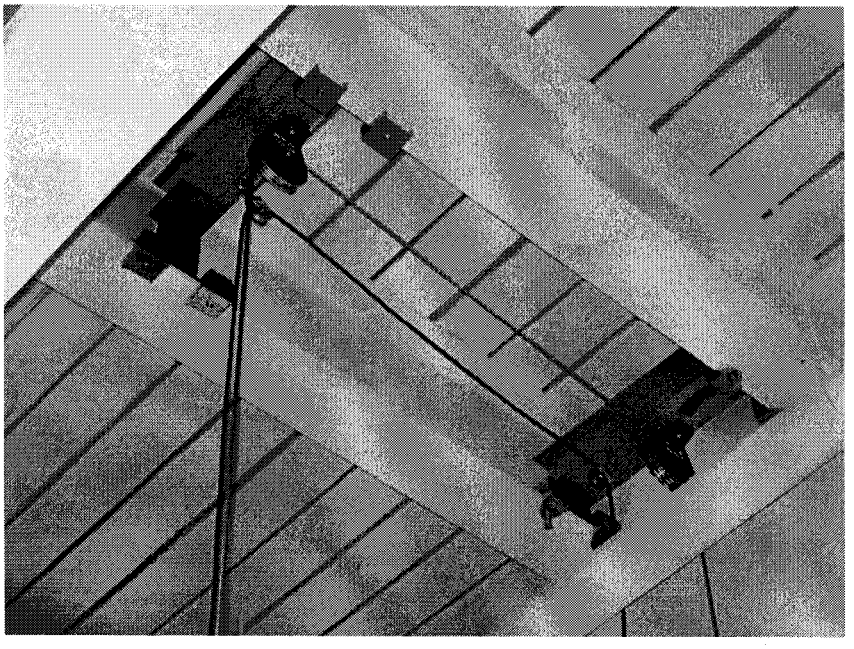

Figure 2.3: Original design for the support structure of the hoist/release mechanism.

There are two active parts of the hoist/release mechanism, the electromagnet and the electric winch. These two components act in conjunction to raise the rig and release it into free fall. The electromagnet (Magnetech Corp. model # R-6030-24, Figure 2.4) is rated to hold up to 1700 pounds; however, that value is drastically reduced when using the electromagnet in a lifting role. Safety standards recommended by the company indicate that the safe lifting capacity of the magnet is only one-quarter of the total holding

capacity. In the case of the R-6030-24 electromagnet, this limits the lifting capacity at approximately 425 pounds.

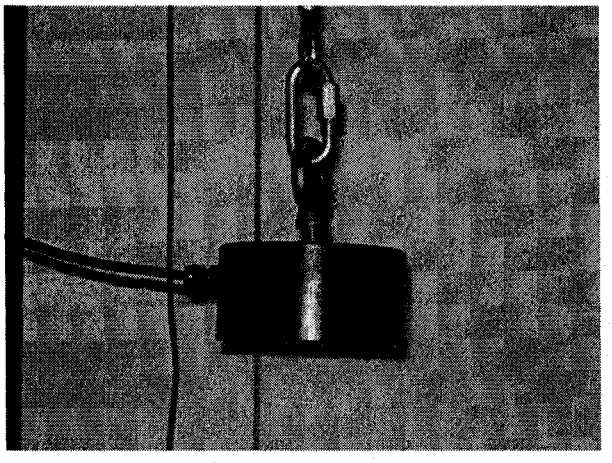

Figure 2.4: Magnetech Corp. #R-6030-24 electromagnet.

The electromagnet is attached to a steel cable, which is raised and lowered using an electric winch (Superwinch model AC2000). This winch has a maximum line pull of 2000 pounds and the steel cable is 5/16" in diameter and 100' long. The winch operates on 115/230 V at 60 Hz and can be controlled by a switch located on a separate controller. In order for the winch to be able to lift up to 2000 pounds, it must be securely fastened to a heavier object or structure. However, the drop rig, which will be discussed in the next chapter, weighs significantly less. Therefore, the winch was attached to the cage that encloses the deceleration mechanism (Figure 2.5), as will be discussed in the next section.

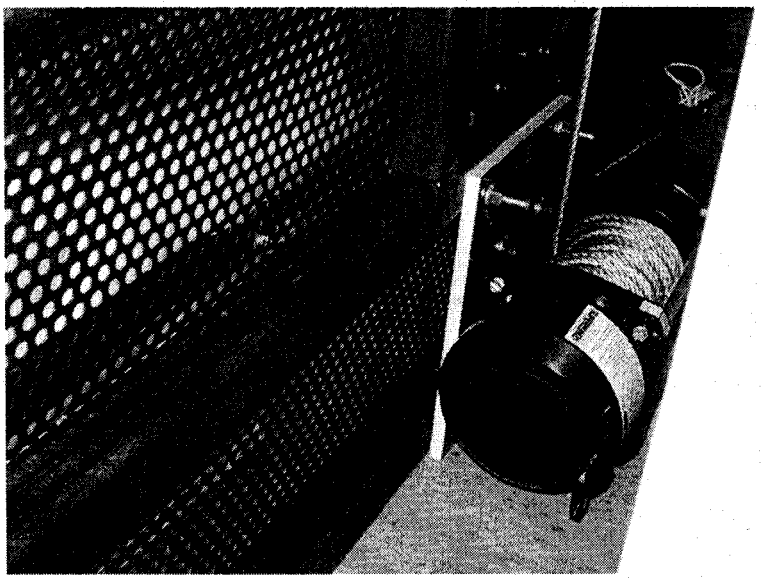

Figure 2.5: Electric winch attached to the deceleration cage.

The hoist/release mechanism is operated as follows. First, the electromagnet is turned on and attached to the top of the drop rig, which contains a ferrous "button" with a ground surface finish to which the electromagnet attaches. Then, the winch is activated, lifting the electromagnet and the rig to the top of the drop tower via the two pulleys. Once there, the entire package is steadied, at which point the power to the electromagnet is cut, releasing the rig into free fall. In order to ensure the rig is not destroyed upon impact with the bottom, a deceleration device is placed under it and is discussed in Section 2.2.

Section 2.2 – Deceleration Device

The purpose of the deceleration device is to slow down and ultimately stop the drop rig. The goal in the design stage was to develop a means of doing so that would

enable the use of drop rigs that adhere to the NASA 2.2-second drop tower standards. To ensure the safety of all equipment on board the drop rig as it falls, the maximum sustained g levels that can be experienced by a NASA standard drop rig during deceleration must not exceed 30 g's. Several methods exist already on numerous drop towers, including an air bag systems and beds of Styrofoam cubes. There are other possibilities that aren't in use, as well, but for various reasons, they have largely been avoided. The above two systems are simple and the decision was made to investigate them further.

Upon consulting with others that had previously worked on developing drop towers, it was decided that an air bag system was the best start for the Rowan University Drop Tower. The bed of Styrofoam cubes was determined to be difficult to properly set up for each test run, whereas all that is needed to set up an air bag is an industrial blower. With the decision to use an air bag system, it was now possible to construct the entire deceleration device.

The air bag is contained within a large cage, constructed out of steel, which is both welded and bolted together. The steel cage itself measures 5'x5'x5', encompassing 125 ft^3 of space. Barn doors on the front of the cage allow for access of the air bag or drop rig. Inside the cage, covering the top 4 feet, is a veneer of perforated sheet metal. The reasoning behind the sheet metal is two-fold: to contain the air bag within the cage itself, and to protect the air bag from any sharp edges left over from cutting and welding the steel members. The airbag was manufactured by DS Sewing, a company that makes covers for truck beds and boats. The air bag is composed of 22 ounce nylon-coated polyester, making it strong enough to withstand the force of impact from the drop rig.

The maximum (inflated) dimensions of the air bag are 5'x5'x4', which is one foot shorter than the actual cage. This is a result of the desire to install a polyurethane foam mat at the base of the air bag in order to guarantee a soft landing for the drop rig. This 12" thick foam mat (US GymMats Model TM12-NF-55) ensures that even if the drop rig isn't completely stopped by the air bag, it would not come into contact with the floor of the High Bay, possibly causing damage to the rig or the components onboard.

In order for the air bag to do its job, there must be a means in which air inside it could escape as the drop rig comes into contact with the air bag. On each side of the rig, located above the foam mat and centered on each side, is a blast gate. These blast gates serve as the inlet/outlet of the air bag; filling it before the run, and allowing it to deflate to accommodate the drop rig. Of the four blast gates, three act as an outlet for air, while the fourth serves as an inlet to inflate the air bag. Each blast gate contains a PVC swing check valve (with the exception of the inlet gate) and a PVC flange. The 6" PVC swing check valves (US Plastics Model 20439) are rated up to 150 psi, with a minimum cracking pressure of 5 psi. In between these two components is a steel plate, dimensions 9"x9"x1/2", which is welded directly to the steel cage. The check valves are placed on the outside of the cage, while the flanges are placed inside. The air bag contains four sleeves, and each one of these is attached to each flange via a hose clamp, ensuring a tight seal. The check valve subsystem can be seen in Figure 2.6, while the entire cage system is shown in Figure 2.7.

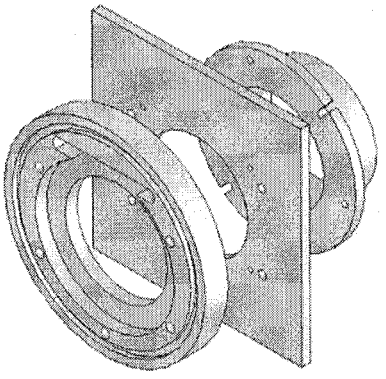

Figure 2.6: Check valve subsystem. The swing check valve is on the left and the flange is on the right. In between is the steel plate used to mount the two together. The airbag sleeve fits over the back of the flange.

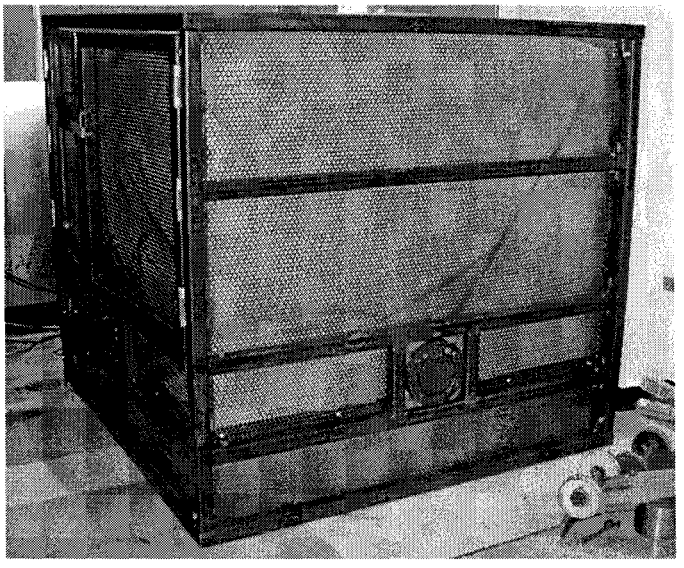

Figure 2.7: Deceleration cage with polyurethane foam mat and inflated air bag. Swing check valves are also present.

The final component of the deceleration device is the radial blower (Figure 2.8). This 1.5 hp regenerative radial blower (Ametek DR454R58A) can generate air flow of 127 CFM running on 110/220 V AC. The maximum pressure it can generate is 2.348 psi. The blower is connected directly to the inlet check valve.

Figure 2.8: 1.5 hp regenerative radial blower.

Section 2.3 – Drop Rig

Perhaps the most important part of the drop tower, the drop rig contains the actual experiment to be conducted in the microgravity environment. Originally, the plan was to get a drop rig on loan from NASA GRC. This way, once the experiment was setup, it could easily be moved to the 2.2 second drop tower located at NASA GRC in order to run the droplet ignition delay tests for a longer period of free fall. However, due to the unavailability of a suitable empty drop rig, it was decided to build a new drop rig to the same size and weight specifications as those used in the NASA 2.2 Second Drop Tower.

Constructed from pre-manufactured extruded components by Minitec Framing, the Rowan University drop rig adheres to the size constraints of the NASA GRC drop rig,

but is not exactly the same. Using a basic rectangular prism shape, the rig measures 38"x16"x33". Additional pieces of framing were used to create two "shelves" to which the experiment and other peripherals can be secured. On one of these shelves, there are two machined aluminum plates with ¼ x 20 tapped holes equally spaced apart. This shelf will be where the main experimental setup is located, whereas the second shelf will be used for any additional peripherals that are required to ensure the experiment runs smoothly. Figure 2.9 shows the completed drop rig prior to installation of the microgravity droplet ignition experiment (See Chapter 3) within its confines.

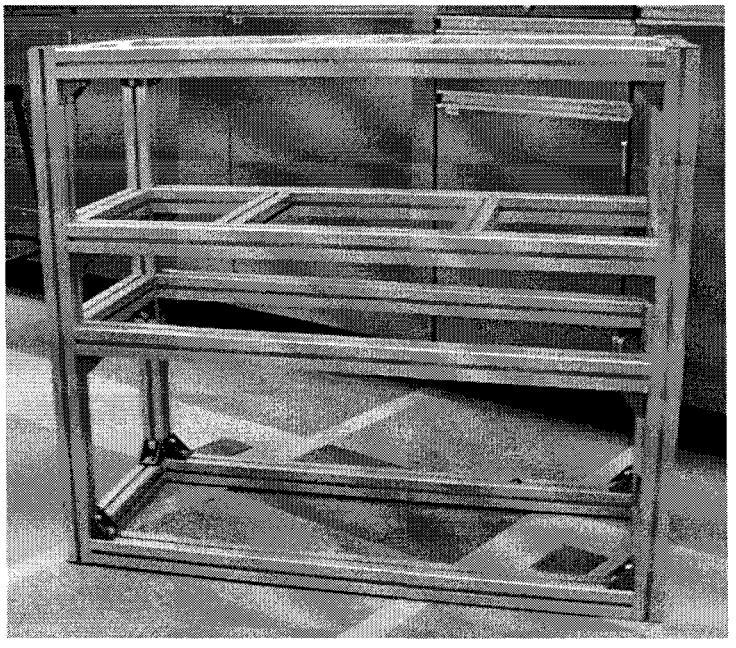

Figure 2.9: Rowan drop rig ("shelves" not present).

Chapter Three

Ignition Delay Experiments

Section 3.0 – Overview

The Drop Tower discussed in the previous chapter is just a part of the experimental apparatus. Its purpose is to simulate microgravity conditions in order for the assumption of a spherically symmetric droplet ignition event to be valid. The overall experiment produces hot ambient air around a liquid fuel droplet. Measurements are taken on the initial diameter of the droplet, as well as the ignition delay associated with it. Before conducting experiments in microgravity, it was necessary to develop and test the entire droplet ignition experiment and to conduct a series of experiments in normal gravity using this experiment. The following section describes the droplet ignition delay experimental setup in normal gravity configuration.

Section 3.1 – Droplet Ignition Delay Experiment in Normal Gravity Configuration

The normal gravity droplet ignition experiment set up developed as part of this thesis is nearly identical to the actual microgravity experimental setup. The purpose of the normal gravity experiments were to develop experience in conducting droplet ignition experiments and to be able to compare 1-g experiments with the future microgravity experiments to determine the role of gravity in droplet ignition. The main difference between the normal and microgravity configurations will be associated with the fact that the microgravity experiment will be more contained; that is, all power supplies will be on board the drop rig alongside the experiments. The normal gravity set up had no such

constraint. Another big difference between the two configurations is the methods of droplet generation and insertion. This difference will be discussed further below. There are several independent systems in the normal gravity setup: the furnace apparatus, the droplet generation/injection mechanism, and the data acquisition system.

3.1.1 – The Furnace Apparatus

The central object in the entire experiment, aside from the liquid fuel droplet, is the furnace that will be used to generate the hot ambient air. The ATS Series 3210 Split Type furnace, is a tube furnace that has a temperature range of up to 1000°C. The furnace is heated by the use of Nichrome wires, which heat up when a current is passed through them. The resistive heating is directly proportional to the amount of voltage, but simply plugging the furnace into an outlet will result in the maximum voltage at all times. One of the variables in these experiments is the initial ambient temperature, so it is desirable to control the amount of voltage running through the wire in order to maintain a specific temperature. In that regard, an Omega CN-132 temperature controller was used to regulate the voltage input. Design of the furnace control system circuit is described in Vaughn [15].

The stock version of the furnace has two hemispherical insulators on each end which block the escape of heat through the furnace's two main openings. However, since it is of interest to see inside the furnace while the experiment is running, one of these insulators has been removed, and a sapphire window (manufactured by CVI optics) has been inserted in their place. These sapphire windows are mounted with an aluminum holder, constructed at Rowan University for this purpose. The tube furnace is shown in Figure 3.1 and the temperature controller is shown in Figure 3.2.

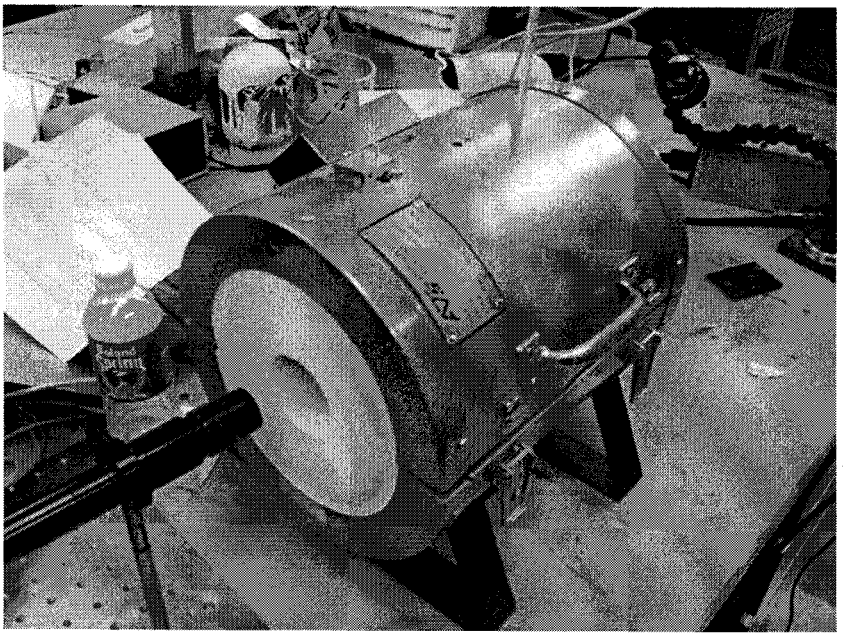

Figure 3.1: ATS Series 3210 Split Type Furnace (shown without sapphire windows).

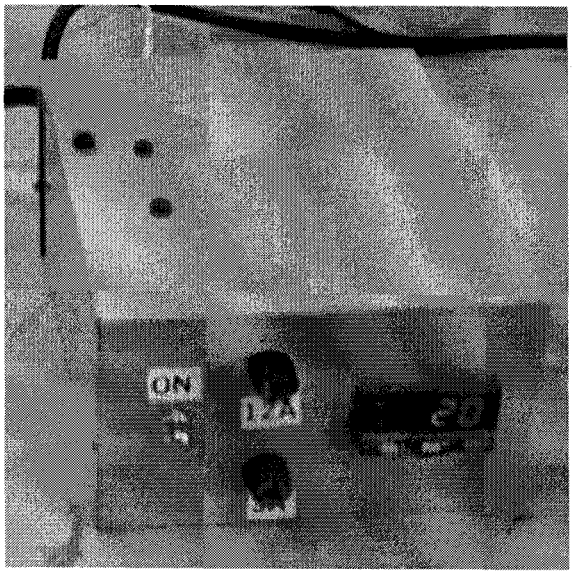

Figure 3.2: The Omega CN-132 Temperature Controller.

3.1.2 – Droplet Generation/Insertion Mechanism

As previously mentioned, this component of the normal gravity experimental setup will vary from the microgravity setup. The reason for this is simplicity. With the normal gravity system, it is much easier to manually implement these mechanisms, whereas on the drop rig during free fall, nearly all of the process must be automated. The normal gravity system is currently being automated in preparation for the microgravity tests, but in all experiments reported herein the droplets were deployed and inserted into the furnace manually. The obvious drawback to using a manual system instead of an automated system is repeatability. It is very difficult to manually replicate the same droplet diameters and insertion velocities between each experiment. The variation in initial droplet diameter is not too problematic since we can accurately measure the initial droplet. It is, however, an inconvenience when interpreting the experimental results, since it is difficult to generate a set of experiments with various furnace temperature and identical droplet diameter. The variation in insertion velocity may introduce some experimental uncertainty since the initial vaporization and diffusion of the fuel vapor surrounding the droplet is likely to be a strong function of the insertion velocity.

Manually generating a droplet requires patience and, mostly, time. In the current method of droplet generation, a syringe is used to hang a droplet on a fiber. In the future microgravity experiments, the liquid fuel droplets will be in unsupported free fall along with the entire drop rig. However, since the bench system will be run in normal gravity as opposed to microgravity conditions, it is necessary to implement a fiber supported system. In this system, droplets ranging from 0.5 to 3 mm are manually grown and placed on silicon carbide (high Nicalon) fibers approximately 10 to 14 μm using a 10 μL

hypodermic syringe. Each fiber contains a small epoxy bead. The purpose behind the epoxy bead is to provide a surface to which the liquid fuel droplet will attach, so that the droplet does not migrate along the fiber. Unfortunately, when employing epoxy for this purpose, each fiber can only be used once due to the fact that epoxy is flammable. Once the liquid fuel droplet evaporates or ignites, the epoxy is quick to ignite. Other methods of supporting the droplet are being investigated.

An injection fork is used to inject the grown droplet into the furnace. Each prong of the injection fork has an Allen screw on its end with two washers. Before the droplet is grown and placed on the bead, the fiber is gently stretched between the two washers on the two prongs. The screw is then tightened, but not overly so, to ensure that the fiber is locked into place. The forks are attached to a slider on ball bearings so that it can be introduced into the furnace at the same depth every time. The forks can be seen in Figure 3.3. The injection forks are manually injected into the furnace for each experiment.

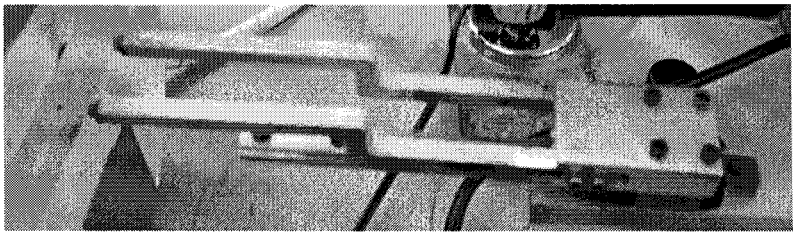

Figure 3.3: Insertion forks.

3.1.3 – Data Acquisition System

The data of interest in this experiment is ultimately the ignition delay time of each scenario. However, these experiments require the acquisition of a variety of data to

accurately analyze the results. Variables of interest include the initial diameter of the liquid fuel droplet, the ambient temperature of the tube furnace, and the moment of fuel droplet ignition. Each of these variables requires a different instrument.

The simplest of the above variables to determine is the ambient temperature inside the tube furnace. The Omega CN-132 temperature controller contains a digital display of the temperature inside the furnace. However, due to the fact that the thermocouple in control of the CN-132 temperature controller is located near the wall of the furnace, a correction factor is needed to account for any temperature gradient inside the furnace. This correction factor is discussed in the Experimental Results section below.

The second variable of interest is the initial diameter of the liquid fuel droplet. It is not enough to simply place a ruler or some other crude measuring device next to the droplet once it has been grown and placed onto the fiber. Measuring the diameter this way is inaccurate and adds to the time between generation and insertion, which is desired to be as low as possible to ensure that there is very little evaporation of the droplet before insertion. Instead, a Hitachi KP-D50 CCD camera records color, back-lit images of the droplet. However, the normal lens on the Hitachi camera doesn't allow for any enlarging; therefore, a zoom lens is needed. The Infinity KC IF-2 zoom lens has been attached to the Hitachi camera in order to enlarge the droplet image. A reference object must also be in the camera's view so that when the video is analyzed using the Spotlight software developed by NASA, a pixel to millimeter ratio can be determined. The Hitachi camera can be seen in Figure 3.4.

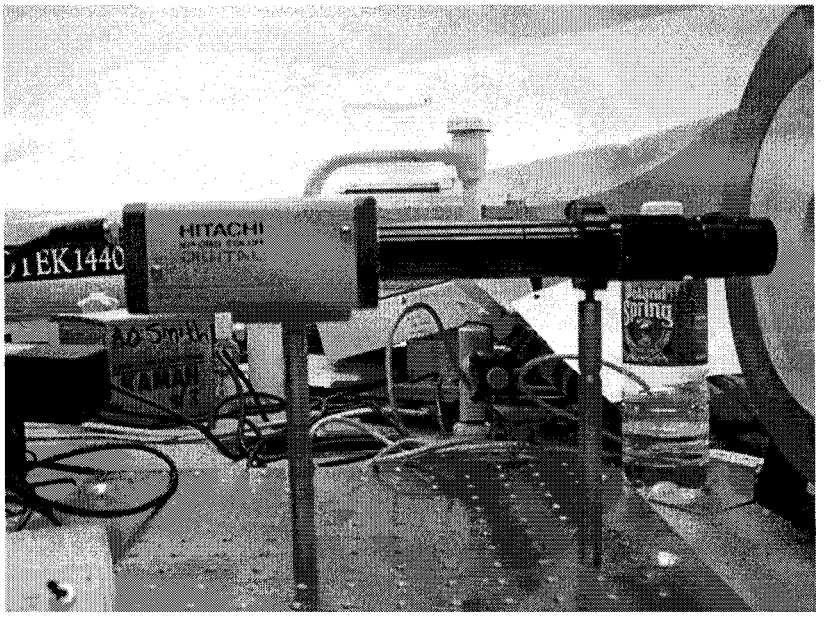

Figure 3.4: Hitachi KP-D50 CCD camera with the Infinity KC IF-2 zoom lens.

The final variable of interest is the ignition delay time. Whereas the previous two variables were independent variables, this one is the dependent. The goal of the experiment is to accurately predict the ignition delay times once the initial diameter and ambient temperature are known. In this experiment, ignition is characterized by measurement of UV emission from hydroxyl radical (OH*) chemiluminescence. This phenomena is invisible to the naked eye, and therefore requires the use of a suitable camera. The OH* chemiluminscence is captured by a Xybion ISG-250 intensified-array CCD video camera fitted with a Hamamatsu A4869 UV transmissive lens and an Andover 310FS10-50 narrow band interference filter centered at 310 nm. The video data from the Xybion and Hitachi cameras are merged into a split screen using a Colorado Video Systems video splitter and recorded onto a Sony S-VHS recorder. The S-VHS

data is later digitized and analyzed on a PC. The Xybion camera is shown in Figure 3.5. The setup of the entire camera system is discussed below.

Figure 3.5: Xybion ISG-250 intensified array CCD camera. Shown with the Hamamatsu A4869 UV transmissive lens. (Not shown: Andover 310FS10-50 narrow band interference filter.)

3.1.4 – Camera System

The Hitachi and Xybion cameras are only part of a larger camera system designed to allow accurate data acquisition as well as providing the ability to observe the tests in real time. The two cameras are the only video capturing devices, but there is a series of other devices that further enhance the cameras.

An important aspect of the camera system deals with the Xybion Controller, which is a separate control box from the Xybion camera itself. The main purpose of the controller is to simply work the Xybion camera, but there is also an option that allows for

another camera to be synced up with it. In this instance, the Hitachi CCD camera is synced with the Xybion camera, meaning that the internal clock of the Xybion camera overrides the internal clock of the Hitachi camera. This ensures that when analyzing the two video outputs, the elapsed time will be identical, allowing for faster and more accurate analysis of the ignition event.

However, the sync function does not affect the video outputs of either camera. Each camera still has its separate Video Out cable, but there is only one video monitor set up in the camera system. The monitor does have two separate BNC connector inputs and it's a simple matter of toggling the current input device to switch between the Hitachi view and the Xybion view. However, this method has two flaws due to the current setup. In order to record the two video outputs, it would be necessary to have two S-VHS recorders. Currently, there is only one S-VHS recorder available. Also, with the inclusion of a time code generator (Horita VG-50, Figure 3.6), the system would need two of them as well. Instead, by incorporating a video splitter into the system, the two camera outputs can be merged into one output, allowing for the use of only one time code generator and S-VHS recorder. Figure 3.7 shows a schematic of the camera system setup, while Figure 3.8 shows the actual 1-g setup.

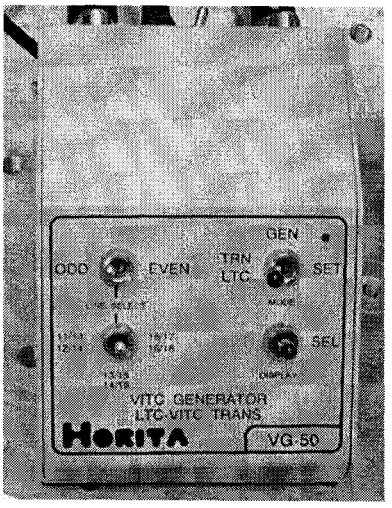

Figure 3.6: Horita VG-50 Time Code Generator.

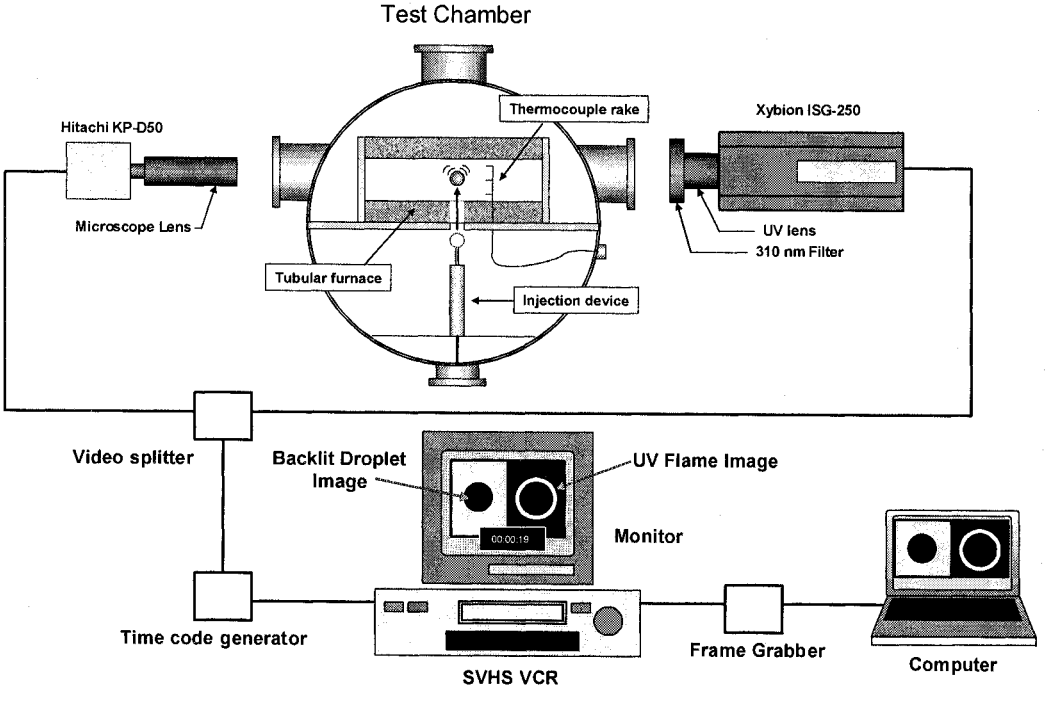

Figure 3.7: Schematic of the experimental setup.

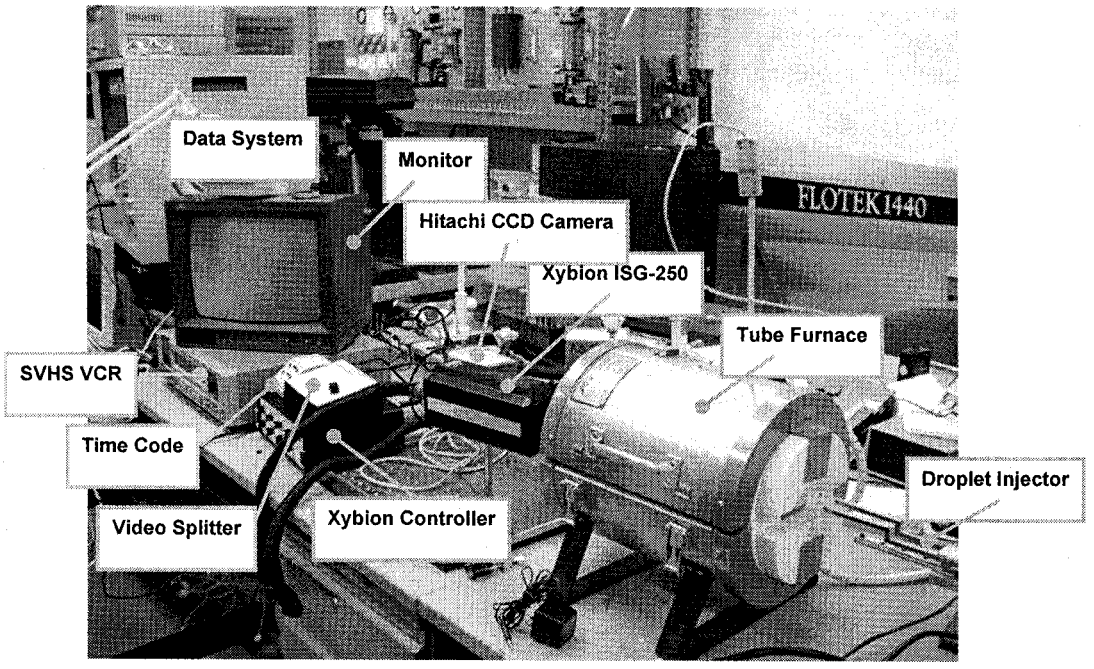

Figure 3.8: Actual 1-g experimental setup.

Section 3.2 – Initial Experimental Results

The two fuels studied experimentally were methanol and methyl butyrate. The overall goal of the biodiesel research program at Rowan is to determine the underlying characteristics that control how a bio-fuel reacts and burns. Therefore, the methyl butyrate was chosen for one set of experiments since a detailed chemical kinetic mechanism (264 species, 1219 reversible reactions) has been developed by Fisher and coworkers [9]. Currently, methyl butyrate has not been incorporated into the droplet combustion numerical model described in Chapter 4. Therefore, a second set of droplet ignition experiments were conducted with methanol, a fuel that has been extensively studied both numerically and experimentally by Marchese [11]. Specifically, since a time-dependent, chemically reacting flow model of methanol combustion already exists

(see Chapter 4), it is possible to predict when the methanol droplets will ignite, and experimental data and modeling results can be compared with each other. It should also be noted that, although Marchese and coworkers studied methanol droplet combustion in detail [11,52,61,62,63], methanol droplet *ignition* experiments and modeling were not conducted prior to the work presented in this thesis. The following subsections deal with several test runs done at various times.

3.2.1 – Initial Methanol Tests

The first set of experiments involved methanol droplets supported by a 10-15 micron fiber. A total of 30 tests were conducted, all of which were recorded onto video so that ignition delay could be measured. In an effort to alleviate any confusion that may result in arbitrarily playing the tape, each run used a different time code stamp. For example, if all tests started from zero every time, then it would be difficult to discern which run was which. Instead, the time code generator was used not only as an elapsed time reading, but also to identify the current test run. To better understand this, it is necessary to know that the time code generator displays time as such: 00:00:00:00. The last two digits indicate the frame (as in 30 frames per second), and the second to last digits are seconds. The identification system occurs within the first four digits, where the first two digits indicate the test day (00 for first test date, 01 for second, etc.), and the second two digits indicate the test number (00 for the first, 01 for the second, and so on). This way, when playing back the video, the time code shown at the bottom of the screen will point to a specific test that has been already documented. For example, a reading of 01:15:00:00 indicates that this test was run on the second day and is the 16^{th} test of the

day. Table 3.1 contains a summary of each test conducted on methanol and includes the furnace temperature and whether or not the droplet ignited.

Table 3.1: Initial methanol tests.

Batch Marker	Test Marker	Temperature [°C]	Ignition [Y/N]
00	00	Calibration runs	
00	01	799	N
00	02	802	N
00	03	806	N
00	04	849	Y
00	05	850	N
00	06	854	N
00	07	856	N
00	08	849	N
00	09	853	N
00	10	854	N
00	11	854	N
00	12	852	N
00	13	884	Y
00	14	860	N
00	15	863	N
00	16	867	N
00	17	868	N
00	18	867	N
00	19	868	Y
00	20	874	N
00	21	872	N
00	22	882	N
00	23	876	Y
00	24	882	Y
00	25	873	N
00	26	912	Y
00	27	914	Y
00	28	914	Y
00	29	906	Y
00	30	914	Y

As indicated in Table 3.1, a total of thirty test runs were initially conducted on methanol droplets. Out of the 30 droplets tested, 10 ignited. In the other 20 cases, the methanol droplets evaporated, or ignited before they were in focus of the video cameras.

In some instances, ignition of the epoxy bead can be seen, including one test in which both the methanol and epoxy ignited separately.

For the experiments in which ignition was observed, the initial diameter and ignition delay were determined by analyzing the video data. To analyze the data, video data from the S-VHS tapes were digitized using a Dazzle Digital Video Creator 150 and its accompanying software, Pinnacle Studio 9. The video data were converted to .mpeg format and then each .mpeg file was imported into another software program called Virtual Dub, which is able to separate each video frame into a separate image. Each image sequence was then opened in the NASA Spotlight software. Using Spotlight and a reference scale (to convert from pixels to mm), the initial size of the droplet and its ignition delay could be determined.

Since these tests were run in normal gravity and supported on a fiber, the droplets themselves were not perfectly symmetrical. Therefore, an equivalent diameter was needed. The following equation, used by Marchese [11], was used to define an equivalent diameter for each droplet:

$$D_{eq} = \sqrt[3]{D_t^2 D_l} \tag{3.1}$$

where D_{eq} is the equivalent diameter, D_t thelength of the droplet perpendicular to the fiber, and D_l the length of the droplet parallel to the fiber.

There is also an issue of the accuracy of the thermocouple inside the furnace. This thermocouple is responsible for regulating the temperature inside the furnace (it is hooked up to the temperature controller). However, the position of the thermocouple inside the furnace does not directly coincide with the location within the furnace where the droplet is inserted. Therefore, another test was run with the thermocouple placed onto

the droplet insertion mechanism. This ensures that the thermocouple is reading the temperature at the same location where the droplet is inserted. Calculations based on the previous temperatures and the new temperature suggests a 4% error on the previous temperatures. To correct this, all previous temperatures were multiplied by a factor of 0.96, and these new temperatures were used for the following data. The following table shows the ten runs, their initial equivalent diameters, and their ignition delays.

Table 3.2: Equivalent initial diameter and ignition delay of the initial methanol tests (with corrected temperature).

Test Run	Droplet size [mm]	Temperature [°C]	Ignition Delay [s]
00:04	1.4656	815.04	0.0333
00:13	1.3706	848.64	0.0333
00:19	1.1599	833.28	0.6667
00:23	1.0858	840.96	0.1667
00:24	0.8542	846.72	0.1667
00:26	1.2852	875.52	0.3667
00:27	1.2124	877.44	0.1667
00:28	1.2760	877.44	0.4000
00:29	0.9366	869.76	0.0667
00:30	Inconclusive		

As can be seen in the above table, Test 00:30 is inconclusive. This is due to the fact that the droplet actually ignited too quickly, and therefore was never in view of the Hitachi CCD camera (used for measuring the initial droplet diameter) although the ignition event was observed on the Xybion camera (used for measuring ignition). Also note that for the results presented in this thesis, it was only possible for the ignition delay time to be measured to within 1/30 of a second since standard S-VHS video was used. A move to a high-speed video camera could result in far more accurate ignition delay times although it is unclear whether the ignition event would be bright enough to observe using high speed video.

The following images, taken from the NASA Spotlight software, show the pre-ignition measurement (Figure 3.9) from the Hitachi camera and the ignition event (Figure 3.10) from the Xybion camera of the 00:19 test run. The left side of each image is the Hitachi view, while the right side is the Xybion view. The back-lit droplet images show that the droplets exhibit a reasonable degree of spherical symmetry. Moreover, the Xybion OH* emission signal also shows a reasonable degree of spherical symmetry. These results suggest that, for 1 mm droplets, the numerical model described in Chapter 4 could be used to simulate the 1-g ignition delay experiments to a reasonable of accuracy. As noted in the Chapter 5 of the thesis, however, there are still some major discrepancies between the numerical model and the 1-g, suspended droplet ignition experiments described herein, which make comparisons with the numerical model difficult.

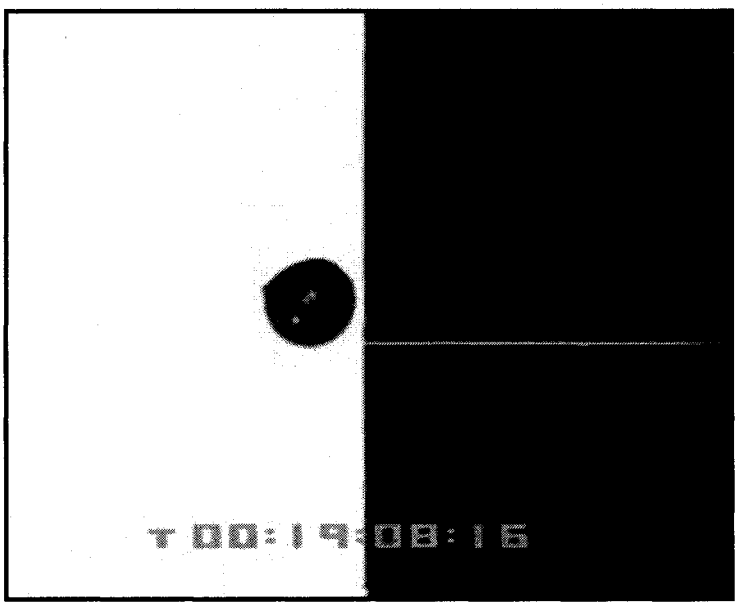

Figure 3.9: Backlit droplet image prior to ignition (methanol, 1.16 mm, 833 °C).

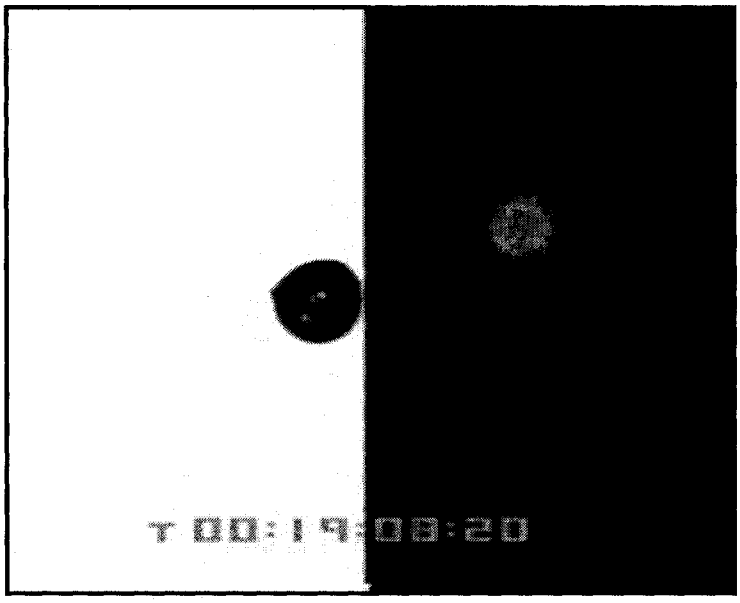

Figure 3.10: OH* emission at the ignition event (methanol, 1.16 mm, 833 °C).

The most important thing that can be determined from the first set of experiments are qualitative trends. Figure 3.11 shows the ignition delay plotted against the adjusted furnace temperature. Nominal diameter ranges were chosen to illustrate any trends. As can be seen, the ignition delay tends to decrease as the temperature increases, which is expected. However, it appears that the larger drops (1.4 mm nominal range) have a much lower ignition delay time, which is opposite of what is expected. In Figure 3.12, which plots the ignition delay versus initial equivalent diameter with nominal diameter ranges, there seems to be little correlation. As the diameter increases while holding the temperature roughly constant, the ignition delay time is sporadic. Data points are scattered throughout the plot, with no real correlation between any of them.

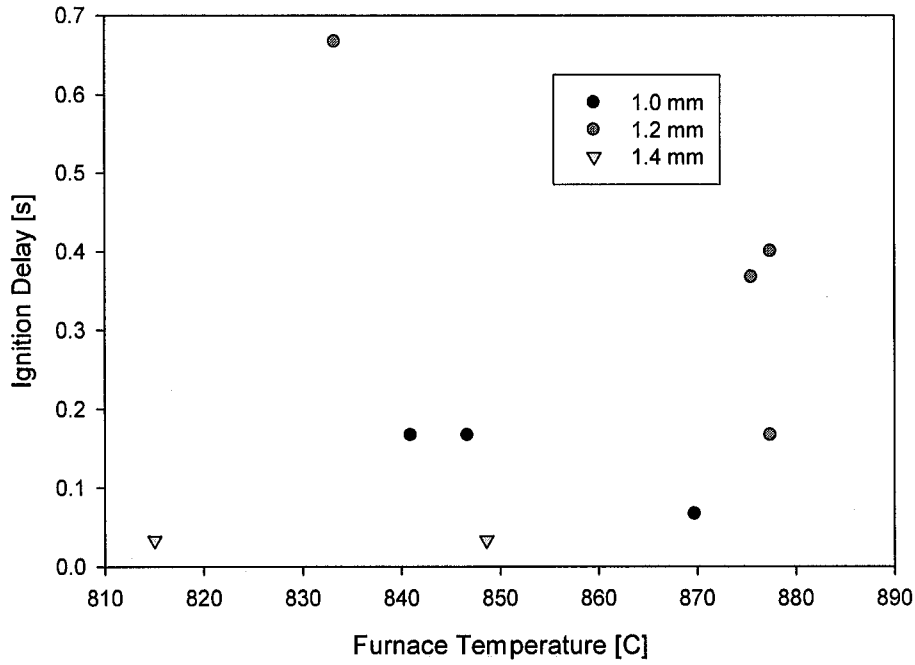

Figure 3.11: Ignition delay vs. furnace temperature of initial tests of methanol fuel droplets, with nominal diameter ranges.

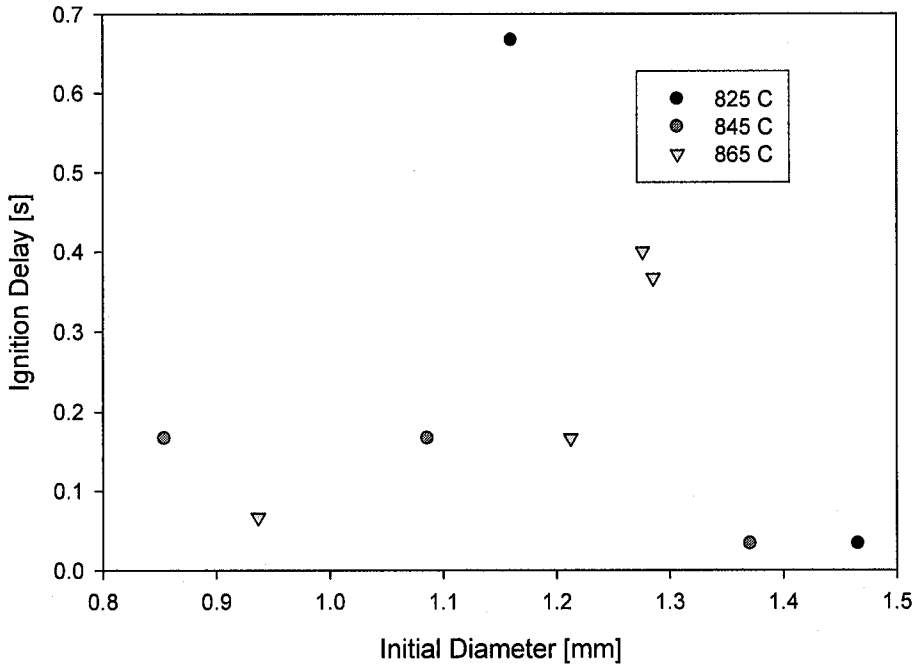

Figure 3.12: Ignition delay vs. droplet diameter of initial tests of methanol fuel droplets, with nominal temperature ranges.

3.2.2 – Initial Methyl Butyrate Tests

The initial methyl butyrate tests were conducted identically to the initial methanol tests. The time code generator was again used to distinguish individual tests, and the same method for digitizing and analyzing the data was used. Table 3.3 shows the initial results from the methyl butyrate runs.

Table 3.3: Initial methyl butyrate tests.

Batch Marker	Test Marker	Temperature [°C]	Ignition [Y/N]
00	31	924	Y
00	32	810	N
00	33	841	N
00	34	854	N
00	35	852	N
00	36	857	N
00	37	865	N
00	38	868	N
01	00	856	N
01	01	888	N
01	02	909	N
01	03	915	N
01	04	915	N
01	05	912	Y
01	06	913	Y
01	07	915	N
01	08	920	N
01	09	923	Y (TC ERROR)
01	10	926	Y
01	11	936	N
01	12	944	Y
01	13	937	Y
01	14	949	Y
01	15	947	Y
01	16	950	N
01	17	955	Y
01	18	943	N
01	19	947	N
01	20	910	N
01	21	960	Y

For the methyl butyrate tests, thirty tests were conducted and approximately ten showed ignition. The entry in the table marked with the TC ERROR ignited, but the time code generator was not started on time, and therefore any data relating to the ignition delay would not be accurate. The video data of the successful experiments were digitized and analyzed. As detailed above, the equivalent diameter was found using Equation (3.1), and the temperature was corrected for the 4% error. The reduced ignition delay is summarized in Table 3.4.

Table 3.4: Equivalent initial diameter and ignition delay of the initial methyl butyrate test (with corrected temperature).

Test Run	Droplet Size [mm]	Temperature [°C]	Ignition Delay [s]
00:31	1.0634	887.04	0.2667
01:05	0.8542	875.52	0.2667
01:06	Inconclusive		
01:10	0.9068	888.96	0.2333
01:12	1.0951	906.24	0.2000
01:13	1.3689	899.52	0.4333
01:14	1.6856	911.04	1.4333
01:15	1.3689	909.12	0.3000
01:17	1.7546	916.80	0.3667
01:21	1.2218	921.60	0.3000

As was also observed in the methanol experiments, there was one test in which it was impossible to determine the ignition delay time due to the fact that it ignited too soon. Test 01:06 was therefore inconclusive. Test 01:14 appeared to be an outlier, igniting a full second after any of the other droplets had ignited. As a result, the 01:14 test provides distinct pictures of pre-igntion (Figure 13) and the ignition event (Figure 14). Again, the Hitachi camera is displayed on the left side of the image, while the Xybion view is on the right. The backlit droplet image once again shows a high degree

of spherical symmetry. The OH* chemiluminescence image is somewhat symmetrical, although it appears to have higher intensity in the lower half of the flame.

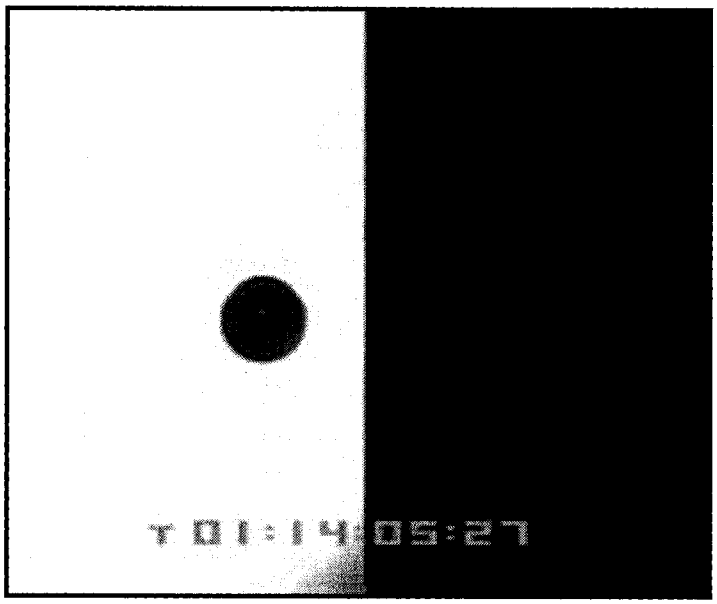

Figure 3.13: Backlit droplet image prior to ignition (methyl butyrate, 1.69 mm, 911 °C).

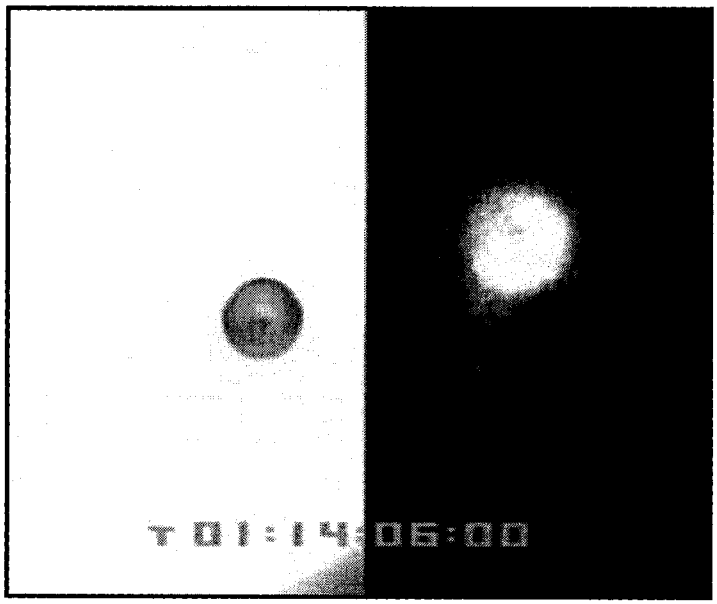

Figure 3.14: OH* emission at ignition (methyl butyrate, 1.69 mm, 911 °C).

Figure 3.15 shows the ignition delay plotted against the adjusted furnace temperature. Looking at the data spread (again using a nominal diameter range), it appears that there is a correlation between the ignition delay and the furnace temperature, as was seen with the methanol tests. Figure 3.16 plots the ignition delay versus the initial diameter with nominal temperature ranges. The data shows a better correlation between initial diameter and ignition delay than in the methanol case, but as can be seen, the correlation is not as strong as the correlation between ignition delay and initial temperature.

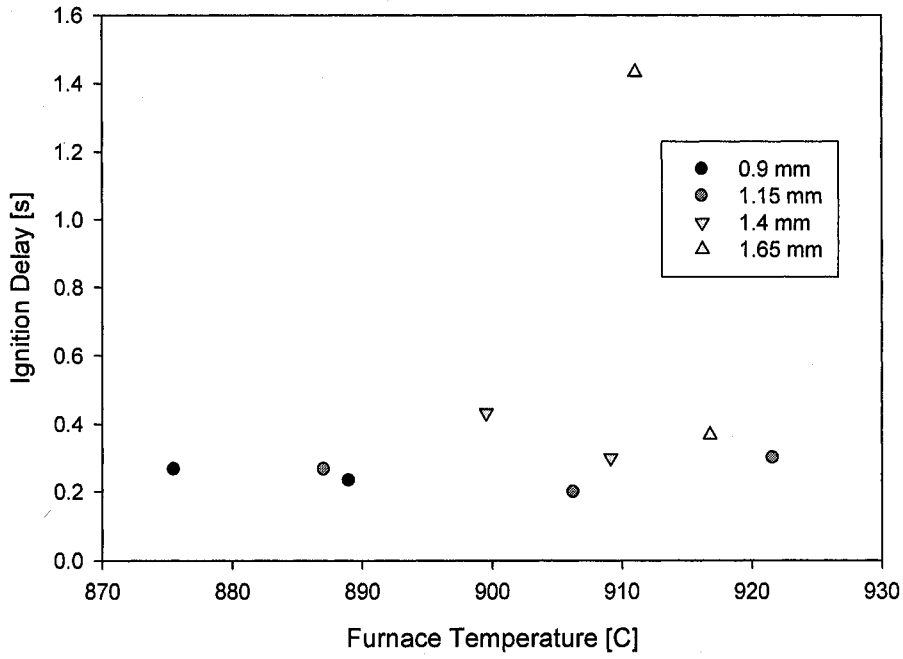

Figure 3.15: Ignition delay vs. furnace temperature of initial tests of methyl butyrate droplets.

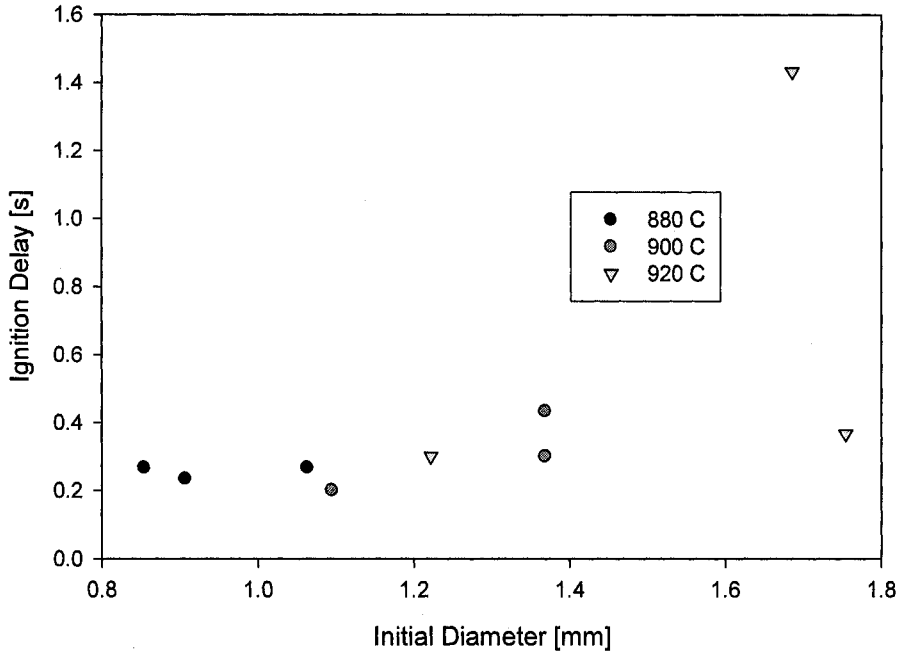

Figure 3.16: Ignition delay vs. droplet diameter of initial tests of methyl butyrate fuel droplets.

Section 3.3 – Experiments with Modified Suspension Method

The experiments above were conducted by placing a bead of epoxy onto a silicon carbide fiber (roughly 15 microns thick) and stretching that fiber across the injection forks. This method proved to be difficult to implement repeatedly. Fibers that small are easily broken and the epoxy bead sizes that could be accommodated on the thin fibers limited the droplet sizes that could be used. As can be seen above, the droplet sizes ranged only from a little smaller than 1 mm to about 1.75 mm. Another difficulty with the fiber/epoxy method was that the epoxy bead would ignite after each droplet ignited, resulting in the necessity to change the fiber after each test. To increase the range of droplet diameters that could be tested and to alleviate the difficulty associated with igniting the epoxy bead, a second suspension technique was employed.

The new suspension method involved quartz rods from Quartz Scientific Incorporated. Beginning with quartz rods of 1 mm in diameter, a MAPP (methylacetylene-propadiene) torch was used to neck the rod in the middle. A break was then forced in this necking area, providing two separate quartz rods that were still 1 mm at the top, but became as small as 75 microns at the bottom. Then, using "The Little Torch" (by Smith Equipment), a bead was made at the bottom of the rod. Two separate torches were used in the overall process because of the temperature of their respective flames. The MAPP torch provided the conditions necessary for necking the rod, but the flame was not hot enough to fashion a bead on the end of the rod. Conversely, the acetylene-oxygen flame produced by "The Little Torch" provided the temperature necessary to form a bead, but proved to be difficult to use for the necking process.

For the second set of experiments, the Hitachi camera was also moved from its original position beside the Xybion camera, to the other side of the furnace. It was placed perpendicular to the orientation of the furnace, and is focused on a point just prior to where the droplet is inserted into the furnace. This allowed for a clearer, more accurate determination of the initial diameter of each droplet. The field of view was placed as close to the furnace as possible to provide a better approximation of the ignition delay time. The exact moment (down to the 1/30 of a second due to the limitations of the Hitachi) that the droplet left the field of view of the camera is considered the start time to the ignition delay. The difference in the time code generator from that point to ignition was defined as the ignition delay. Figures 3.17 and 3.18 show images from the experiments conducted using the quartz suspension fiber. One negative aspect of the

quartz suspension fiber is that the droplets show more of a deviation from spherical symmetry than those suspended on the silicon carbide/epoxy fibers.

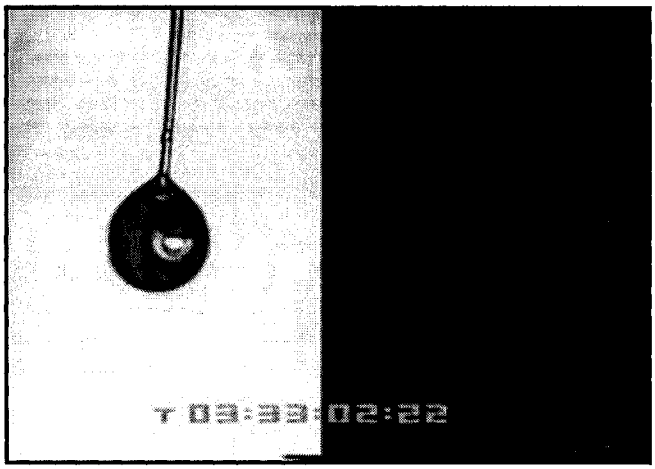

Figure 3.17: Backlit droplet image prior to insertion (methanol, 1.6358 mm, 930 °C).

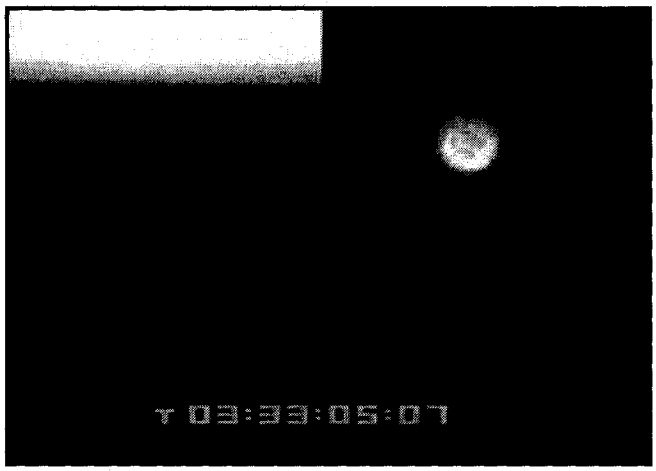

Figure 3.18: OH* emission at ignition (methanol, 1.6358 mm, 930 °C).

Many individual suspension rods were made. The necking ranged in sizes from 75 microns up to 250 microns, whereas the beads ranged from 150 microns to 550 microns. Using these new suspension rods, additional ignition delay experiments on methanol and methyl butyrate were conducted.

3.3.1 – Methanol Tests with Quartz Rods

The results of the methanol tests with the quartz suspension rods and new camera set up are summarized in Table 3.5.

Table 3.5: Methanol tests with a quartz rod bead size of 250 microns.

Batch Marker	Test Marker	Temperature [°C]	Ignition [Y/N]
02	00	917	N
02	01	915	Y
02	02	924	Y
02	03	923	N
02	04	923	Y
02	05	911	Y
02	06	911	Y
02	07	917	Y
02	08	897	Y
02	09	911	Y
02	10	894	N
02	11	904	Y
02	12	904	Y
02	13	896	Y
02	14	890	N
02	15	884	N
02	16	886	Y
02	17	892	Y
02	18	883	N
02	19	883	N
02	20	889	N
02	21	885	N
02	22	890	N
02	23	895	Y
02	24	885	N
02	25	894	Y
02	26	892	Y
02	27	895	Y
02	28	903	Y
02	29	897	N
02	30	902	Y
02	31	905	Y
02	32	911	N
02	33	907	N
02	34	903	Y

02	35	904	Y
02	36	921	Y
02	37	921	Y
02	38	920	Y
02	39	914	Y
02	40	926	N
02	41	929	Y
02	42	934	Y
02	43	934	Y
02	44	940	Y
02	45	945	Y
02	46	943	Y
02	47	946	Y
02	48	941	Y
02	49	952	Y
02	50	956	Y

The above tests were run with a constant bead size of 250 microns. As can be seen, the temperature was slowly ramped up to provide a wider range of ignition delay times. The successful runs, and their corresponding ignition delay times, are summarized in Table 3.6.

Table 3.6: Equivalent initial diameter and ignition delay times of methanol in the updated setup (Bead Size = 250 microns)

Test Run	Droplet Size [mm]	Temperature [°C]	Ignition Delay [s]
02:01	1.1999	915	0.9333
02:02	1.3362	924	0.7000
02:04	1.3089	923	0.6667
02:05	1.3578	911	1.3333
02:06	1.2230	911	0.5667
02:07	1.2063	917	0.4667
02:08	1.1573	897	0.5000
02:09	1.2271	911	0.4000
02:11	1.2987	904	0.9333
02:12	1.3017	904	0.7333
02:13	1.2373	896	1.2000
02:16	1.2271	886	0.5667
02:17	1.2168	892	0.6000
02:23	1.1516	895	1.5667
02:25	1.3734	894	1.2667

02:26	1.2917	892	0.5333
02:27	1.2337	895	0.6333
02:28	1.1622	903	0.9333
02:30	1.2917	902	0.8000
02:31	0.9324	905	0.8333
02:34	1.2645	903	1.4667
02:35	1.3089	904	1.0667
02:36	1.2714	921	0.8667
02:37	1.2917	921	1.0000
02:38	1.2337	920	0.4667
02:39	1.3260	914	1.2667
02:41	1.3289	929	1.3000
02:42	1.3089	934	0.5000
02:43	1.1895	934	0.5333
02:44	1.2063	940	0.4667
02:45	1.2917	945	0.8333
02:46	1.1726	943	0.8333
02:47	1.3089	946	0.5000
02:48	1.2714	941	0.5000
02:49	1.2917	952	0.6000
02:50	1.2504	956	0.5333

Again, it can be seen that image analysis system currently employed allows for accuracy down to 1/30 of a second, which results in identical ignition delay times for droplet sized close to each other. With a more advanced system, it would be possible to find distinct ignition delay times for each pair of droplet diameter and ambient temperature.

To generate larger droplets, another series of experiments were conducted on the methanol droplets. In this set, a different quartz rod with a different bead size was used in order to generate the larger droplet sizes. For these experiments, a bead size of 430 microns was used. Tables 3.7 and 3.8 contain summaries of the raw data and the analysis of the successful runs, respectively.

Table 3.7: Methanol tests with a quartz rod bead size of 430 microns.

Batch Marker	Test Marker	Temperature [°C]	Ignition [Y/N]
03	00	882	N
03	01	870	N
03	02	871	N
03	03	880	N
03	04	880	N
03	05	887	N
03	06	885	N
03	07	873	N
03	08	894	N
03	09	894	N
03	10	893	N
03	11	901	N
03	12	904	Y
03	13	904	N
03	14	904	N
03	15	905	N
03	16	897	N
03	17	910	N
03	18	904	N
03	19	905	Y
03	20	904	N
03	21	902	N
03	22	913	N
03	23	910	N
03	24	915	Y
03	25	920	Y
03	26	910	N
03	27	924	Y
03	28	924	Y
03	29	925	Y
03	30	920	Y
03	31	923	Y
03	32	927	N
03	33	930	Y
03	34	934	Y
03	35	926	Y
03	36	930	Y
03	37	932	Y
03	38	930	Y
03	39	936	Y
03	40	947	Y

03	41	945	Y
03	42	940	Y
03	43	946	Y
03	44	961	Y
03	45	960	Y
03	46	959	Y
03	47	984	Y
03	48	972	Y
03	49	983	Y
03	50	972	Y

Table 3.8: Equivalent initial diameter and ignition delay times of methanol in the updated setup (Bead Size = 430 microns)

Test Run	Droplet Size [mm]	Temperature [°C]	Ignition Delay [s]
03:12	1.5194	904	1.1667
03:19	1.4650	905	0.7000
03:24	1.3190	915	1.2667
03:25	1.3190	920	1.2333
03:27	1.5738	924	1.2667
03:28	1.3833	924	0.8667
03:29	1.3561	925	1.9667
03:30	1.3833	920	1.0667
03:31	1.4922	923	1.5667
03:33	1.6358	930	0.8333
03:34	1.5018	934	1.1667
03:35	Inconclusive		
03:36	Inconclusive		
03:37	1.4007	932	1.8000
03:38	1.5194	930	0.8333
03:39	1.3931	936	0.6667
03:40	1.3115	947	0.7000
03:41	1.4203	945	1.0000
03:42	1.5194	940	0.6000
03:43	1.3483	946	0.5000
03:44	1.4650	961	0.9333
03:45	1.5194	960	0.6000
03:46	1.2745	959	0.4333
03:47	1.3931	984	0.8000
03:48	1.4203	972	0.4333
03:49	1.4475	983	0.4333
03:50	Inconclusive		

Although the above sets of tables deal with slightly different cases, it is still desirable to include all the successful runs on one plot in order to identify any trends that may have resulted from the experimentation. Taking out the three tests above that were deemed inconclusive due to either lack of data or problems with the individual recordings, the methanol tests can be plotted against initial temperature and initial diameter. It is advantageous to be able to see the two variables (temperature and diameter) on the same plot. By grouping similar diameters into one nominal diameter, the two different variables can be seen on the same plot. In this case, the methanol droplets were broken down into diameter ranges of 0.1 mm. For instance, a diameter falling in the range of 1.25 mm and 1.34 mm was classified as 1.3 mm. Figure 3.19 shows the ignition delay of the methanol droplets versus ambient temperature, with diameter ranges indicated. Figure 3.20 shows the same data as Figure 3.19, but includes hand drawn trend lines through each set of points to indicate correlation between ignition delay and ambient temperature.

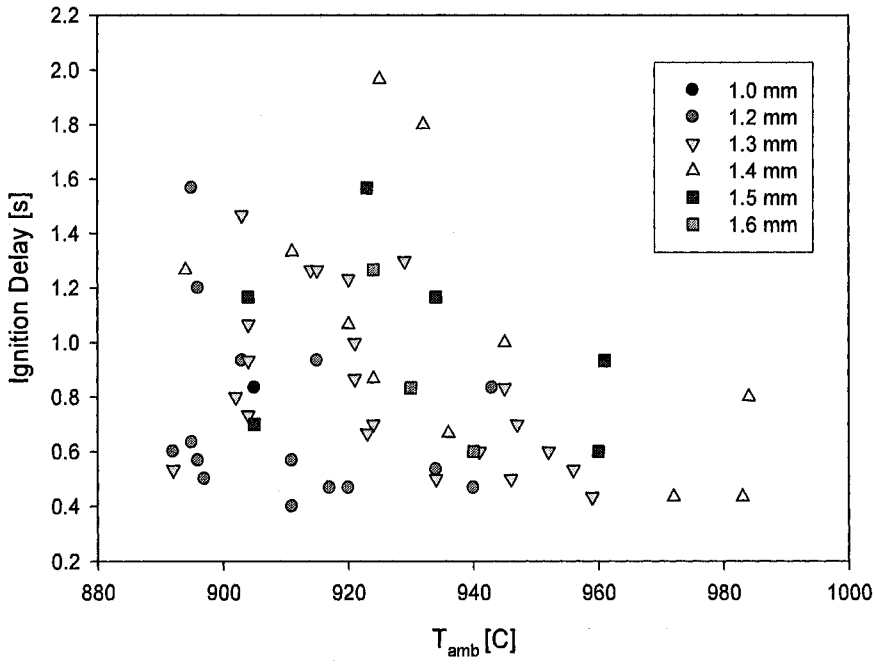

Figure 3.19: Ignition delay vs. ambient temperature of methanol droplets, broken down into specific diameter ranges.

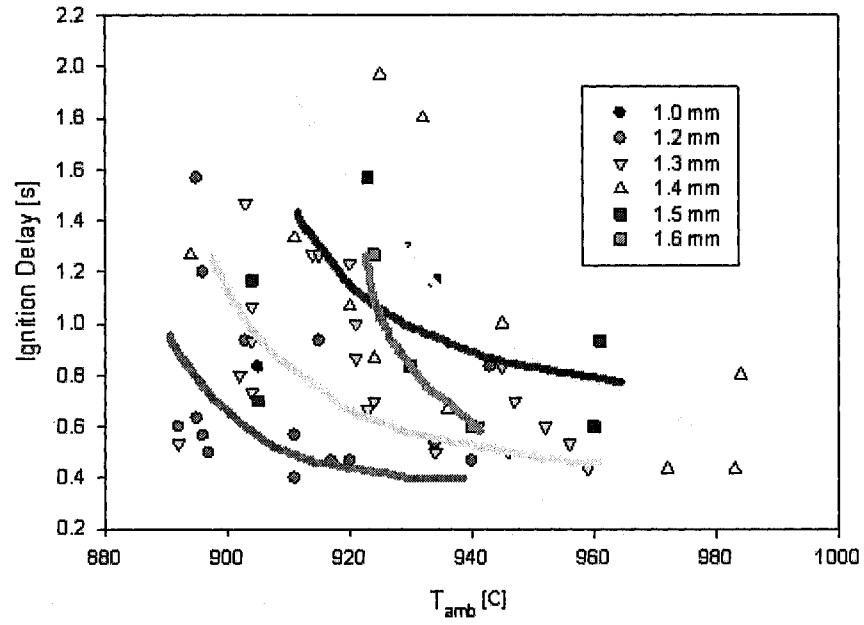

Figure 3.20: Ignition delay vs. ambient temperature, broken down into nominal diameter ranges. Shown with hand drawn trend lines.

Although Figures 3.19 and 3.20 clearly contain significant scatter, the trends of ignition delay versus initial temperature are similar to those predicted by the numerical modeling (See Chapter 4). Specifically, the data show that ignition delay of the droplets increases with decreasing furnace temperature and increases with increasing droplet size. Sources of uncertainty in the above data are discussed in Chapter 5.

3.3.2 – Methyl Butyrate Tests with Quartz Rods

Similar tests were run with the methyl butyrate fuel using the quartz rod suspension technique. Table 3.9 contains a summary of experiments conducted with a quartz bead size of 430, whereas Table 3.10 summarizes experiments run with a quartz bead size of 350 microns. Note that all tests conducted with the bead size of 430 microns resulted in no ignition for the methyl butyrate droplets (tests 04:00-04:17). After test 04:17, the quartz rod was broken and needed to be replaced with the quartz rod with bead size 350 microns.

Table 3.9: Methyl butyrate tests with a bead size of 430 microns.

Batch Marker	Test Marker	Temperature [°C]	Ignition [Y/N]
04	00	905	N
04	01	904	N
04	02	915	N
04	03	921	N
04	04	920	N
04	05	924	N
04	06	928	N
04	07	933	N
04	08	928	N
04	09	935	N
04	10	943	N
04	11	943	N
04	12	934	N

04	13	955	N
04	14	953	N
04	15	940	N
04	16	951	N
04	17	955	N

Table 3.10: Methyl butyrate tests with a bead size of 350 microns.

Batch Marker	Test Marker	Temperature [°C]	Ignition [Y/N]
04	18	936	N
04	19	951	N
04	20	965	N
04	21	961	N
04	22	960	N
04	23	960	N
04	24	963	Y
04	25	968	N
04	26	965	Y
04	27	971	Y
04	28	962	N
04	29	968	Y
04	30	967	Y
04	31	969	N
04	32	974	N
04	33	971	Y
04	34	970	Y
04	35	976	Y
04	36	976	N
04	37	968	N
04	38	973	N
04	39	963	N
04	40	967	N
04	41	972	Y
04	42	973	N
04	43	969	Y
04	44	974	Y
04	45	970	Y
04	46	970	Y
04	47	973	N
04	48	964	Y
04	49	968	N
04	50	973	Y

The first thing to note about the methyl butyrate experiments is the need to run them at higher temperatures than the methanol tests. As a result, the safety limit of the furnace apparatus was approached and surpassed. The safety rating on the ATS furnace is 950 °C and, as can be seen above, the experiments exceeded this by as much as thirty degrees Celsius. This overheating was also done in the methanol experiments, but was out of curiosity rather than necessity. As a result, the furnace appeared to have trouble maintaining temperatures over 950 °C. It is not known why this particular temperature was specified as the safety rating, whether it be the electrical circuitry that couldn't handle more power, or if the alumina insulation had limitations, or some other limitation.

Also of note is the fact that all tests run with a quartz fiber bead size of 430 microns failed to ignite. This could be due to the transient heating of the quartz fiber as it is subjected to large temperature gradients. Not allowing for significant cool down time between tests may result in a higher temperature of the quartz fiber, which would in turn heat the liquid droplet from the inside. Consequently, the droplet may be evaporating long before it is subjected to the hot ambient environment of the furnace. Table 3.11 tabulates the test runs that successfully ignited.

Table 3.11: Equivalent initial diameter and ignition delay times of methyl butyrate in the updated setup (Bead Size = 350 microns)

Test Run	Droplet Size [mm]	Temperature [°C]	Ignition Delay [s]
04:24	1.4179	963	1.9000
04:26	1.4570	965	1.7000
04:27	1.2168	971	1.5667
04:29	1.4377	968	1.2000
04:30	1.3931	967	0.6333
04:33	1.4203	971	1.6000
04:34	1.2472	970	0.7667
04:35	1.3755	976	1.8333
04:41	1.4842	972	1.9000

04:43	1.4377	969	1.6333
04:44	1.4842	974	1.8333
04:45	1.4475	970	1.5667
04:46	1.4299	970	0.7000
04:48	1.4203	964	1.8000
04:50	1.4650	973	1.6333

Table 3.12 summarizes experiments that were conduced using a 235 micron bead size.

Table 3.12: Methyl butyrate tests with a bead size of 235 microns.

Batch Marker	Test Marker	Temperature [°C]	Ignition [Y/N]
05	00	915	N
05	01	911	N
05	02	927	N
05	03	931	N
05	04	930	N
05	05	938	N
05	06	943	N
05	07	940	N
05	08	943	N
05	09	946	Y
05	10	956	Y
05	11	954	Y
05	12	956	N
05	13	944	Y
05	14	946	N
05	15	940	N
05	16	946	N
05	17	933	N
05	18	956	N
05	19	952	N
05	20	953	Y
05	21	954	N
05	22	954	Y
05	23	953	Y
05	24	954	N
05	25	960	Y
05	26	966	N
05	27	961	Y

05	28	961	Y
05	29	954	Y
05	30	962	N
05	31	955	N
05	32	961	Y
05	33	960	Y
05	34	955	Y
05	35	960	Y
05	36	967	N
05	37	973	Y
05	38	968	Y
05	39	972	N
05	40	965	Y
05	41	976	Y
05	42	966	Y
05	43	976	N
05	44	974	Y
05	45	958	Y
05	46	956	N
05	47	964	N
05	48	960	N
05	49	953	N
05	50	956	N

Due to the smaller droplets that can be made with the 235 micron bead as opposed to the larger 350 micron bead, more tests were successful, and the furnace temperature did not need to be put as high as for the 350 micron bead experiments. Table 3.13 contains the reduced data from the 235 micron experiments.

Table 3.13: Equivalent initial diameter and ignition delay times of methyl butyrate in the updated setup (Bead Size = 235 microns)

Test Run	Droplet Size [mm]	Temperature [°C]	Ignition Delay [s]
05:09	1.1580	946	0.6667
05:10	1.0394	956	0.4333
05:11	1.1132	954	0.4667
05:13	1.1404	944	0.4667
05:20	1.1404	953	0.5333
05:22	1.1404	954	1.7000
05:23	1.0764	953	0.4667

05:25	0.9305	960	0.4000
05:27	1.1226	961	0.5333
05:28	1.0860	961	0.4000
05:29	1.0938	954	0.5333
05:31	1.1498	961	0.6333
05:33	1.1036	960	0.3000
05:34	1.0938	955	0.4000
05:35	1.1498	960	0.3000
05:37	1.1132	973	0.3000
05:38	1.1132	968	0.4000
05:40	1.0492	965	0.4000
05:41	1.1308	976	0.5000
05:42	Inconclusive		
05:44	1.1580	974	0.5333
05:45	1.1308	958	0.4000

As with the methanol data, it is advantageous to indicate both variables on the same set of plots. Therefore, the following graphs were generated by first dividing the data into specific diameter ranges and plotting the ignition delay versus the ambient temperature. Figure 3.21 shows the raw data divided into the nominal diameter ranges. Hand drawn trend lines are then added in Figure 3.22.

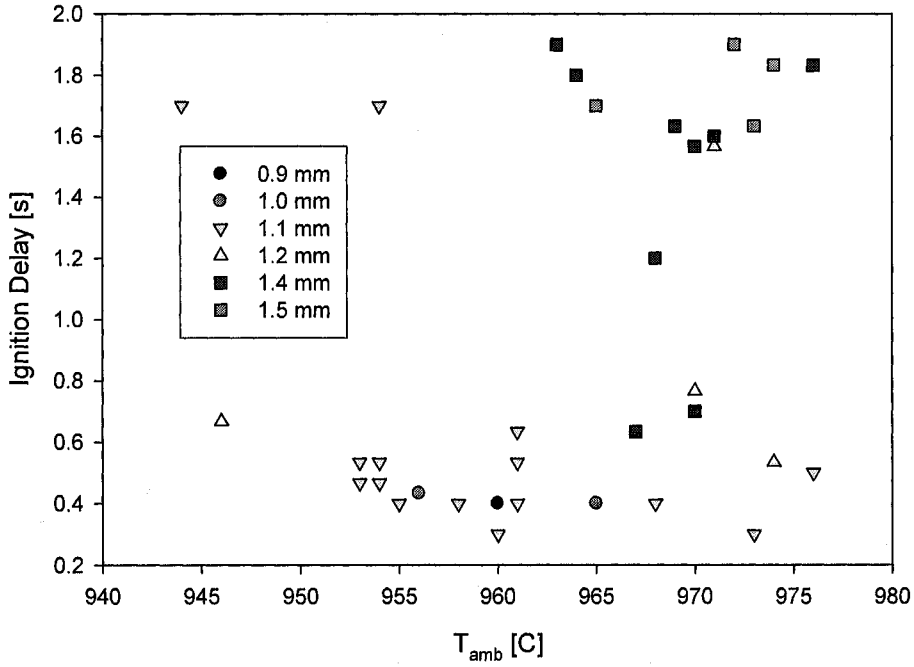

Figure 3.21: Ignition delay vs. ambient temperature of methyl butyrate droplets using the updated setup. The data has been broken into nominal diameter ranges.

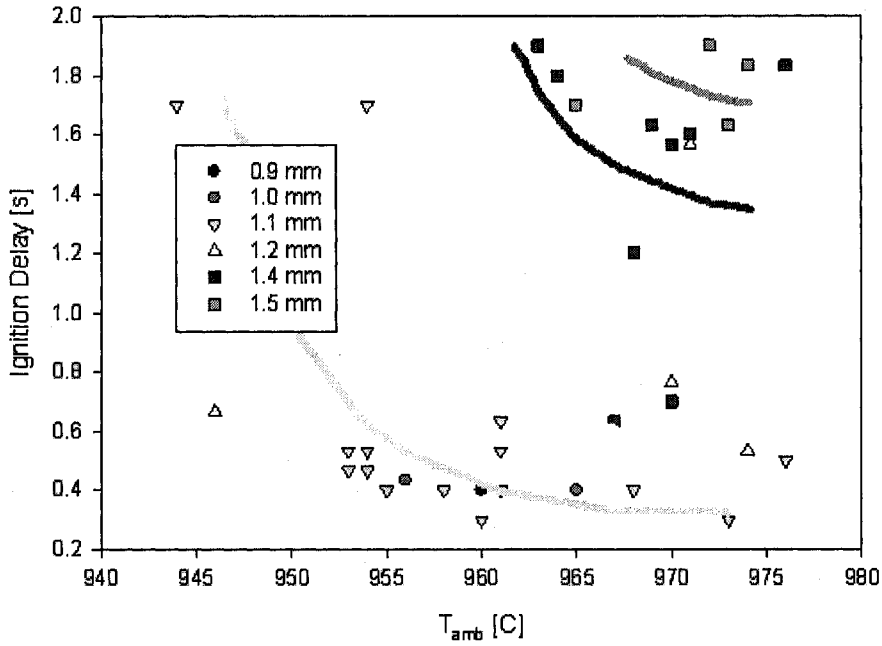

Figure 3.22: Ignition delay vs. ambient temperature of methyl butyrate droplets, shown with hand-drawn trend lines.

The methyl butyrate data correlates well with what was expected. As the temperature of the furnace is increased, the ignition delay times decrease. As will be seen in Chapter 4, the ignition delay time does not decrease as a linear function; instead, it follows a decaying exponential trend, as appears in Figure 3.22.

Further testing on both methanol and methyl butyrate fuel needs to be conducted, in both normal gravity and microgravity. Further discussions on the above experiments can be found in Chapter 5. The next chapter introduces the numerical model used to simulate methanol droplets in microgravity conditions.

Chapter Four

Numerical Modeling

Section 4.0 – Overview

While experimental data provides real-world answers, without an accompanying theoretical or numerical model, it is difficult to interpret the results and even more difficult to draw conclusions that can be extended to other systems. Development of a theoretical or numerical model is also useful for conducting simulated experiments over a much wider range of conditions than can sometimes be available to the experimentalist. In the case of running ignition delay tests in a microgravity setting, problems arise in the difficulty of conducting the experiments as well as availability of microgravity devices such as a drop tower, the KC-135 Weightless Wonder, and space-based missions. Having an accurate numerical model of the experiment allows tests to be run simply by changing the initial conditions of the system. For the droplet combustion modeling described here, the simulations take longer to run than actual experiments, but can be run overnight without the presence of a person.

The numerical model employed in this study simulates the ignition of a single, isolated methanol droplet. Specifically, a cool (e.g. room temperature) droplet is suddenly subjected to a hot, spherically symmetric, ambient environment. The effects of buoyancy are ignored. The numerical model used is a variation of a moving finite-element model originally developed by Cho, *et al* [53]. This time-dependent, chemically reacting flow model simulates the transient, spherically symmetric, isobaric combustion of a multi or single component liquid droplet. Buoyancy and forced convection effects

are assumed to be negligible, and the model is subdivided into three sections: gas phase, liquid phase, and a vapor/liquid interface. In the gas phase region, the model considers detailed molecular transport and complex chemical kinetic mechanisms. In the liquid phase region, liquid species mass transfer and the conservation of energy are solved. A similar model has been used previously to simulate methanol/water droplet combustion [54] and heptane ignition [52]. The numerical model also includes an OH* chemiluminescence sub-model [55] and a gas-phase thermal radiation sub-model [56].

As stated above, the numerical model takes three scenarios into consideration: the gas phase, the liquid phase, and the interaction between the two. For each of these cases, a set of governing equations are solved by the numerical model. An overview of the governing equations for the gas and liquid phase follows. For a more in depth discussion, refer to Marchese [11]. In the gas phase, the conservation of mass, energy, and species are the governing equations:

$$\frac{\partial}{\partial t}(\rho_g)+\frac{1}{r^2}\frac{\partial}{\partial r}(r^2\rho_g v_r)=0 \tag{4.1}$$

$$\rho_g\frac{\partial Y_{g,i}}{\partial t}+\rho_g v_r\frac{\partial Y_{g,i}}{\partial r}=-\frac{1}{r^2}\frac{\partial}{\partial r}(r^2\rho_g Y_{g,i}V_{r,i})+\omega_{g,i} \tag{4.2}$$

$$\begin{aligned}\rho_g C_{p,g}\frac{\partial T_g}{\partial t}+\rho_g C_{p,g}v_r\frac{\partial T_g}{\partial r}=\frac{1}{r^2}\frac{\partial}{\partial r}(r^2\lambda_g\frac{\partial T_g}{\partial r}-q_R)-\\ \rho_g\sum_{i=1}^{n}(Y_{g,i}V_{r,i}C_{p,g,i})\frac{\partial T_g}{\partial r}-\sum_{i=1}^{n}\omega_{g,i}H_{g,i}\end{aligned} \tag{4.3}$$

where ρ_g is the density of the gas mixture, $C_{p,g}$ the specific heat of the gas mixture at constant pressure, λ_g the thermal conductivity of the gas mixture, $Y_{g,i}$ the mass fraction of the i^{th} species in the gas phase, T_g the temperature of the gas mixture,

q_R the radiative heat flux, $C_{p,g,i}$ the specific heat at constant pressure of the i^{th} gas phase species, $H_{g,i}$ the enthalpy of the i^{th} gas phase species, $V_{r,i}$ the diffusion velocity of the i^{th} species, v_r the fluid velocity in the radial direction, r the radial coordinate, $\omega_{g,i}$ the mass production rate of the i^{th} species by gas-phase chemical reaction, and n the number of chemical species.

In the liquid phase, the governing equations are as follows:

$$\frac{\partial Y_{l,i}}{\partial t} = \frac{1}{r^2}\frac{\partial}{\partial r}\left(r^2 D_{l,i}\frac{\partial Y_{l,i}}{\partial r}\right) \tag{4.4}$$

$$\rho_l C_{p,l}\frac{\partial T_l}{\partial t} = \frac{1}{r^2}\frac{\partial}{\partial r}\left(r^2 \lambda_l \frac{\partial T_l}{\partial r}\right) \tag{4.5}$$

where $Y_{l,i}$ is the liquid mass fraction of the i^{th} liquid phase species, ρ_l the liquid density, $C_{p,l}$ the specific heat, λ_l the thermal conductivity, and T_l the liquid temperature. A detailed schematic of the above equations can be seen in Figure 4.1.

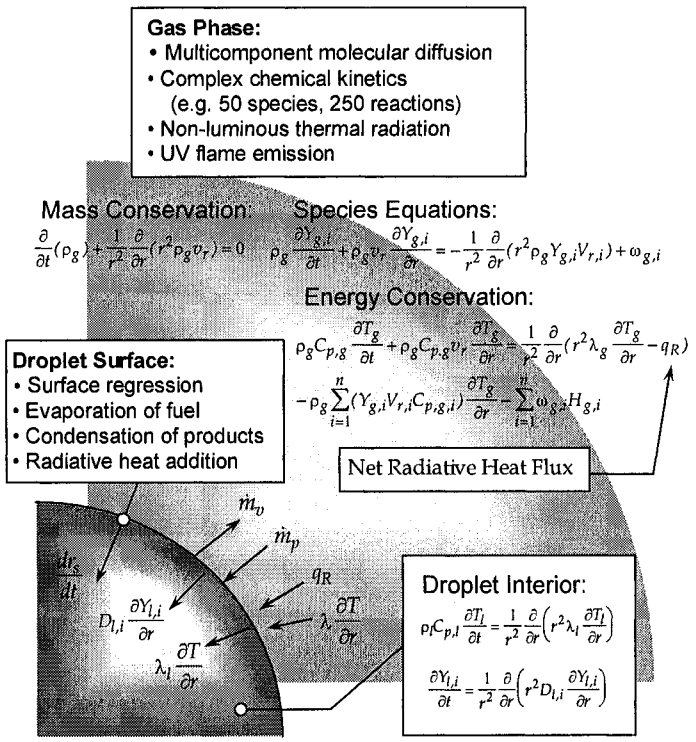

Figure 4.1: Detailed schematic of the numerical model.

For the droplet ignition modeling, the fuel droplet is suddenly subjected to high ambient temperature. In the following sections, various initial conditions are investigated. The initial conditions include the ambient temperature surrounding the droplet and the diameter of the droplet. The fuel used in all simulations was methanol (CH_3OH) and the simulations were all run under atmospheric pressure. As part of the present study, a radiative heat transfer model was developed to account for the radiation heat transfer from the furnace walls to the droplet surface. For the calculations with radiative heat transfer, the emissivity of the droplet, and the emissivity of the split-tube

furnace were varied parametrically to elucidate the impact of radiative heat transfer on ignition delay.

Section 4.1 – Modeling without Radiation

Initial numerical simulations were run without the inclusion of radiation effects. Most droplet combustion theories typically ignore the effect of radiation. However, in the droplet ignition delay experiments described above, it was expected that radiative heat exchange between the furnace walls and the droplet surface was likely significant. However, the numerical modeling results without radiation were still a crucial step and the results were necessary for comparison against other models that have been developed with and without the effect of radiation.

A basic test matrix was developed and implemented to ensure that a range of initial droplet diameters and initial ambient temperature was used that would be consistent with the experiments described in Chater 3. Since radiation effects were ignored in the first set of simulations, emissivity of the droplet and furnace was not necessary as an input for these simulations. Four initial droplet diameters were investigated: 0.5 mm, 1 mm, 2.5 mm, and 5 mm. Ambient temperature ranged from 900 K up to 1900 K. The test matrix is summarized in Table 4.1.

Table 4.1: Test Matrix used for numerical simulations. The matrix was used for runs with and without radiation effects.

Temp (K)	0.5 mm	1.0 mm	2.5 mm	5.0 mm
900				
950				

1000				
1173				
1300				
1500				
1700				
1900				

Temperatures were chosen based on several reasons. First, an even spacing was desired in order to encompass a large range without the need for an infinite number of tests. Second, the split-tube furnace being used in the real-world experimentation (Applied Testing Systems, Inc. Series 3210) is rated to approximately 900 °C, which leads to the 1173 K selection. Lastly, the smaller diameter droplets (0.5 mm and 1 mm) were found to not ignite under a certain temperature due to the lower combustion limit, and a smaller temperature range was used under 1000 K. The test matrix above ensures that each scenario was simulated, and after a run was completed, a simple check mark was placed in the corresponding box. This same test matrix was used for the simulations which included the radiation effects, so for each scenario (no radiation and radiation with varying emissivity levels), 32 simulations were run. In all, 352 simulations were performed.

Once a set of simulations is finished, it is possible to determine the ignition delay of the various size droplets. However, to do so, a definition of when ignition occurs is necessary. For the purposes of this study, ignition was defined as the time when the maximum gas phase temperature began to increase very rapidly. One of the output files

from the numerical model tracks the maximum temperature throughout the entire simulation and places it into tabular form. At the very beginning of the simulation, the maximum temperature matches that of the ambient air, which was preset according to the test matrix. When the fuel droplet ignites, the maximum temperature in the gas phase suddenly exhibits a sudden increase. It is at the start of this temperature spike that ignition is said to have occurred. Figure 4.2 shows the species mass fractions and the temperature of the environment at three separate times: early in the simulation (t=0.3150 s), at ignition (t=0.6410 s), and after ignition (t=0.6810 s). The specific case is a 1 mm methanol droplet with an ambient temperature of 950 °C, including radiation effects. This case was chosen arbitrarily. Table 4.2 contains the simulation results for the computations performed without including radiation.

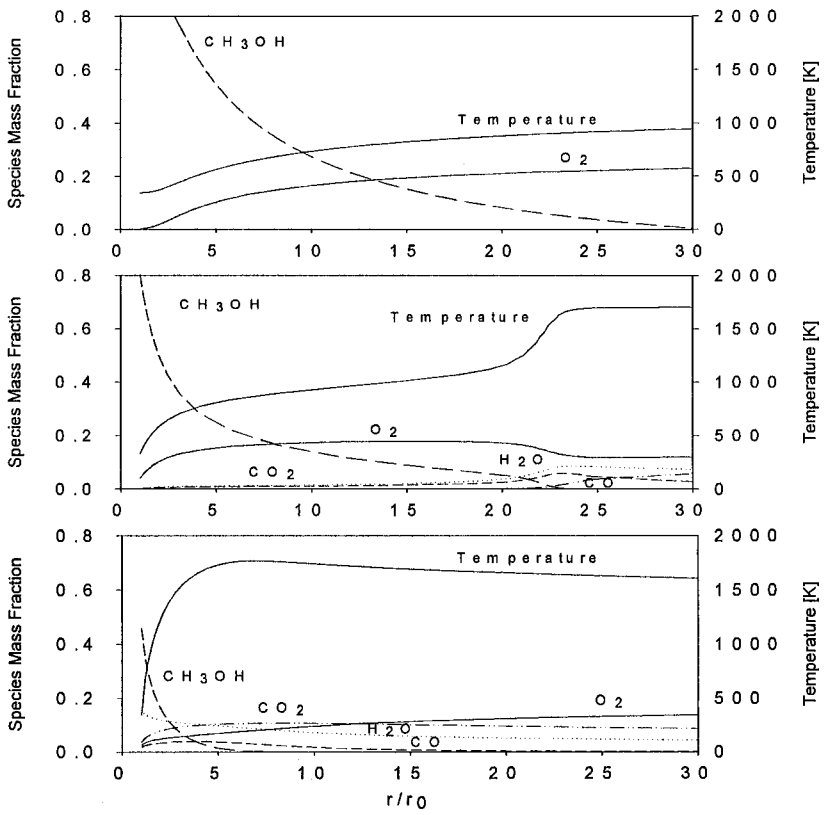

Figure 4.2: Temperature and species in the ambient air surrounding the liquid methanol droplet. Snapshots taken at t=0.3150 (before ignition), t=0.6410 (at ignition), and t=0.6810 (after ignition). 1 mm methanol droplet in 950 °C ambient, including radiation.

Table 4.2: Ignition delay times (in seconds) for a methanol droplet neglecting radiation. (DNI = Did Not Ignite)

Temp (K)	0.5 mm	1.0 mm	2.5 mm	5.0 mm
900	DNI	DNI	2.630	3.080
950	DNI	DNI	0.953	1.240
1000	DNI	0.327	0.449	0.567
1173	0.0307	0.0437	0.0608	0.0777
1300	0.0119	0.0155	0.020	0.0304

1500	3.2e-3	4.0e-3	6.3e-3	0.0118
1700	1.2e-3	1.6e-3	3.1e-3	6.5e-3
1900	8.0e-3	1.3e-3	2.2e-3	4.6e-3

As can be seen Table 4.2, without radiation, the ignition delay time of each size droplet decreases with increasing temperature. This does not quite match up with previously observed phenomena. According to Law [26], at lower temperatures, the larger droplets should ignite first, whereas at the higher temperatures, the smaller droplets should ignite first. Also of interest is the region of temperatures for the 0.5 mm and 1 mm droplets in which the droplets do not ignite. This indicates that somewhere in this temperature range, the temperature became too low to ignite the fuel. Instead, the fuel evaporates beforehand. The data presented above can also be seen in Figures 4.3 and 4.4. Figure 4.3 shows the dependence of ignition delay on the initial ambient temperature. In Figure 4.4, ignition delay is plotted versus initial droplet diameter. As shown, the ignition delay decreases with increasing temperature, but increases with increasing initial diameter.

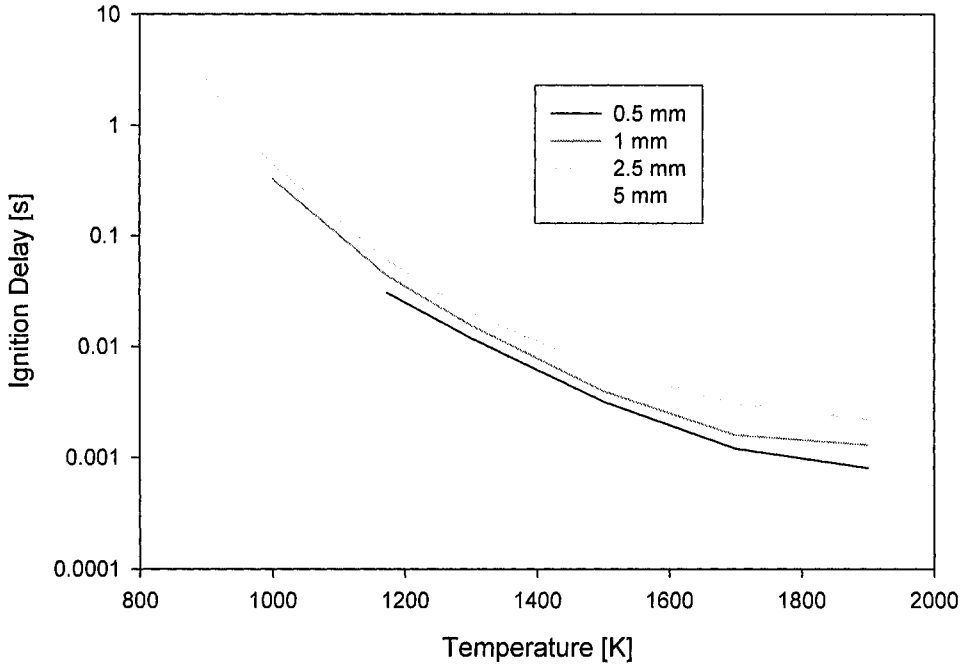

Figure 4.3: Ignition delay vs. ambient temperature of 0.5 to 5.0 mm methanol droplets in air at 900 to 1900 K. (Neglecting radiation)

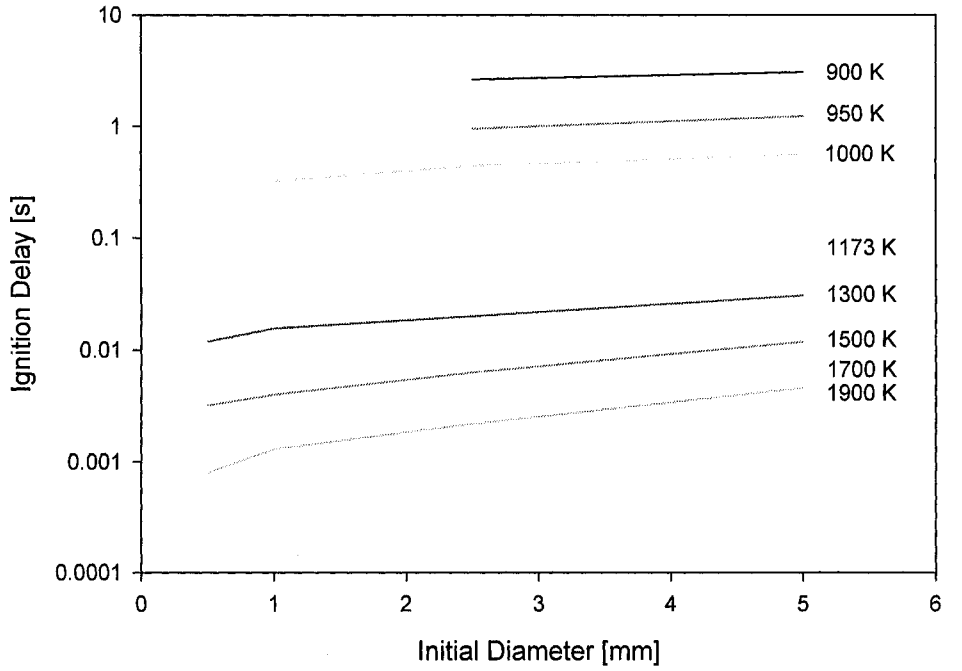

Figure 4.4: Ignition delay vs. initial diameter of 0.5 to 5.0 mm methanol droplets in air at 900 to 1900 K. (Neglecting radiation)

Using the simulations above, it is possible to compare the numerical modeling to the actual 1-g experimentation. Comparisons between the experiments and numerical models will be investigated in Chapter 5.

Section 4.2 – Radiation Effects

4.2.1 - Determination of Radiation Factors

While the above modeling results are reasonable and display the expected trend of ignition delay vs. temperature and initial diameter, they were not expected to agree quantitatively with the experiments of Chapter 3 because of the role of the radiation heat transfer. Marchese and coworkers [56] incorporated gas phase radiation heat transfer into the droplet combustion model by considering the radiative emission from the major gas phase species that emit thermal radiation (CO_2, H_2O and CO). For the droplet ignition calculations, the gas phase radiative emission from these species is negligible because their mole fractions are insignificant prior to the ignition event, which occurs explosively fast. However, in the droplet ignition calculations radiative heat transfer from the hot furnace walls to the cool droplet surface is an important factor, which needed to be considered. Accordingly, a radiative heat transfer model was developed and incorporated into the droplet combustion model as part of the present study. It should be noted that Marchese and coworkers did not include radiative heat transfer from furnace walls (or any other external source) because the droplet combustion experiments that they were simulated were conducted in cool ambient conditions where the droplet surface temperature is roughly equal to the ambient temperature.

To more accurately model the ignition delay experiments described in Chapter 3, radiation heat transfer from the furnace walls to the droplet surface must be included. There are many ways to model radiation in a given system. The simplest scenario between two distinct bodies is given by the basic equation governing radiation exchange between two blackbodies:

$$q_{ij} = A_i F_{ij} \sigma (T_i^4 - T_j^4) \tag{4.6}$$

where q_{ij} is the net rate at which radiation leaves surface i and is absorbed by surface j, A_i the area of surface i, F_{ij} the view factor between the two surfaces, σ the Stefan-Boltzmann constant, and T_i and T_j the temperatures of the respective surfaces. This calculation doesn't correspond well with the current system setup. Neither the fuel droplet nor the furnace walls can be considered a black body. Rather, both are diffuse, gray surfaces that form an enclosure (the tube furnace completely surrounds the fuel droplet), so modification of the basic equation is necessary. Further derivation of the enclosed surfaces scenario yields the following equation:

$$q_{12} = \frac{\sigma (T_1^4 - T_2^4)}{\frac{1-\varepsilon_1}{\varepsilon_1 A_1} + \frac{1}{A_1 F_{12}} + \frac{1-\varepsilon_2}{\varepsilon_2 A_2}} \tag{4.7}$$

where q_{12} is the radiation exchange between surfaces 1 and 2, σ the Stefan-Boltzmann constant, A_1 and A_2 the surface areas, T_1 and T_2 the respective temperatures, F_{12} the view factor between the surfaces, and ε_1 and ε_2 the emissivities of the given surface.

Three separate cases were considered before implementation into the droplet combustion code. In the first case, the fuel droplet was estimated to be a small object in a very large cavity. In this instance, the above equation can be rewritten as:

$$q_{12} = \sigma A_1 \varepsilon_1 (T_1^4 - T_2^4) \tag{4.8}$$

where the fuel droplet is defined as surface 1 and the "infinite" tube furnace is surface 2. The second case describes two concentric spheres forming an enclosure. Once again, defining the fuel droplet to be surface 1 and the "spherical" tube furnace to be surface 2, Equation 4.7 can be modified to [57]:

$$q_{12} = \frac{\sigma A_1 (T_1^4 - T_2^4)}{\frac{1}{\varepsilon_1} + \frac{1-\varepsilon_2}{\varepsilon_2}\left(\frac{r_1}{r_2}\right)^2} \tag{4.9}$$

where r_1 and r_2 are the radii of the fuel droplet and the furnace, respectively. The final case involves estimating the fuel droplet to be a sphere inside a long cylinder (in this case, the tube furnace). The surface nomenclature stays the same. Equation 4.7 can then be rewritten as:

$$q_{12} = \frac{\sigma A_1 (T_1^4 - T_2^4)}{\frac{1-\varepsilon_1}{\varepsilon_1} + \frac{1}{F_{12}} + \frac{1-\varepsilon_2}{\varepsilon_2}\left(\frac{2r_1^2}{hr_2}\right)} \tag{4.10}$$

where h is the length of the tube furnace. For the concentric spheres case, the view factor F_{12} is identically equal to 1 for the concentric regardless of the size of the spheres. For the sphere inside a cylinder, however, the view factor F_{12} depends on the size of the cylinder is calculated from the following equation [58]:

$$F_{12} = \frac{1}{\sqrt{1+R^2}}$$

(4.11)

$$R = \frac{r}{a}$$

where r is the radius of the cylinder and a is half its length. The full derivations can be found in the Appendix.

The final case (equations 4.10 and 4.11) was chosen to be implemented into the code because it most closely resembled the physical configuration of the experimental setup (Figure 4.3). The lone difference lies in the fact that equations 4.10 and 4.11 were derived assuming the furnace was an open cylinder, whereas the actual experimental setup has ends that are neither completely open nor closed. The injection end of the furnace opens prior to injection and then partially closes after injection. The other end of the furnace contains a sapphire window.

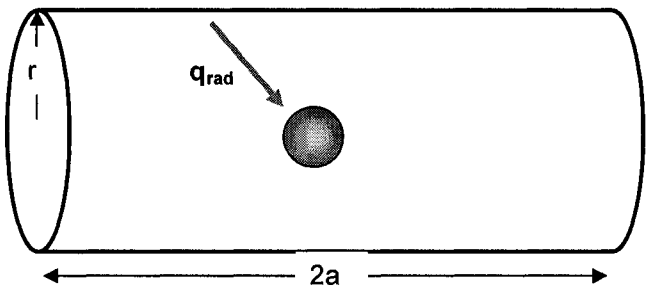

Figure 4.5: Basic representation of the furnace and droplet geometry used in the radiation heat transfer model.

4.2.2 - Simulations with Radiation

The simulations including radiation were run exactly the same as the simulations that neglected radiation effects. A total of 32 simulations were run for each set of radiation boundary conditions, which in this case are the emissivity of the fuel droplet and the emissivity of the furnace walls. Exact values for these emissivities were not readily available from the literature, but were estimated based on several sources. To make up for the lack of a definitive value for the emissivities, a range of values were used instead. Calculations were performed with two different values for the emissivity of the droplet (0.95 and 0.90), and five different values for the furnace walls (0.50, 0.40, 0.30, 0.20, and 0.05).

These emissivity values were chosen based on published values of similar materials. The furnace walls are made up of Alumina (Al_2O_3). However, the exact form of the Alumina was not known. Published values for it range from around 0.20 to 0.50, hence the highest and second-lowest levels chosen. The lowest level of 0.05 was chosen in an effort to determine what effect, if any, a significantly low wall emissivity would have on the ignition delay. The two intermediate levels were included in order to form a more complete picture of the effects of the Alumina emissivity. It should also be noted that the furnace walls also include some exposed Nichrome wire, which has different emissivity values than alumina.

The fuel droplet (in this case, methanol) was harder to determine. No published value for emissivity of liquid methanol was available in the literature. However, previous work done by Konishi, *et al* [59] found the emissivity of liquid propanol to be 0.95. This does not necessarily mean that the emissivity of liquid methanol would be the same, but

when coupled with the fact that almost all liquids thus far published have had an emissivity of greater than 0.90, it becomes a reasonable estimation. Therefore, it may be safe to assume that the emissivity of liquid methanol is somewhere in the 0.90 to 0.95 range, and thus these two values were used.

Since the droplet surface temperature does not vary significantly for an evaporating methanol droplet and the furnace temperature is fixed, it was possible to estimate the rates of heat transfer from the proposed radiation model for a wide range of emissivities prior to incorporating the model into the droplet combustion model In order to investigate the effects of varying emissivity levels, an Excel worksheet was set up to calculate the radiative heat loss with the assumption of the droplet and furnace being blackbodies, as well as relaxing that assumption and run calculations with furnace emissivity values ranging from 0.01 to 0.99. In the interest of time, only one ambient temperature was used in these calculations. A value of 1200 K was arbitrarily used. Figure 4.6 shows the results of these calculations. Each set of emissivity calculations was normalized against the radiative heat loss of the blackbody scenario. As can be seen in Figure 4.6, there is little variation above a furnace emissivity of 0.2. However, at or below that level shows a decrease in the radiation exchange which may or may not alter the ignition delay times significantly. And while this information could justify reducing the number of furnace emissivity levels being simulated, the entire range was simulated using the droplet combustion model. . In fact, this is the reason that the emissivity level of 0.05 was introduced into the modeling study.

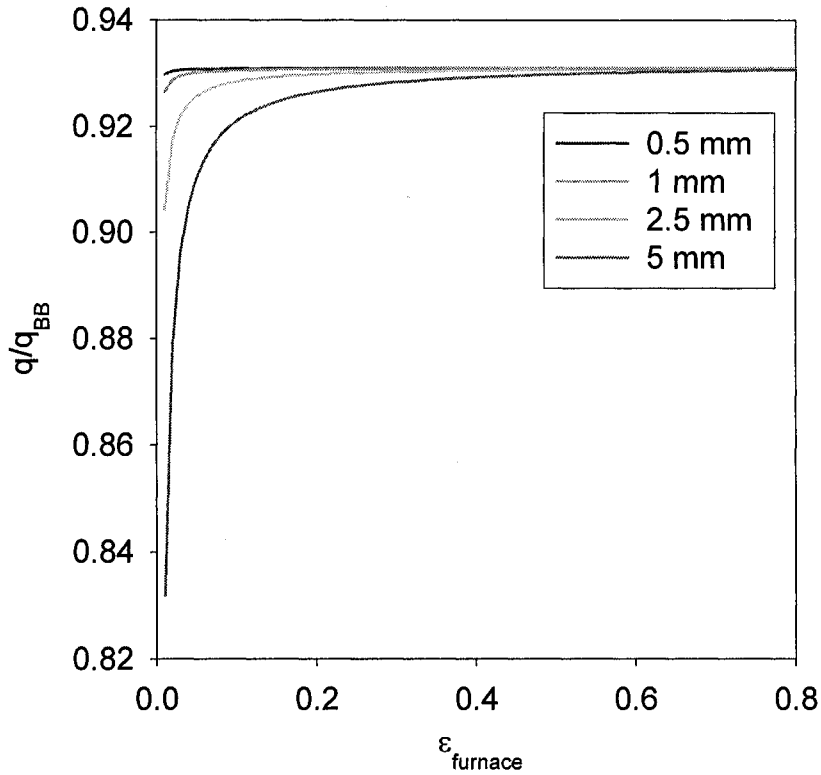

Figure 4.6: Effects of the furnace emissivity against normalized radiative heat exchange.

Since there are so many variables (ambient temperature, initial droplet size, emissivity of the droplet, and emissivity of the furnace walls), it is beneficial to look at each case specifically. For the first set of experiments, the droplet emissivity was held constant at 0.95 and the emissivity of the furnace walls was varied over the range of 0.05 to 0.50. For each furnace wall emissivity, the entire 32-point simulation matrix was performed.

4.2.2.1 – Methanol Simulations with Droplet Emissivity of 0.95

The first case analyzed was the effect of the furnace wall emissivity of 0.5 on the ignition delay with respect to each ambient temperature/initial droplet size pairing.

Table 4.3: Ignition delay times (in seconds) for a methanol droplet with droplet emissivity of 0.95 and furnace emissivity of 0.5. (DNI = Did Not Ignite)

Temp (K)	0.5 mm	1.0 mm	2.5 mm	5.0 mm
900	DNI	DNI	2.24	1.220
950	DNI	0.6410	0.4010	0.4320
1000	DNI*	0.2100	0.1620	0.1710
1173	0.0127	0.0137	0.0158	0.0200
1300	3.8e-3	4.0e-3	5.3e-3	7.8e-3
1500	9.0e-4	1.0e-3	1.7e-3	3.4e-3
1700	3.0e-4	4.0e-4	9.0e-4	1.8e-3
1900	1.0e-4	2.0e-4	6.0e-4	1.1e-3

There are several things to note here. First is the ignition delay corresponding to an initial droplet size of 1.0 mm and an ambient temperature of 950 K. In the previous case (neglecting radiation – Table 4.2), this scenario resulted in the droplet evaporating instead of igniting. With the inclusion of radiation effects, the droplet now ignites. Second, the value marked with an asterisk (*), corresponding to an initial droplet size of 0.5 mm and ambient temperature of 1000 K, is inconclusive. In the process of the simulations, the code becomes hung up at the point at which ignition may or may not occur. This specific scenario was run multiple times, all with the same inconclusive result. It appears as though the droplet may ignite, as there is a slight temperature increase at that point; however, the code ceases to function properly and it is not known if the temperature would continue to increase rapidly, signaling ignition of the droplet.

This code hang up appears in all instances of this specific scenario (0.5 mm, 1000 K), regardless of the furnace emissivity used.

In summary, it can be seen that at the lower temperatures, the bigger droplets ignite earlier than the smaller droplets (if at all), while at the higher temperatures, the smaller droplets ignite before the larger droplets. This corresponds with Law's work [26], which also states that the larger droplets suffer significant mass loss before igniting at the lower temperatures, whereas at the higher temperatures, there is very little mass loss before ignition. The data in Table 4.3 can be plotted in two different ways: ignition delay versus ambient temperature (Figure 4.7), and ignition delay versus initial droplet size (Figure 4.8). Figure 4.7 shows that as the temperature increases, the difference in ignition delay times between the various droplet sizes also increases. Also note that several of the lines cross each other, indicating that at lower temperatures, the larger droplets ignite first, while the smaller droplets are first to ignite at the higher temperatures. This phenomenon is also present in Figure 4.8.

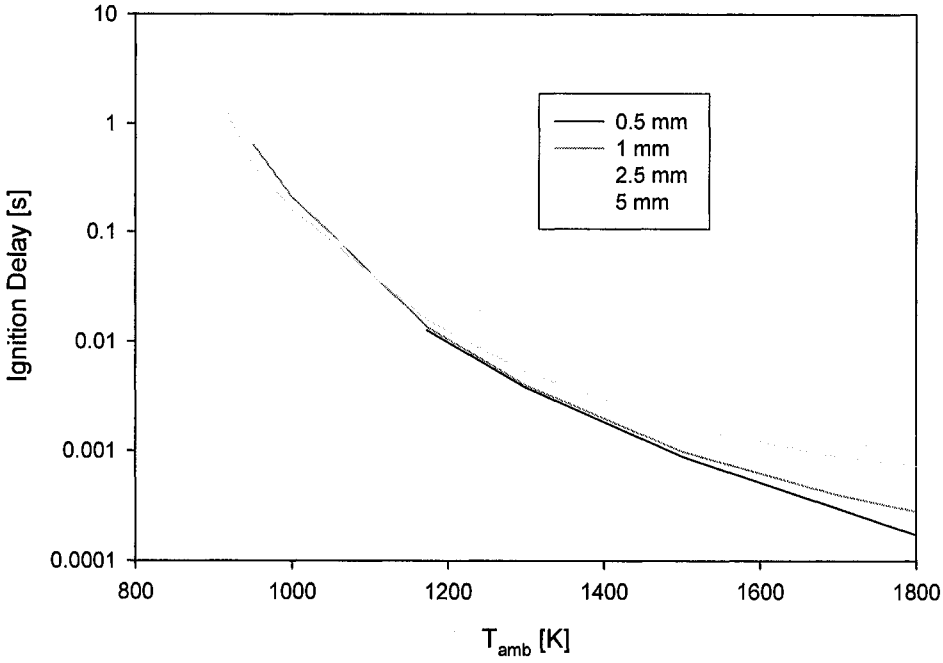

Figure 4.7: Ignition delay vs. ambient temperature of 0.5 to 5.0 mm methanol droplets in air at 900 to 1900 K (Droplet emissivity of 0.95, furnace emissivity of 0.5)

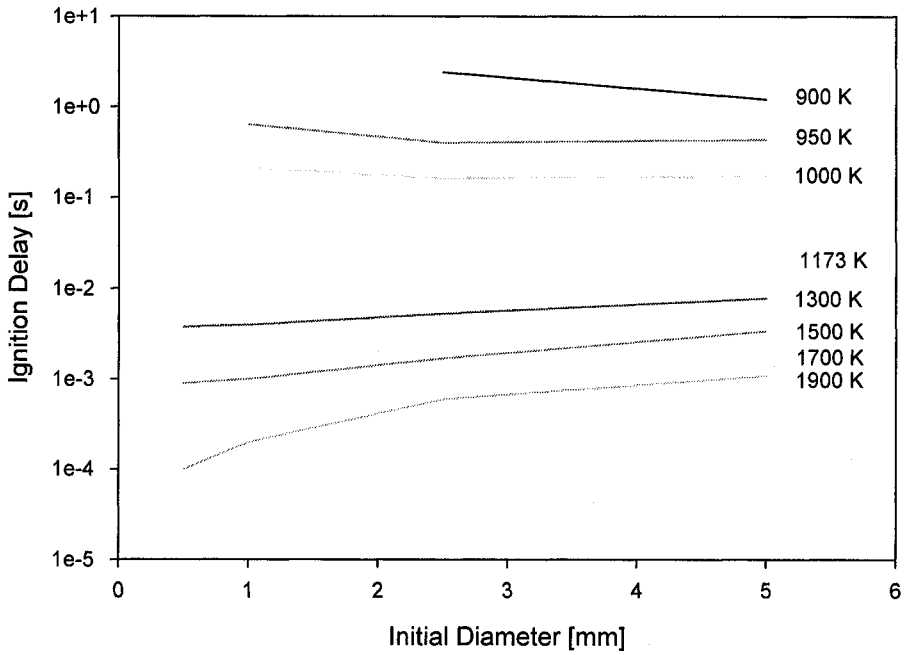

Figure 4.8: Ignition delay vs. initial diameter of 0.5 to 5.0 mm methanol droplets in air at 900 to 1900 K. (Droplet emissivity of 0.95, furnace emissivity of 0.5)

Keeping the droplet emissivity at 0.95, but lowering the furnace emissivity to 0.4 slightly lowers some of the ignition delay times, but not all. The following table shows the ignition delay times with any changes italicized.

Table 4.4: Ignition delay times (in seconds) for a methanol droplet with droplet emissivity of 0.95 and furnace emissivity of 0.4. (DNI = Did Not Ignite)

Temp (K)	0.5 mm	1.0 mm	2.5 mm	5.0 mm
900	DNI	DNI	***2.23***	***1.21***
950	DNI	0.6410	***0.4060***	***0.4230***
1000	DNI*	0.2100	***0.1630***	***0.1740***
1173	***0.0125***	0.0137	0.0158	0.0200
1300	3.8e-3	4.0e-3	5.3e-3	7.8e-3
1500	9.0e-4	1.0e-3	***1.8e-3***	3.4e-3
1700	3.0e-4	4.0e-4	9.0e-4	1.8e-3
1900	1.0e-4	2.0e-4	***5.0e-4***	***1.2e-3***

As can be seen, the differences between the ignition delay times are very insignificant. They can, in fact, be attributed to uncertainty in the way ignition delay is defined in the model. Again, the 0.5 mm, 1000 K case is inconclusive. Figure 4.9 shows the ignition delay times plotted against ambient temperature, while Figure 4.10 is plotted against initial droplet size.

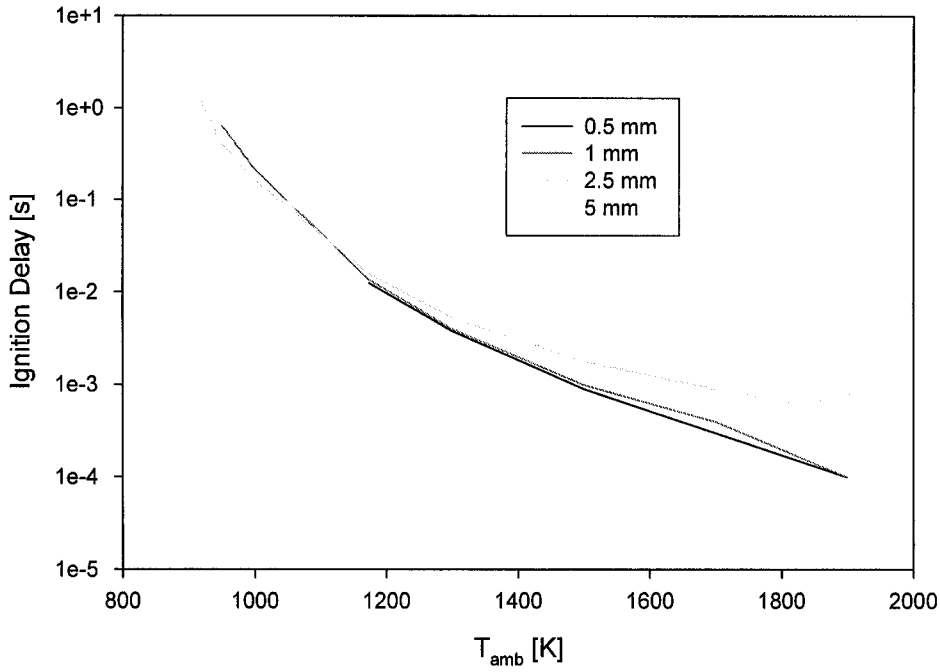

Figure 4.9: Ignition delay vs. ambient temperature of 0.5 to 5.0 mm methanol droplets in air at 900 to 1900 K (Droplet emissivity of 0.95, furnace emissivity of 0.4)

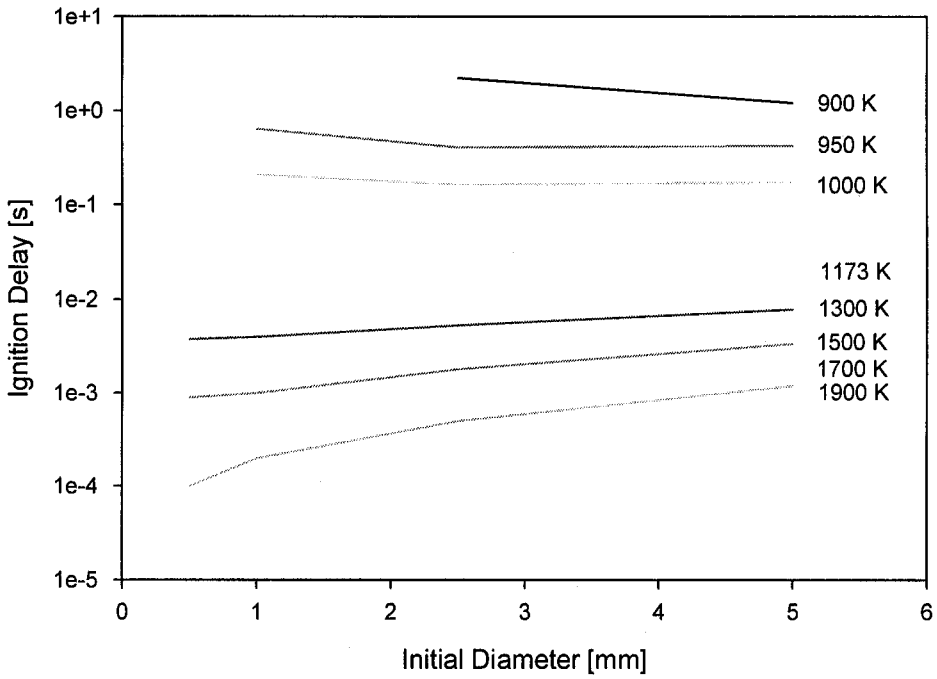

Figure 4.10: Ignition delay vs. initial diameter of 0.5 to 5.0 mm methanol droplets in air at 900 to 1900 K (Droplet emissivity of 0.95, furnace emissivity of 0.4)

Lowering the furnace emissivity once again, this time to 0.3, yields very similar results. Table 4.5 shows the ignition delay times, with any changes italicized.

Table 4.5: Ignition delay times (in seconds) for a methanol droplet with droplet emissivity of 0.95 and furnace emissivity of 0.3. (DNI = Did Not Ignite)

Temp (K)	0.5 mm	1.0 mm	2.5 mm	5.0 mm
900	DNI	DNI	2.23	1.21
950	DNI	***0.6390***	***0.4050***	***0.4310***
1000	DNI*	***0.2110***	0.1630	***0.1750***
1173	0.0125	0.0137	0.0158	0.200
1300	3.8e-3	4.0e-3	***5.4e-3***	7.8e-3
1500	9.0e-4	1.0e-3	***1.7e-3***	***3.3e-3***
1700	3.0e-4	4.0e-4	9.0e-4	***1.9e-3***
1900	1.0e-4	2.0e-4	5.0e-4	1.2e-3

The same trends continue in the 0.3 furnace emissivity case as the previous two cases. The 0.5 mm, 1000 K pairing once again does not run to completion, and there are slight differences in a handful of the ignition delay times. Again, these variations may be attributed to the way ignition delay is defined in the code, as well as the fact that the code uses a variable time-step. Figure 4.11 shows the ignition delay times plotted against the ambient temperature, and the same inverse trend is present. The ignition delay is then plotted against the initial diameter in Figure 4.12.

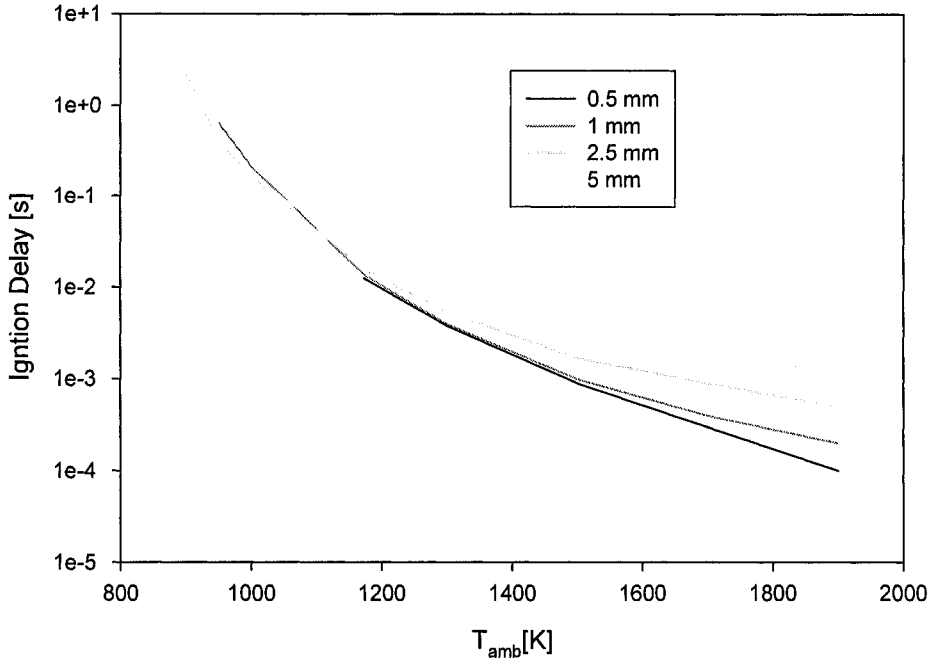

Figure 4.11: Ignition delay vs. ambient temperature of 0.5 to 5.0 mm methanol droplets in air at 900 to 1900 K (Droplet emissivity of 0.95, furnace emissivity of 0.3)

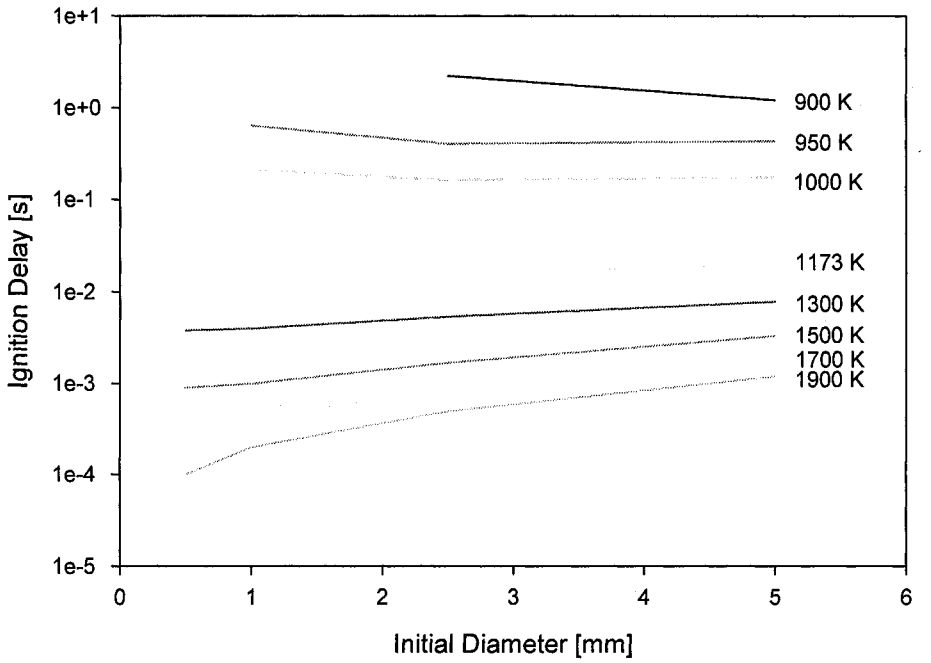

Figure 4.12: Ignition delay vs. initial diameter of 0.5 to 5.0 mm methanol droplets in air at 900 to 1900 K (Droplet emissivity of 0.95, furnace emissivity of 0.3)

Once again, the wall emissivity is lowered, this time to the 0.20 level. As can be seen in the table below, the same trends continue with this case as well.

Table 4.6: Ignition delay times (in seconds) for a methanol droplet with droplet emissivity of 0.95 and furnace emissivity of 0.2. (DNI = Did Not Ignite)

Temp (K)	0.5 mm	1.0 mm	2.5 mm	5.0 mm
900	DNI	DNI	2.24	***1.22***
950	DNI	***0.6410***	***0.3950***	***0.4250***
1000	DNI*	0.2110	***0.1610***	***0.1720***
1173	0.0125	0.0137	0.0158	***0.0201***
1300	3.8e-3	4.0e-3	5.4e-3	***7.6e-3***
1500	9.0e-4	1.0e-3	1.7e-3	***3.2e-3***
1700	3.0e-4	4.0e-4	9.0e-4	1.9e-3
1900	1.0e-4	2.0e-4	5.0e-4	***1.1e-3***

The same graphical trends can be seen in Figures 4.13 (ignition delay vs. ambient temperature) and 4.14 (vs. initial droplet diameter). Finally, the furnace emissivity is lowered to its final value of 0.05. This is the last set of simulations with the droplet emissivity held at 0.95.

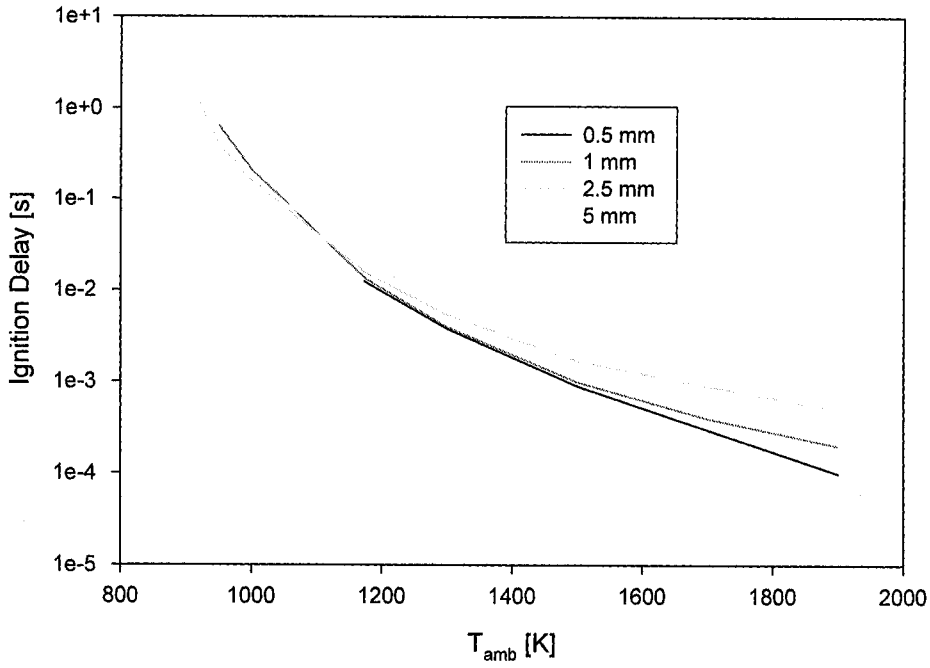

Figure 4.13: Ignition delay vs. ambient temperature of 0.5 to 5.0 mm methanol droplets in air at 900 to 1900 K (Droplet emissivity of 0.95, furnace emissivity of 0.2)

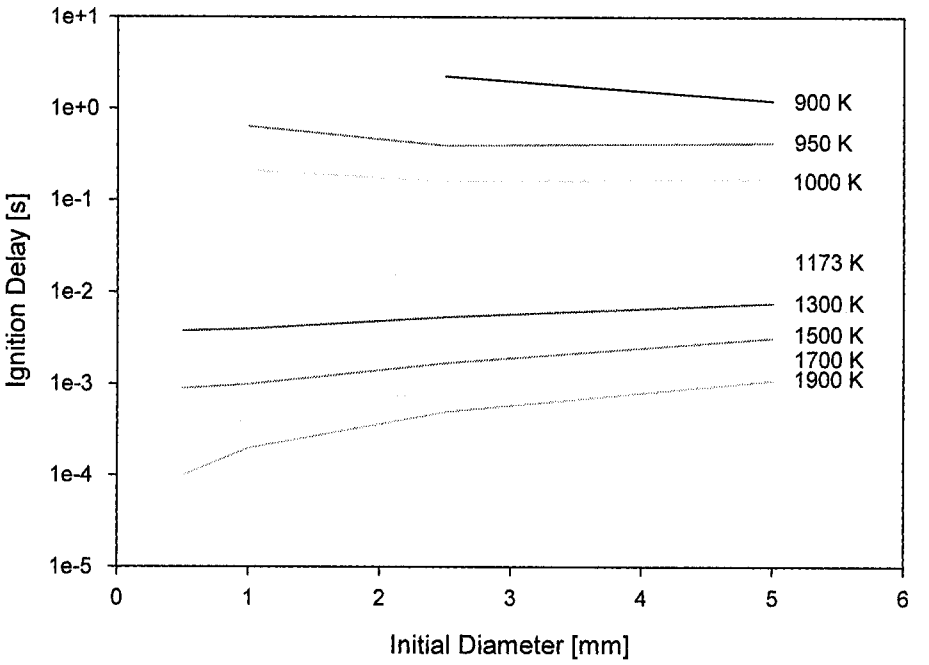

Figure 4.14: Ignition delay vs. initial diameter of 0.5 to 5.0 mm methanol droplets in air at 900 to 1900 K (Droplet emissivity of 0.95, furnace emissivity of 0.2)

Table 4.7: Ignition delay times (in seconds) for a methanol droplet with droplet emissivity of 0.95 and furnace emissivity of 0.05. (DNI = Did Not Ignite)

Temp (K)	0.5 mm	1.0 mm	2.5 mm	5.0 mm
900	DNI	DNI	2.24	***1.21***
950	DNI	***0.6420***	***0.4030***	***0.4270***
1000	DNI*	***0.2120***	0.1610	***0.1730***
1173	0.0125	0.0137	***0.0159***	***0.0200***
1300	3.8e-3	4.0e-3	***5.3e-3***	***8.0e-3***
1500	9.0e-4	1.0e-3	1.7e-3	***3.5e-3***
1700	3.0e-4	4.0e-4	9.0e-4	1.9e-3
1900	1.0e-4	2.0e-4	5.0e-4	***1.2e-3***

Contradictory to what was previous thought, lowering the furnace emissivity to a value lower than 0.2 did not have as great an effect on the ignition delay time. As was previously shown, while the presence of radiation in general has a great effect on the droplet ignition delay time, the furnace emissivity (which is unknown) has little effect on the ignition delay time. In essence, the furnace emissivity can be neglected while still maintaining the level of accuracy that is desired. Figures 4.15 and 4.16 show the ignition delay plotted against ambient temperature and initial droplet diameter, respectively.

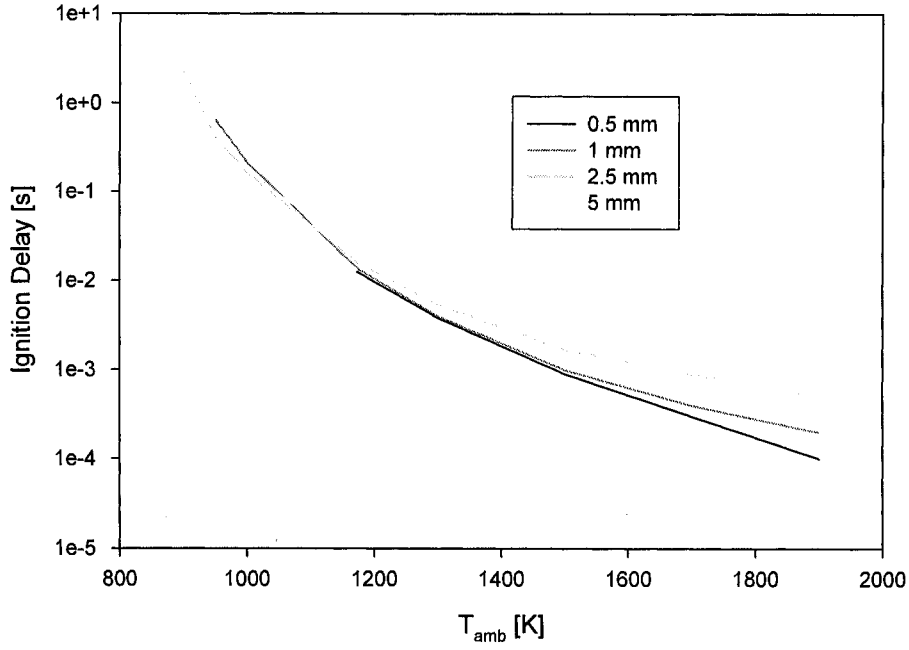

Figure 4.15: Ignition delay vs. ambient temperature of 0.5 to 5.0 mm methanol droplets in air at 900 to 1900 K (Droplet emissivity of 0.95, furnace emissivity of 0.05)

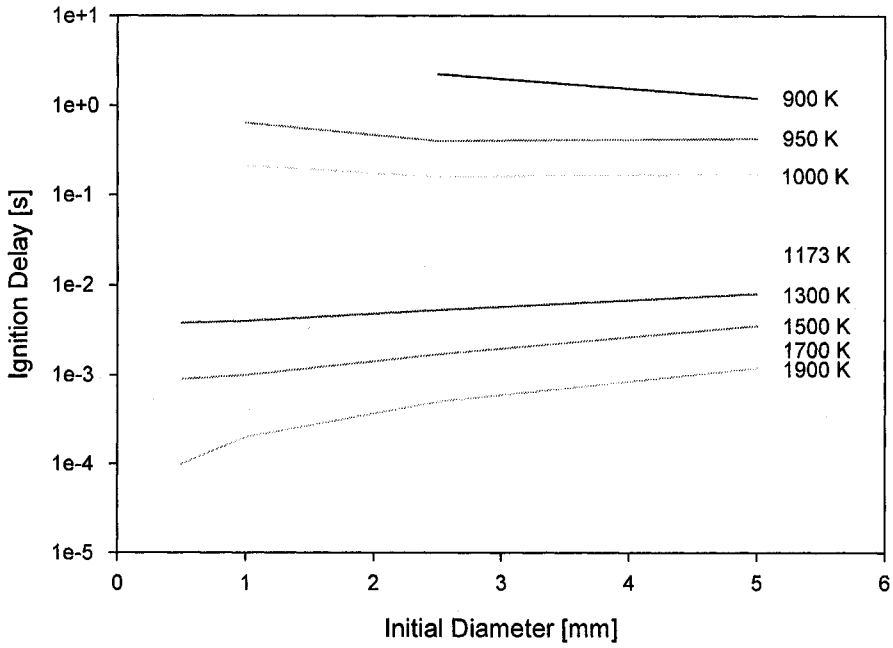

Figure 4.16: Ignition delay vs. initial diameter of 0.5 to 5.0 mm methanol droplets in air at 900 to 1900 K (Droplet emissivity of 0.95, furnace emissivity of 0.05)

4.2.2.2 – Methanol Simulations with Droplet Emissivity of 0.90

The next sets of calculations were performed to determine the effect of the emissivity of the liquid droplet surface on the calculated ignition delay. Setting the droplet emissivity to 0.90, all the above tests were run once again. Starting from the highest level, the furnace emissivity is set to 0.5.

Table 4.8: Ignition delay times (in seconds) for a methanol droplet with droplet emissivity of 0.90 and furnace emissivity of 0.5. (DNI = Did Not Ignite)

Temp (K)	0.5 mm	1.0 mm	2.5 mm	5.0 mm
900	DNI	DNI	2.24	***1.18***
950	DNI	***0.6520***	0.4240	***0.4260***
1000	DNI*	0.2020	0.1620	0.1710
1173	***0.0126***	0.0137	***0.0159***	***0.0202***
1300	3.8e-3	4.0e-3	***5.0e-3***	7.8e-3
1500	9.0e-4	1.0e-3	***1.8e-3***	3.4e-3
1700	3.0e-4	4.0e-4	9.0e-4	***1.9e-3***
1900	1.0e-4	2.0e-4	6.0e-4	***1.2e-3***

The highlighted entries in the above table are slightly different from the values that appear in the case of a droplet emissivity of 0.95 with a furnace emissivity of 0.5. Again, these values are not significantly different, and seem to indicate that there is not a strong correlation between droplet emissivities and ignition delay times. Figures 4.17 and 4.18 show the relationship between the ignition delay with respect to initial ambient temperature and initial droplet diameter, respectively.

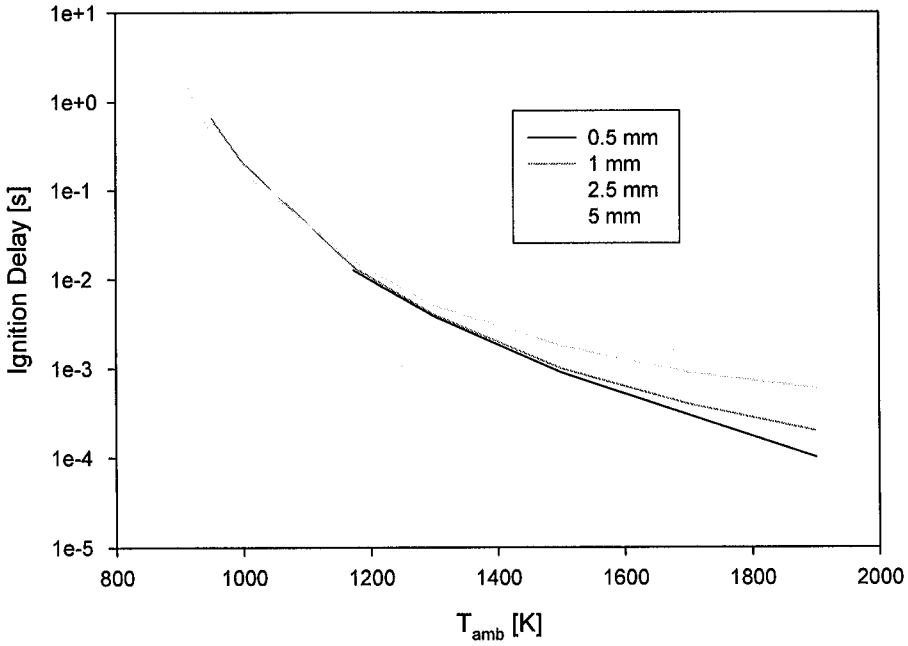

Figure 4.17: Ignition delay vs. ambient temperature of 0.5 to 5.0 mm methanol droplets in air at 900 to 1900 K (Droplet emissivity of 0.90, furnace emissivity of 0.5)

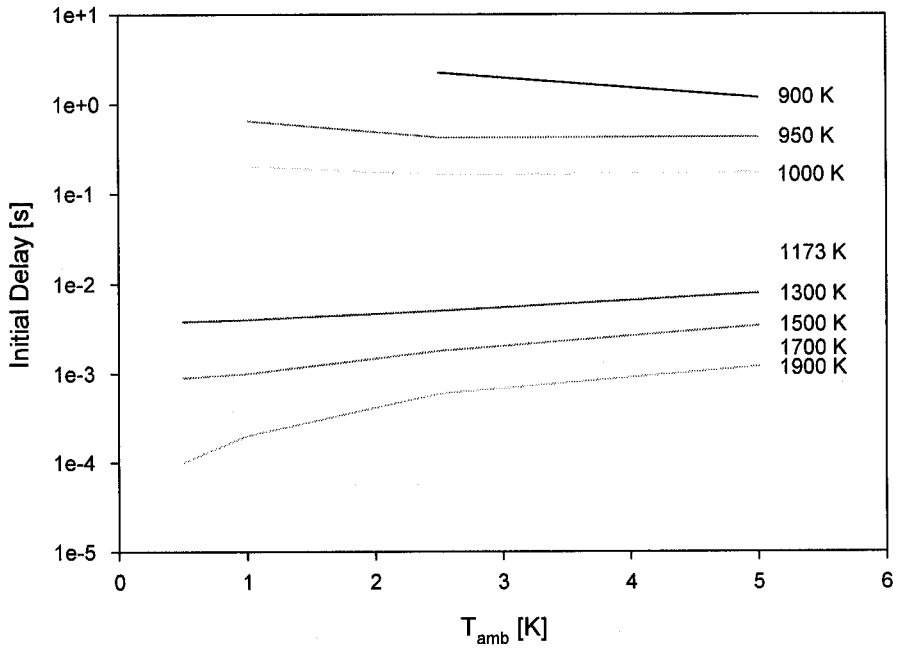

Figure 4.18: Ignition delay vs. initial diameter of 0.5 to 5.0 mm methanol droplets in air at 900 to 1900 K (Droplet emissivity of 0.90, furnace emissivity of 0.5)

Drawing any conclusions from just one set of data is premature. Therefore, the furnace emissivity was dropped down to 0.4 and the simulations were run again. The ignition delay time for this case are shown in the following table.

Table 4.9: Ignition delay times (in seconds) for a methanol droplet with droplet emissivity of 0.90 and furnace emissivity of 0.4. (DNI = Did Not Ignite)

Temp (K)	0.5 mm	1.0 mm	2.5 mm	5.0 mm
900	DNI	DNI	***2.24***	***1.19***
950	DNI	***0.6530***	***0.4180***	***0.4280***
1000	DNI*	***0.2040***	***0.1620***	***0.1760***
1173	***0.0126***	0.0137	***0.0159***	0.0200
1300	3.8e-3	4.0e-3	***5.0e-3***	***7.7e-3***
1500	9.0e-4	1.0e-3	1.8e-3	***3.3e-3***
1700	3.0e-4	4.0e-4	9.0e-4	***1.9e-3***
1900	1.0e-4	2.0e-4	***6.0e-4***	1.2e-3

Again, the highlighted values correspond to differences in ignition delay times when compared with the same furnace emissivity in the 0.95 droplet emissivity case, and as was seen in the 0.5 furnace emissivity simulations, the difference in ignition delay times is very small. The graphs for this case follow.

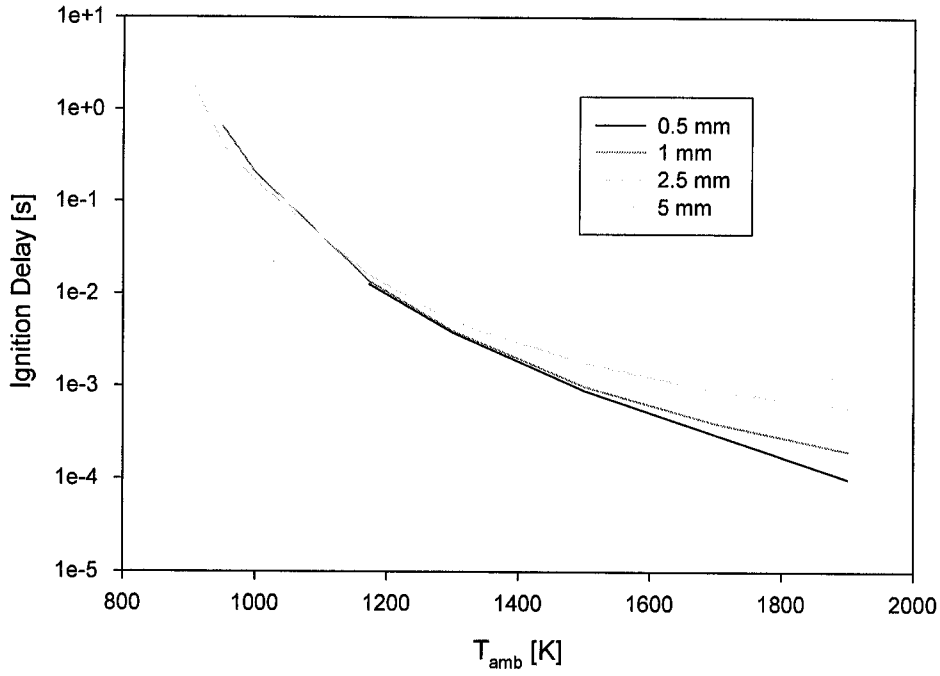

Figure 4.19: Ignition delay vs. ambient temperature of 0.5 to 5.0 mm methanol droplets in air at 900 to 1900 K (Droplet emissivity of 0.90, furnace emissivity of 0.4)

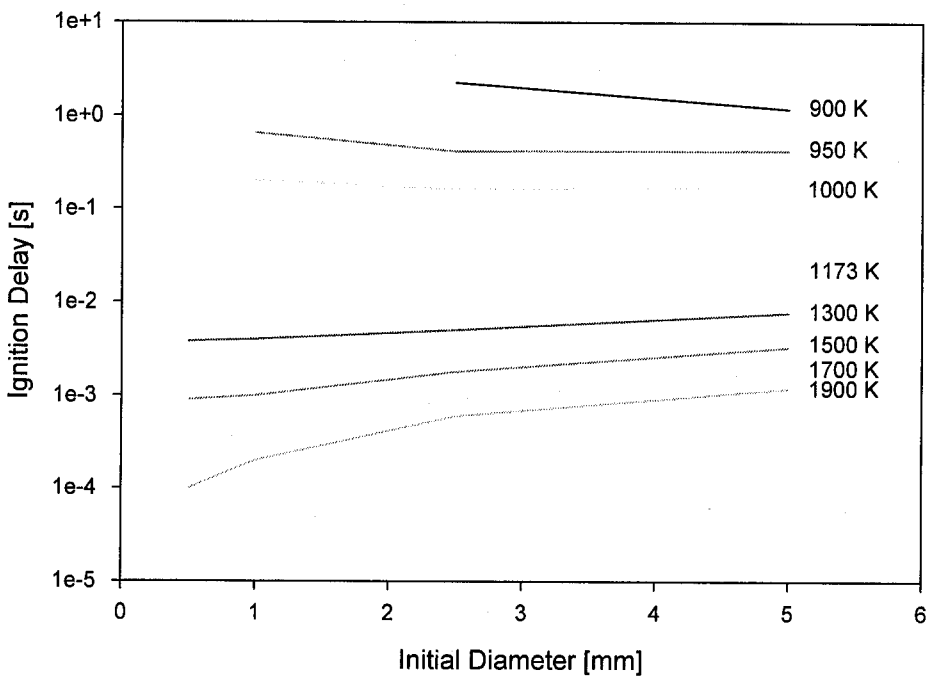

Figure 4.20: Ignition delay vs. initial diameter of 0.5 to 5.0 mm methanol droplets in air at 900 to 1900 K (Droplet emissivity of 0.90, furnace emissivity of 0.4)

More simulations were run for the 0.90 droplet emissivity scenario (0.3, 0.2 and 0.05 furnace emissivity), but will not be discussed here. For completion, the data and graphs for these simulations can be found in the appendix.

Section 4.3 – Discussion

Based on the above simulations above, it is quite obvious that the ignition delay times, while significantly lowered with the addition of radiation effects, are not significantly affected by any reasonable changes in the emissivity of either the droplet itself or the surrounding furnace. This is a result of the specific geometry of the droplet ignition experiments described in Chapter 3. The droplet is relatively small when compared to the internal cavity of the furnace. Because of this geometry (and the fact that it can be accurately assumed that the droplet emissivity is greater than 0.9), radiative heat transfer to the droplet surface will be significant for all values of furnace wall emissivity greater than approximately 0.2. This explains the similarities of ignition delay times for all the calculations presented in the previous section.

Overall, the simulations run with radiation effects agree with what has previously been observed in experimentation; that at lower temperatures, the bigger droplets ignite faster than smaller droplets, while at the higher temperatures, the opposite is true. These results were not observed for the calculations in which radiation was neglected.

Figure 4.21 compares the calculated ignition delay times for droplet size of 0.5 mm and 5 mm for calculations performed with and without the effect of radiation heat

transfer from the furnace walls to the droplet surface. For the calculations shown in Figure 4.21, the droplet emissivity was 0.95 and the furnace emissivity was 0.50. As discussed above, the calculations showed surprisingly little sensitivity to the furnace emissivity and the droplet emissivity is likely greater than 0.9. Accordingly, the results of Figure 4.21 are presented with a high degree of certainty, despite the lack of certainty in the furnace emissivity. Appendix A contains the graphs for the 1.0 mm, 2.5 mm, and 5.0 mm droplet sizes.

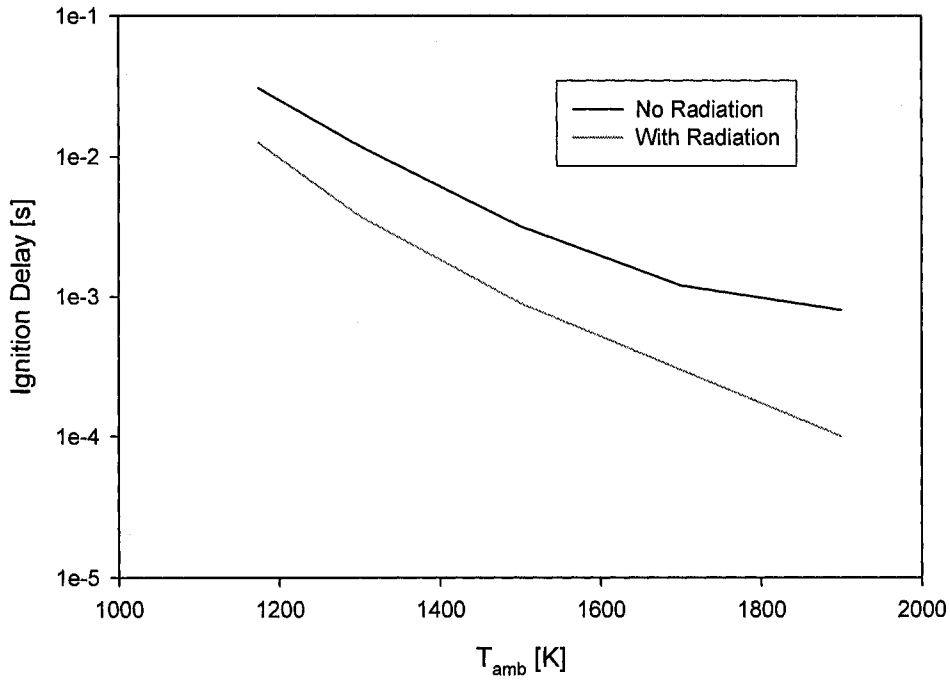

Figure 4.21: Radiation effect on the ignition delay of a 0.5 mm methanol droplet for droplet emissivity of 0.95 and furnace emissivity of 0.50.

As can be seen, there is a significant decrease in ignition delay times with the inclusion of the furnace radiation effect. Comparisons between the simulations and experiments are made in the following chapter.

It should be noted that ignition delay of <0.1 seconds is virtually impossible to measure experimentally. Even if high speed photography is available, the transient effects associated with droplet insertion render ignition delays of less than 0.1 second meaningless for comparison with a spherically symmetric model. Accordingly, furnace temperatures, droplet diameters and fuels are typically chosen that yield ignition delays between 0.1 and 5 seconds. The results of the modeling study suggest that methanol is a very difficult fuel for ignition delay experiments, since at the low temperature it evaporates prior to ignition and at the high temperatures its predicted ignition delay is too small to observe experimentally.

Chapter Five

Conclusions and Future Work

Section 5.0 – Conclusions

Due to differences in conditions between the numerical model and the experimental model (microgravity versus normal gravity), it is very difficult to compare the model with experimental results. In the experiment, temperatures in the range of 900-980 °C (1173-1253 K) resulted in ignition delay times ranging from 0.4-1.8 s. Conversely, the predicted ignition delay times at 1173 K in were much shorter than the experimental data (~0.03 s neglecting radiation, ~0.01 s with radiation). These sets of data won't be able to be fully compared until the experimental setup is ready to be tested in the drop tower facility constructed in Rowan Hall.

However, there is still the issue of the discrepancies between the ignition delay times of the methanol experiment. When looking at similar initial conditions (initial diameter and initial ambient temperature), it can be observed that there are some significant differences on the ignition delay times. For example, Table 5.1 shows several (but not all) similar initial conditions and their respective ignition delay times.

Table 5.1: Several examples of methanol tests with similar initial conditions, but varying ignition delay times.

Test Run	Droplet Size [mm]	Temperature [°C]	Ignition Delay [s]
02:23	1.1516	895	1.5667
02:27	1.2337	895	0.6333
03:25	1.3190	920	1.2333
03:30	1.3833	920	0.8333

03:47	1.3931	984	0.8000
03:49	1.4475	983	0.4333

Based on their initial conditions, one would expect that the ignition delay times of these tests would be closer. But, as shown above, there is a considerable difference in each case. The first pair (Test Runs 02:23 and 02:27) have the same initial temperature and their initial diameters vary by only 0.0821 mm, but the ignition delay time of Test Run 02:23 is more than double that of Test Run 02:27. Even more surprising is that the 02:23 case has the smaller diameter droplet, which should have resulted in a shorter ignition delay than 02:27.. In the second pair (Test Runs 03:25 and 03:30) the ambient temperature is once again the same, and the initial diameters vary by only 0.0643 mm, yet the same phenomena can be found as in the first pair. The case with the smaller diameter (03:27) takes longer to ignite. Finally, this can be seen again in the third pairing. Reasons for these discrepancies will be discussed shortly.

The following graph shows a comparison between the measured (1-g) ignition delay times and calculated ignition delay times (0-g, with and without radiation).

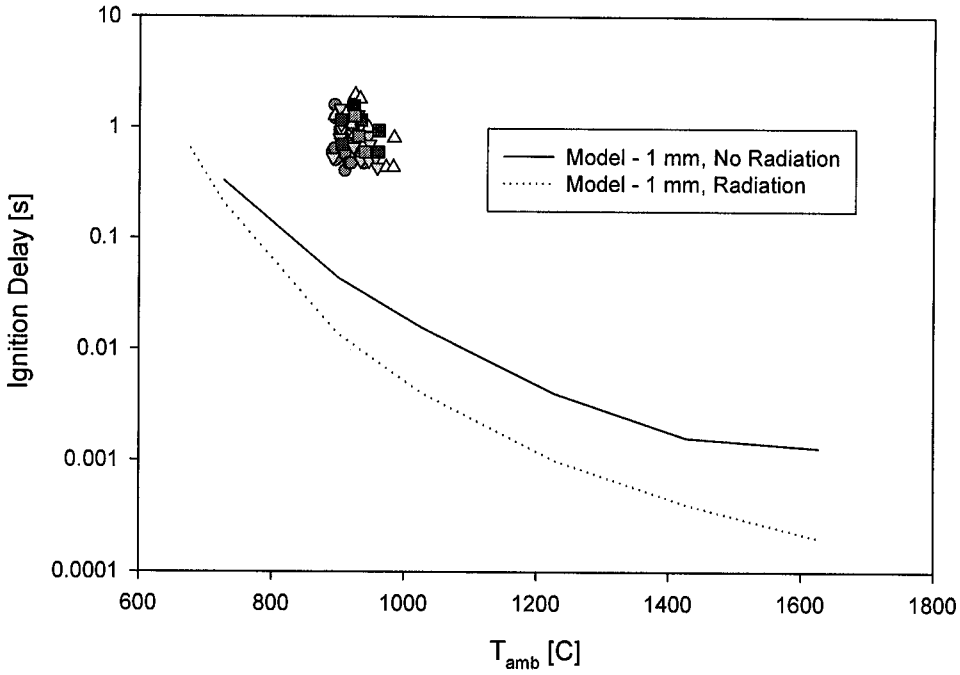

Figure 5.1: Results from the methanol experiment compared against the numerical model. The solid line represents simulations neglecting radiation effects, while the dotted line represents those with radiation included.

Figure 5.1 shows the same data as Figure 3.19, but uses a log scale on the y-axis in order to provide a means to show the numerical results on the same graph. The temperature range has been increased in order to allow for all the numerical modeling data be shown. As can be seen, there is a large difference between the 1-g experiments and the microgravity numerical models. Based on these observations, it is very important that a complete setup for microgravity be developed in order to validate the numerical modeling.

The following figure places Figures 3.20 and 3.22 side-by-side. These two figures show the ignition delay as a function of ambient temperature, divided into nominal diameter ranges.

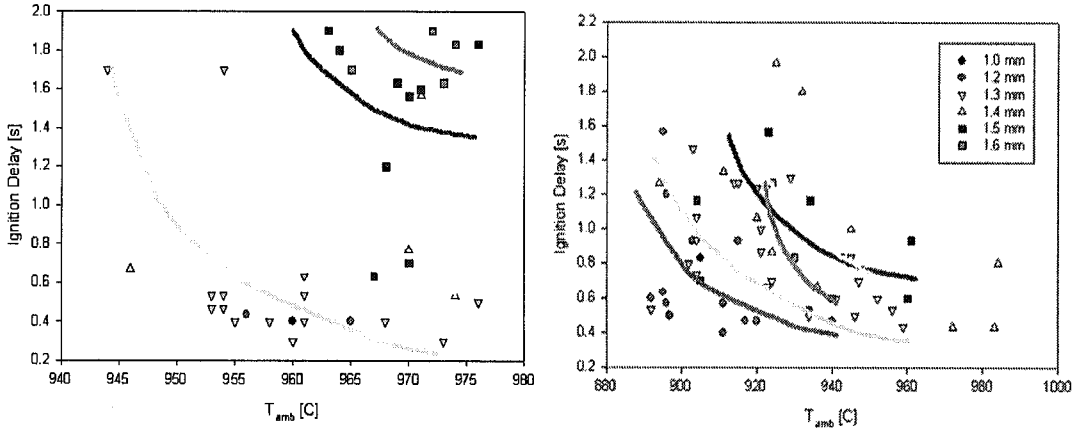

Figure 5.2: Ignition delay vs. ambient temperature, grouped by diameter range and shown with linear regression lines. Methanol is on the left, methyl butyrate on the right. (For a better look, please see Figures 3.20 and 3.22.)

The distinct regions of nominal droplet diameter is still present in the methyl butyrate data, while the methanol data still shows a lot of scattering. From the trend lines, it appears as though the methanol droplets have a higher dependence on ambient temperature than the methyl butyrate droplets do, but it is difficult to draw any conclusions due to the scatter of the methanol droplet data, and the fact that there is less data for the methyl butyrate droplets. In order to validate the above trends, more experiments need to be conducted.

With the data above, and further testing, it will be possible to begin the task of determining a valid chemical kinetic model for methyl butyrate. This model could then be used to determine how this particular fuel will react when introduced into an engine and ran under normal, real world conditions. The model can also be used to determine why biodiesel fuels produce more NO_x, while at the same time reduce CO, HC, and PM emissions. As for the methanol tests, further validation of the numerical model is not possible until the experiment is introduced into a microgravity condition.

5.0.1 – Sources of Uncertainty in the 1-g Experiments

As mentioned in the previous section, there are discrepancies among the individual experiments. In order to explain these differences, sources of experimental uncertainty must be investigated. One such factor has been discussed previously, and that is the introduction of water into the pure methanol. If the methanol had absorbed water from the atmosphere, then the ignition delay times may be affected. The effect of water dissolution into the methanol prior to conducting the experiments would be to increase the ignition delay. Therefore, water dissolution could explain the longer than expected ignition delay times observed herein, but it likely does not explain the lack of repeatability in the experiments.

A second cause behind these discrepancies may be human error. As of now, the experiment is not automated, and while this is accounted for in the varying diameters and temperatures, there is still one area that hasn't been accounted for. Currently, the droplet is inserted into the furnace via the injection forks, which in turn are inserted manually. This is the area in which human error may be responsible. It is nearly impossible for a person to insert the injection forks at the same velocity and same timing for all experiments. As a result, some droplets may be in the ambient temperature sooner than others, and therefore igniting sooner as well. Moreover, some droplets will have been subjected to greater convective flows than others prior to the ignition event. Such convective flows will increase heat transfer to the droplet, but could also modify the gaseous fuel layer surrounding the droplet, so the overall effect of convection during injection is unclear. Regardless, the entire process needs to be automated to ensure repeatability and to remove the human element from the experiment. Thirdly, as has

been previously mentioned, better temporal resolution in the measured ignition delay might be realized through the use of high speed video camera(s). The Hitachi CCD camera and the Xybion camera only record at 30 frames per second, which is too slow for this sort of experiment. In order to get a more accurate reading on the ignition delay times, it is necessary to include a high-speed camera in the system. A high-speed camera can record much faster (up to ~1000 fps on some, even higher on others) and would provide an accuracy of 1/1000 of a second, rather than the 1/30 of a second accuracy currently in the experiment.

Another source of error is the transient heating of the glass fiber used to hold the droplet. Due to its small size, the glass rod and bead become subject to large swings in temperature. Rapid heating and cooling occur when the experiment is injected and taken out, respectively. Any residual heat that remains in the glass fiber will have an adverse effect on the ignition delay testing. For example, the fiber will be at room temperature (~25 °C) at the start of the experiments. However, after injecting the entire apparatus into the 900-950 °C tube furnace, the temperature of the fiber will be higher. The difference in these temperatures will result in transient internal heating of the droplet as it sits on the fiber, but before injection. Therefore, a droplet on a hot fiber will have different initial conditions than the same size droplet on fiber at room temperature. The fact that the larger bead size quartz rods did not ignite might also show that heat transfer from the quartz rod to the droplet was significant since this effect should increase substantially with the rod/bead size.

To alleviate this effect, future suspended droplet experiments will employ a means to cool and/or measure the fiber temperature prior to each experiment. Ironically,

the silicon carbide fiber system results in much less transfer of heat from the fiber to the droplet because of the very small fiber diameters. Unfortunately, the silicon carbide fibers are difficult to use for more than one experiment.

Since these experiments are being run in 1-g conditions, convection effects can alter the ignition delay times of the test droplets. In the current setup, there are two sources of convection: convection brought about by insertion of the forks at a particular velocity, and convection as a result of a non-uniform temperature distribution throughout the entire tube furnace. These effects will always be present in the 1-g experiments, but their effect could be lessened by changing the design of the experiment. Currently, the temperature profile is asymmetric with respect to the vertical centerline of the furnace. On one end is an aluminum plate which houses the sapphire window, while the other end is covered with the insulator for the majority of the time. The insulator contains the heat, while the aluminum allows for conduction through it. The next section deals with these sources of error, as well as other improvements and experiments to be done.

Section 5.1 – Future Work

The goal of this thesis was to develop a means in which to conduct ignition delay experiments in both normal gravity and microgravity, as well as run simulations. At this time, only normal gravity experiments have been conducted. There is much more work that needs to be done in order to meet the overall goals of the entire study. First and foremost, a means to automate the entire experiment is necessary. This will take away human error and increase repeatability. It will also be necessary due to the fact that once

the experiment is ready to be run using the newly developed Rowan 1 -Second Drop Tower, it will be impossible to run this experiment manually. More specifically, an automated device to grow a droplet and inject it into the furnace are needed, as well as a triggering device to simultaneous drop the experimental rig and begin filming with the two (or possibly more) cameras.

A high speed camera needs to be added to the experiment in order to assure a more accurate reading of the ignition delay time. Currently, the use of a standard CCD camera only allows for a recording speed of 30 frames per second. A high speed camera capable of delivering up to 1000 fps would be more suited to the task. Also, incorporation of a third camera must be investigated. With the current two camera system (1 CCD, 1 UV), it is only possible to see the ignition event and the initial diameter outside the furnace, or the ignition event and the diameter just before ignition. Due to transient heating through the fiber, or simply convection effects, these two diameters will almost certainly be different. Therefore, the addition of a second CCD camera would allow for the measurement of both diameters, which could then be compared to each other in order to determine any evaporation of the droplet prior to ignition.

The entire experimental package must also be redesigned as necessary to determine how it will be placed on the instrumentation table on the drop rig. The current 1-g bench configuration did not take into consideration any space constraints. The rig must also be outfitted with a power source to provide enough power to run the cameras and other automated devices on board. The steel button that is currently being used to secure the drop rig to the electromagnet must also be modified. It will need to be made

slightly bigger than the desired contact area with the electromagnet to ensure a secure connection between the two.

The issue of a drag shield must also be addressed. Preliminary calculations show that the inclusion of a simple nose cone can reduce the g levels slightly (Figure 5.2), but an entire drag shield would reduce these levels even more. Secondary calculations were made to determine the effect of a drag shield on the rig. Both sets of calculations can be seen in the Appendix. For the case of the rig by itself, a drag coefficient of 1.05 was used, while for the rounded nose, a drag coefficient of 0.85 was used.

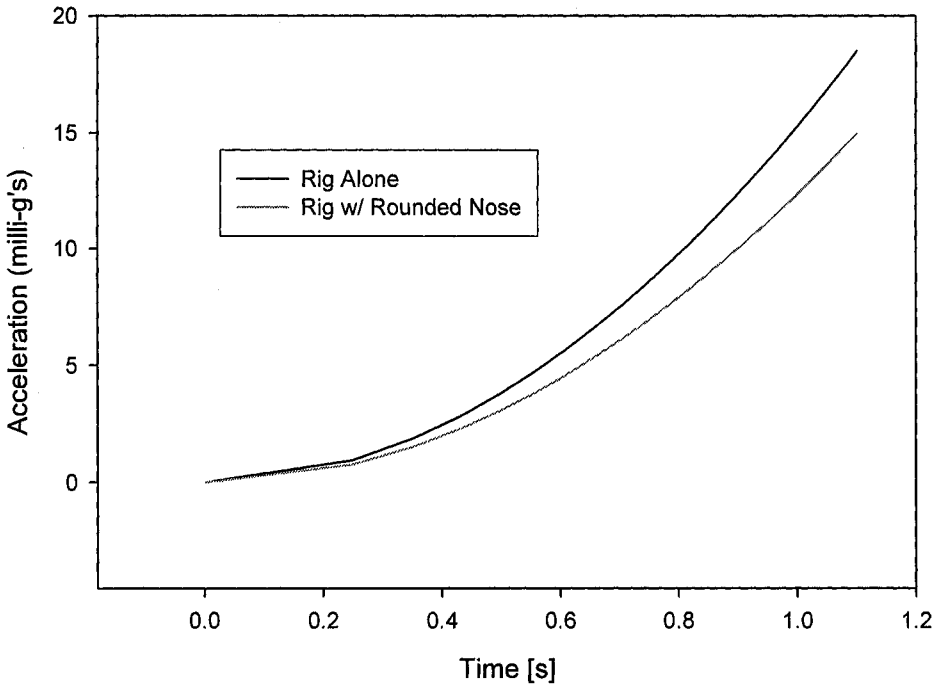

Figure 5.3: G levels vs time.

Several changes need to be made to the drop tower itself. First off, due to recent construction and rearrangement of the High Bay, the drop tower needed to be moved over ten feet or so. Because of this, the current support structure of the hoist/release

mechanism must be redesigned to fit in a different area of the room. Other designs of the support structure are also being considered. A means of securing the swinging access doors must also be addressed. Currently, there is no latch holding the doors shut. There is also the possibility that more blast gates need to be added to allow for the release of air from the air bag once the drop rig comes into contact with it.

Finally, additional test runs in both normal gravity and microgravity must be made. Propanol and ethanol fuels also need to be studied in both configurations, as well as other types of biodiesel surrogate fuels.

References

1. *Annual Energy Review 2004.* (2005) Energy Information Administration. Office of Energy Markets and End Use, US Department of Energy, Washington, DC.

2. Graboski, M.S., McCormick, R.L. (1998). Combustion of Fat and Vegetable Oil Derived Fuels in Diesel Engines. *Prog. Energy Combust. Sci.*, **28**, pp. 125-164.

3. A Comprehensive Analysis of Biodiesel Impact on Exhaust Emissions. (2002). EPA420-P-02-001. Oct. 2002.

4. Syzbist, J., Simmons, J., Druckenmiller, M., Al-Qurashi, K., Boehman, A., and Scaroni, A. (2003). Potential Methods for NOx Reduction from Biodiesel. **SAE 2003-01-3025**.

5. Choi, C., Bower, G., and Reitz, R. (1997). Effects of Biodiesel Blended Fuels and Multiple Injections on D.I. Diesel Engines. **SAE 970218**.

6. Syzbist, J., Boehman, A., Taylor, J., and McCormick, R. (2005). Evaluation of Formulation Strategies to Eliminate the Biodiesel NOx Effect. *Fuel Processing Technology,* **86**, 1109.

7. Heywood, J.B., Internal Combustion Engine Fundamentals. 1st Edition, McGraw-Hill, 1988.

8. McCormick, R.L., Graboski, M.S., Alleman, T.L., Herring, A.M., Tyson, K.S. (2001). Impact of Biodiesel Source Material and Chemical Structure on Emissions of Criteria Pollutants from a Heavy-Duty Engine. *Environmental Science and Technology*, **35**, No. 9.

9. Fisher, E., Pitz, W., Curran, H. and Westbrook, C. (2000). Detailed Chemical Kinetic Mechanism for Combustion of Oxygenated Fuels. *Proc. Combust. Inst.* **28**, 2000.

10. Marchese, A.J., Angioletti, M., and Dryer, F.L. *Work in Progress Poster, 30th Symposium (International) on Combustion, Chicago, IL, July 2004.*

11. Marchese, A.J. (1996). *Single and Multicomponent Liquid Droplet Combustion: Detailed Kinetic Modeling and Microgravity Experiments.* Ph. D. Dissertation, Dept. of Mechanical and Aerospace Engineering, Princeton Univ., Princeton, NJ.

12. Williams, F.A. (1973). The Combustion of Liquid Fuels: A Review. *Combust. And Flame,* **21**, 1.

13. Faeth, G.M. (1977). Current Status of Droplet and Liquid Combustion. *Prog. Energy Combust. Sci.* **3**, 191.

14. Law, C.K. (1982). Recent Advances in Droplet Vaporization and Combustion. *Prog. Energy Combust. Sci.* **8**, pp. 171-201.

15. Vaughn, T. (2006). Biodiesel and Biodiesel Surrogate Fuel Droplets: 1-g and 0-g Test Results, Master's Thesis (In Progress), Rowan University, 2006.

16. Spalding, D.B. (1953). The Combustion of Liquid Fuels. *Fourth Symposium (International) on Combustion*, Williams and Wilkens, Co., Baltimore, MD, p. 847.

17. Godsave, G.A.E. (1953). Studies of the Combustion of Drops in a Fuel Spray: The Burning of Single Droplets of Fuel. *Fourth Symposium (International) on Combustion,* Williams and Wilkens, Co., Baltimore, MD, p. 818.

18. Chung, S.H. and Law, C.K. (1986). An Experimental Study of Droplet Extinction in the Absence of External Convection. *Combustion and Flame*, **64**, 237.

19. Avedisian, C.T., Yang, J.C., and Wang, C.H. (1988). On Low-Gravity Droplet Combustion. *Proc. R. Soc. Lond.*, A **420**, 183.

20. Cho, S.Y., Choi, M.Y., and Dryer, F.L. (1990). The Extinction of a Free Methanol Droplet in Microgravity. *23rd Symposium (International) on Combustion,* The Combustion Institute, Pittsburgh, PA, p. 1611.

21. Hara, H. and Kumagai, S. (1990). Experimental Investigation of Free Droplet Combustion under Microgravity. *23rd Symposium (International) on Combustion,* The Combustion Institute, Pittsburgh, PA, p. 1605.

22. Dietrich, D.L., Dryer, F.L., Haggard, J.B., Jr., Nayagam, V., Shaw, B.D., and Williams, F.A. (1996). Droplet Combustion Experiments on Spacelab. *26th Symposium (International) on Combustion,* The Combustion Institute, Pittsburgh, PA, p. 1201.

23. Law, C.K., Chung, S.H., and Srinivasan, N. (1980). Gas Phase Quasi-Steadiness and Fuel Vapor Accumulation Effects in Droplet Burning. *Combustion and Flame,* **38**, 173.

24. Law, C.K. (1976). Unsteady Droplet Combustion with Droplet Heating. *Combust. and Flame,* **26**, 219.

25. Law, C.K. (1975). Asymptotic Theory for Ignition and Extinction in Droplet Burning. *Combustion and Flame*, **24**, 89.

26. Law, C.K. (1978). Theory of Thermal Ignition in Fuel Droplet Burning. *Combust. and Flame*, **31**, 285.

27. Card, J.M. and Williams, F.A. (1992). Asymptotic Analysis of the Structure And Extinction of Spherically Symmetric N-Heptane Diffusion Flames. *Combust. Sci. and Tech.* **84**, 91.

28. Yang, B., Seshardi, K., and Peters, N. (1992). The Asymptotic Structure of Premixed Methanol-Air Flames. *Combustion and Flame*, **91**, 382.

29. Zhang, B.L., Card, J., and Williams, F.A. (1995). Application of Rate-Ratio Asymptotics to the Prediction of Extinction of Methanol Droplet Combustion. *Combustion and Flame*, **105**, 267.

30. Aldred, J.W., Patel, J.C., and Williams, A. (1971). The Mechanism of Combustion of Droplets and Spheres of Liquid N-Heptane. *Combustion and Flame*, **17**, 139.

31. Ludwig, D.E., Bracco, F.V., and Harrje, D.T. (1975). Nitric Oxide and Consumption Measurements Within Diffusion Flames Around Simulated Ethanol and Ethanol-Pyridine Droplets. *Combustion and Flame*, **25**, 107.

32. Choi, M.Y. (1992). *Droplet Combustion Characteristics under Microgravity and Normal-Gravity Conditions.* Ph.D. Dissertation, Dept. of Mechanical and Aerospace Engineering, Princeton Univ., Princeton, NJ.

33. *The Early History of Drop Towers.* NASA Glenn Research Center 2.2 Second Drop Tower: A Gateway to Space, http://microgravity.grc.nasa.gov/drop2/history.

34. Dietrich, D.L., Ross, H.D., and T'ien, J.S. (1994). The Burning of a Candle in Reduced Gravity: Space Shuttle and Drop Tower Results. *AIAA 94-0429.*

35. Law, C.K. and Faeth, G.M. (1994). Opportunities and Challenges of Combustion in Microgravity. *Progress in Energy and Combustion Science*, **20**, p 65.

36. Braeucker, Richard. *Research under Microgravity Conditions.* http://www.richard-braeucker.de/jamic1-e.htm.

37. *Microgravity Experiments using Drop-Tower Test Facility.* http://spaceinfo.jaxa.jp/note/kankyo/e/kan9812_rakkasetubi_e.html.

38. The Drop Tower "Bremen" at ZARM. http://131.176.49.1/spaceflight/map/ao/dtowbre.htm.

39. NASA Glenn Research Center 2.2 Second Drop Tower. http://microgravity.grc.nasa.gov/drop2/tour.

40. University of Texas at Austin Drop Tower Facility. http://www.ae.utexas.edu/research/FloImLab/drpt.html.

41. Faeth, G.M. and Olson, D.R. (1968). The Ignition of Hydrocarbon Fuel Droplets in Air. *Transactions of the ASME*, 1793.

42. Kumagai, S., Sakai, T., and Okajima, S. (1971). Combustion of Free Fuel Droplets in a Freely Falling Chamber. *13th Symposium (International) on Combustion*, The Combustion Institute, Pittsburgh, PA, p. 779.

43. Green, G.J., Takahashi, F., Walsh, D.E., and Dryer, F.L. (1989). An Aerodynamic Droplet Device for Generating Mono-disperse Fuel Droplets. *Rev. Sci. Instrum.*, **60**, 646.

44. Jackson, G., and Avedisian, C.T. (1993). Experiments on the Effect of Initial Droplet Diameter of Spherically Symmetric Droplet Combustion of Sooting Fuels. *31st Aerospace Sciences Meeting and Exhibit*, Reno, NV, *AIAA-93-0130*.

45. Choi, M.Y., Dryer, F.L., Haggard, J.B., Jr. (1990). Observations on a Slow Burning Regime for Hydrocarbon Droplets: n-Heptane/Air Results. *23rd Symposium (International) on Combustion*, The Combustion Institute, Pittsburgh, PA, p.1611.

46. Xu, G., Ikegami, M., Honma, S., Ikeda, K., Dietrich, D.L., and Struk, P.M. (2004). Sooting Characteristics of Isolated Droplet Burning in Heated Ambients under Microgravity. *International Journal of Heat and Mass Transfer*, **47**, 5807.

47. Urban, B.D., Kroenlein, K., Kazakov, A., Dryer, F.L., Yozgatligil, A., Choi, M.Y., Manzello, S.L., Lee, K., and Dobashi, R. (2004). Sooting Behavior of Ethanol Droplet Combustion at Elevated Pressures under Microgravity Conditions. *Microgravity Science and Technology*, **15**, No. 3, 12.

48. Lee, K., Jensen, K., and Choi, M.Y. (1995). Effects of Sooting in Droplet Combustion. *NASA Conference Publication*, No. 10174, p 53.

49. Lee, K., Manzello, S.L., and Choi, M.Y. (1997). Effects of Sooting and Radiation on Droplet Combustion. *NASA Conference Publication*, No. 10194, p. 461.

50. Yozgatligil, A., Park, S., and Choi, M.Y. (2004). Burning and Sooting Behavior of Ethanol Droplet Combustion under Microgravity Conditions. *Combust. Sci. and Tech.*, **176**, 1985.

51. Held, T.J. and Dryer, F.L. (1994). An Experimental and Computational Study of Methanol Oxidation in the Intermediate and High Temperature Regimes. *25th Symposium (International) on Combustion*, p. 901.

52. Marchese, A.J., Dryer, F.L, and Nayagam, V. (1999). Numerical Modeling of

Isolated n-Alkane Droplet Flames: Initial Comparisons with Ground and Space-Based Microgravity Experiments. *Combustion and Flame*, **116**, 432.

53. Cho, S.Y., Yetter, R.A., and Dryer, F.L. (1990). Mathematical Modeling of Liquid Droplet Combustion in Microgravity. *Mathl. Comput. Modelling*, **14**, 790.

54. Marchese, A.J. and Dryer, F.L. (1996). The Effect of Liquid Mass Transport on the Combustion and Extinction of Bi-Component Droplets of Methanol and Water. *Combustion and Flame*, **105**, 104.

55. Marchese, A.J., Dryer, F.L., Nayagam, V., and Colantonia, R.O. (1996). Hydroxyl Radical Chemiluminescence Imaging and the Structure of Microgravity Droplet Flames. *Proc. Combust. Inst.* **26**, 1219.

56. Marchese, A.J. and Dryer, F.L. (1997). The Effect of Non-Luminous Thermal Radiation in Microgravity Droplet Combustion. *Combust. Sci. and Tech.*, **124**, 1-6, 371.

57. Incropera, F.P. and Dewitt, D.P. Fundamentals of Heat and Mass Transfer, Fifth Edition. John Wiley and Sons, 2002.

58. Modest, M.F. Radiative Heat Transfer. McGraw-Hill, Inc., 1993.

59. Konishi, T., Ito, A., and Saito, K. (2000). Transient Infrared Temperature Measurements of Liquid-Fuel Surfaces: Results of Studies of Flames Spread Over Liquids. *Applied Optics*, **39**, No. 24.

Appendix

Section A.0 – Calculations

A.0.1 - Initial Drop Tower Calculations

The following text and calculations are direct from a MathCad file.

Before we can effectively design and insrument any type of release mechanism, deceleration mechanism, or anything else thereof, we must run preliminary calculations on the basic physics of the drop.

First off, we're looking for the amount of time that the rig will be in free fall. If we calculate this time by assuming maximum height (restricted by the height of the room), and neglect air friction and the release mechanism and deceleration device, then the calculations become very simple.

From Physics,

$$\Delta x = \left(\frac{1}{2}\right) \cdot a \cdot t^2$$

where Δx in this case is our maximum height (assumed to be 22 ft), a is the acceleration due to gravity (32.2 ft/s^2), and t is the time (s). Rearranging to solve for t,

$$\Delta x := 22 \cdot ft$$

$$a := 32.2 \cdot \frac{ft}{s^2}$$

$$t_{max} := \sqrt{\frac{(2 \cdot \Delta x)}{a}}$$

$$t_{max} = 1.169s$$

However, this result makes too many assumptions, most notably the one about our drop height. As of now, we don't know what this height will be, but it's almost certain that it will NOT be 22 ft. In order to determine the amount of time the rig spends in free fall, we must look at the preliminary setup (which follows below) and set up a series of equastions in order to solve for the time.

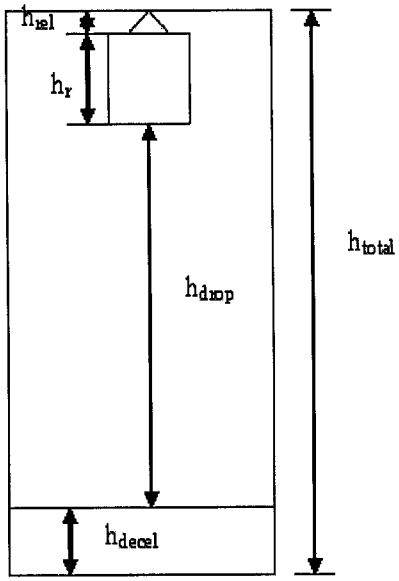

As can be seen, our Δx in this case is not the total height of the experiment (h_{total}). Instead, we must allow room for the release mechanism (h_{rel}), the deceleration device (h_{decel}), and the height of the rig itself (h_r). Our Δx then becomes the height of the drop (h_{drop}). This leaves us with the following relation.

$$h_{drop} = h_{total} - h_{rel} - h_r - h_{decel}$$

The only value we have so far is the height of the rig, which is given in NASA specs as 33 in, or 2.75 ft. However, since this may also be subject to change, we will leave it in variable form. And since h_{total} will be a concrete value deterimined by our experimental setup, that will remain in the equation as itself as well. This holds true for the height of the release mechanism. The only variable left in the above equation is the height of the deceleration device. This is also a design characteristic and needs to be calculated to ensure that the rig never exceeds 30 g's as it decelerates.

From Physics, we know that

$$v_f^2 = v_i^2 + 2 \cdot a \cdot \Delta x$$

We know that the final velocity (v_f) will be zero, since the experiment is coming to a full stop. The variable, a, in this case is not just the acceleration due to gravity. Instead, it is the acceleartion in g's. To compensate for this, we can replace a with $a*g_o$, where g_o is the amount of g's seen by the rig (this is a dimensionless number). In our case, g_o should not exceed 30, so we can treat this as an upper limit. We can also replace Δx with h_{decel}, since this is the distance over which the rig will be decelerating from it's initial speed to rest. Therefore,

$$0 = v_i^2 + 2 \cdot a \cdot g_o \cdot h_{decel}$$

Rearranging for h_{decel}

$$h_{decel} = \frac{-v_i^2}{2 \cdot a \cdot g_o}$$

We can neglect the negative sign since the intial velocity itself is negative (the rig is falling). So,

$$h_{decel} = \frac{v_i^2}{2 \cdot a \cdot g_o}$$

Now, we can use another relation to substitute in for v_i^2. This "initial velocity" is actually the final velocity of the rig at the bottom of the drop (at the distance h_{drop} from its original position). In order to determine this velocity, we can use yet another Physics relation,

$$v_i^2 = 2 \cdot a \cdot \Delta x$$

where a is the acceleration due to gravity, and Δx is our drop height, h_{drop}.

$$v_i^2 = 2 \cdot a \cdot h_{drop}$$

Substituting this value of v_i^2 into the equation for h_{decel}

$$h_{decel} = \frac{\left(2 \cdot a \cdot h_{drop}\right)}{2 \cdot a \cdot g_o}$$

The 2*a terms cancel, leaving

$$h_{decel} = \frac{h_{drop}}{g_o}$$

Now that we have a relation for h_{decel} in terms of h_{drop}, we can plug back into the governing equation.

$$h_{drop} = h_{total} - h_{rel} - h_r - \frac{h_{drop}}{g_o}$$

Rearranging to solve for h_{drop}

$$h_{drop} + \frac{h_{drop}}{g_o} = h_{total} - h_{rel} - h_r$$

$$h_{drop} \cdot \left(1 + \frac{1}{g_o}\right) = h_{total} - h_{rel} - h_r$$

$$h_{drop} = \frac{\left(h_{total} - h_{rel} - h_r\right)}{1 + \frac{1}{g_o}}$$

To solve for the time in free fall, we can use the original relation of

$$t = \sqrt{\frac{(2 \cdot \Delta x)}{a}}$$

Setting Δx equal to h_{drop}, we get

$$t = \sqrt{\frac{(2 \cdot h_{drop})}{a}}$$

A.0.2 – Preliminary Drag Shield Calculations

The following is taken directly from a MathCad Worksheet.

Drag Shield Calculations

We also need to determine if a drag shield will be required in the experiment. In order to do this several calculations must be made, and the results of individual expressions must be compared amongst themselves. To start, we first look at the FBD (free body diagram).

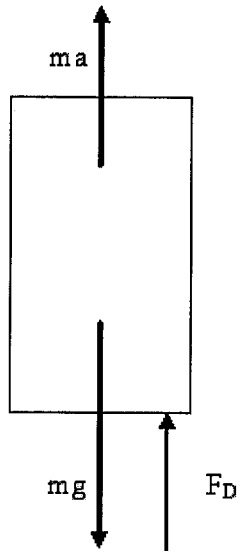

In this FBD, mg is the weight of the rig pulling it down. F_D is the drag force acting on the rig, and ma is D'Lambert's Force. The drag force is defined as

$$F_D = \left(\frac{1}{2}\right) \cdot C_D \cdot \rho \cdot A \cdot v^2$$

where C_D is the drag coefficient, ρ is the density of the air, A is the cross sectional area of the rig, and v is the rig's velocity. By definition, the velocity is just acceleration times time. So,

$$v = a \cdot t$$

$$F_D = \left(\frac{1}{2}\right) \cdot C_D \cdot \rho \cdot A \cdot (a \cdot t)^2$$

Balancing the forces (with up being positive),

$$\Sigma F_y = 0$$

$$m \cdot a + F_D - m \cdot g = 0$$

Rearranging,

$$m \cdot a = m \cdot g - F_D$$

$$a = \frac{(m \cdot g - F_D)}{m}$$

$$a = g - \frac{F_D}{m}$$

Plugging in for F_D,

$$a = g - \frac{\left[C_D \cdot \rho \cdot A \cdot (a \cdot t)^2\right]}{2 \cdot m}$$

We would like to know the acceleration in g's, rather than in actual units (m/s^2, ft/s^2). So,

$$g_o = \frac{g - \left[\frac{C_D \cdot \rho \cdot A \cdot (a \cdot t)^2}{2m}\right]}{a}$$

$$g_o = 1 - \frac{C_D \cdot \rho \cdot A \cdot a \cdot t^2}{2 \cdot m}$$

The above equations were used in determining the graph shown in Figure 5.1. The only real difference in the calculations is the drag coefficient used. For the case of the rig by itself, a drag coefficient of 1.05 was used; for one with a rounded nose, a drag coefficient of 0.85 was used.

A.0.3 – Drag Shield Calculations using Differential Equations

The following setup was used to determine the differential equations governing the drop rig/drag shield system:

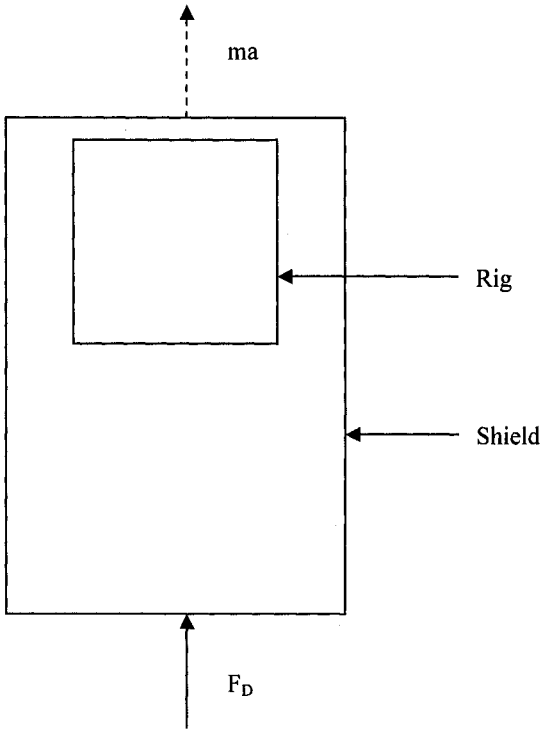

First, we take a look at the equation for the shield. Newton's Second Law states:

$$F = ma$$

The above configuration, in differential form, is:

$$m\frac{dv}{dt} + F_D - mg = 0$$

Solving for $\frac{dv}{dt}$ by dividing by m and rearranging:

$$\frac{dv}{dt} = g - \frac{F_D}{m}$$

Where

$$F_D = \frac{1}{2} C_D \rho A v^2$$

Substituting:

$$\frac{dv_{shield}}{dt} = g - \frac{\frac{1}{2} C_D \rho A v^2}{m}$$

By using the definition of a derivative, we can write the above as:

$$\frac{v_{i+1} - v_i}{\Delta t} = g - \frac{\frac{1}{2} C_D \rho A v_i^2}{m}$$

Rearranging for the v_{i+1} term:

$$v_{i+1} = v_i + \Delta t \left[g - \frac{\frac{1}{2} C_D \rho A v_i^2}{m} \right]$$

Likewise, for the shield acceleration:

$$a_{shield} = g - \frac{\frac{1}{2} C_D \rho A v^2}{m}$$

Finally, for the shield's position:

$$v = \frac{\Delta x}{\Delta t} \longrightarrow \frac{x_{i+1} - x_i}{\Delta t} = v_i$$

Leading to:

$$x_{i+1} = x_i + v_i \Delta t$$

The derivation for the rig is very similar. The governing differential equation becomes:

$$\frac{dv_{rig}}{dt} = g - \frac{\frac{1}{2} C_D \rho A v^2}{m}$$

However, in this case, $v = v_{rig} - v_{shield}$, so the final equation for the rig velocity becomes:

$$v_{i+1} = v_i + \Delta t \left[g - \frac{\frac{1}{2} C_D \rho A \left[v_{rig} - v_{shield} \right]^2}{m} \right]$$

The acceleration equation is:

$$a_{rig} = \frac{dv_{rig}}{dt}$$

And the position equation is:

$$x_{i+1} = x_i + \Delta t \left[v_{rig} - v_{shield} \right]$$

A.0.4 – Radiation Factor Calculations

For the scenario of a sphere inside a sphere, the setup is as follows (not drawn to scale):

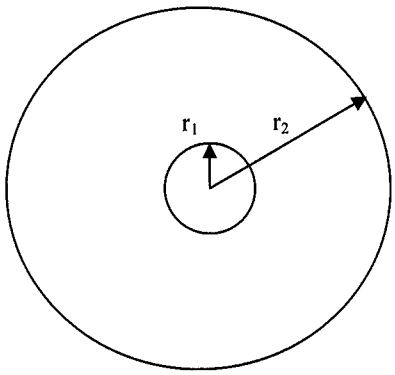

From Incropera and Dewitt [64]:

$$A_1 / A_2 = r_1^2 / r_2^2$$

$$F_{12} = 1 \qquad F_{21} = A_1 / A_2$$
$$F_{11} = 0 \qquad F_{22} = 1 - A_1 / A_2$$

And the heat exchange due to radiation is given by:

$$q_{21} = \frac{\sigma A_1 \left[T_2^4 - T_1^4\right]}{\frac{1}{\varepsilon_1} + \frac{1-\varepsilon_2}{\varepsilon_2}\left[\frac{r_1}{r_2}\right]^2}$$

For the case of a sphere inside a cylinder, the setup changes to the following (again, not drawn to scale):

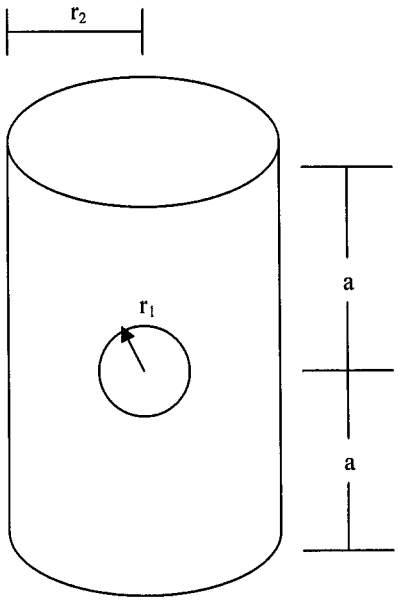

From Modest [65], the view factor of the above configuration is given by:

$$F_{12} = \frac{1}{\sqrt{1+R^2}}$$

$$R = {}^{r_2}\!/_{a}$$

The general equation for heat exchange due to radiation of an enclosed surface is [64]:

$$q_{12} = \frac{\sigma(T_1^4 - T_2^4)}{\frac{1-\varepsilon_1}{\varepsilon_1 A_1} + \frac{1}{A_1 F_{12}} + \frac{1-\varepsilon_2}{\varepsilon_2 A_2}}$$

By multiplying the entire equation by $\frac{A_1}{A_1}$, the above equation becomes:

$$q_{12} = \frac{\sigma A_1 (T_1^4 - T_2^4)}{\frac{1-\varepsilon_1}{\varepsilon_1} + \frac{1}{F_{12}} + \frac{1-\varepsilon_2}{\varepsilon_2}\left[\frac{A_1}{A_2}\right]}$$

It is now possible to substitute the appropriate areas into A_1 and A_2.

$A_1 = 4\pi r_1^2$
$A_2 = 2\pi r_2 h$, where h is the height of the cylinder ($h = 2a$)

Therefore,

$$\frac{A_1}{A_2} = \frac{2r_1^2}{r_2 h}$$

Finally, subbing this back into the radiation equation results in:

$$q_{12} = \frac{\sigma A_1 (T_1^4 - T_2^4)}{\frac{1-\varepsilon_1}{\varepsilon_1} + \frac{1}{F_{12}} + \frac{1-\varepsilon_2}{\varepsilon_2}\left[\frac{2r_1^2}{r_2 h}\right]}$$

As previously stated, σ is the Stefan-Boltzmann constant, T_1 and T_2 are the respective temperatures, F_{12} is the view factor between the surfaces, and ε_1 and ε_2 are the emissivities of the given surface.

Section A.1 – Additional Figures and Tables

A.1.1 – Droplet Emissivity of 0.90 and Furnace Emissivity of 0.3

Table A.1: Ignition delay times (in seconds) for a methanol droplet with droplet emissivity of 0.90 and furnace emissivity of 0.3. (DNI = Did Not Ignite)

Temp (K)	0.5 mm	1.0 mm	2.5 mm	5.0 mm
900	DNI	DNI	2.24	1.21
950	DNI	0.6520	0.4030	0.4240
1000	DNI*	0.2010	0.1640	0.1740
1173	0.0126	0.0137	0.0159	0.0200
1300	3.8e-3	4.0e-3	5.0e-3	7.9e-3
1500	9.0e-4	1.0e-3	1.7e-3	3.4e-3
1700	3.0e-4	4.0e-4	9.0e-4	1.9e-3
1900	1.0e-4	2.0e-4	6.0e-4	1.2e-3

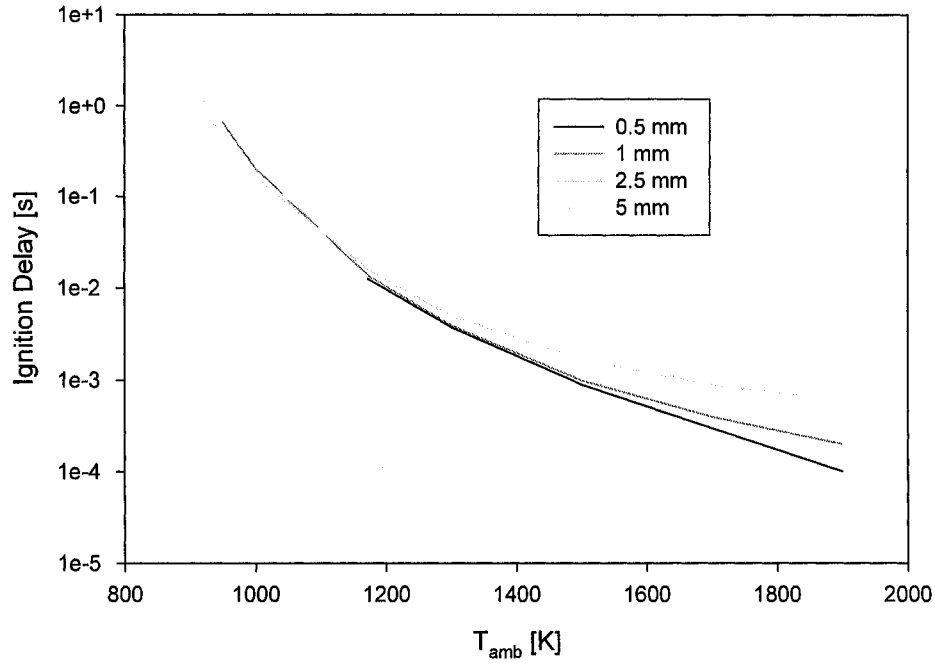

Figure A.1: Ignition delay vs. ambient temperature of 0.5 to 5.0 mm methanol droplets in air at 900 to 1900 K (Droplet emissivity of 0.90, furnace emissivity of 0.3)

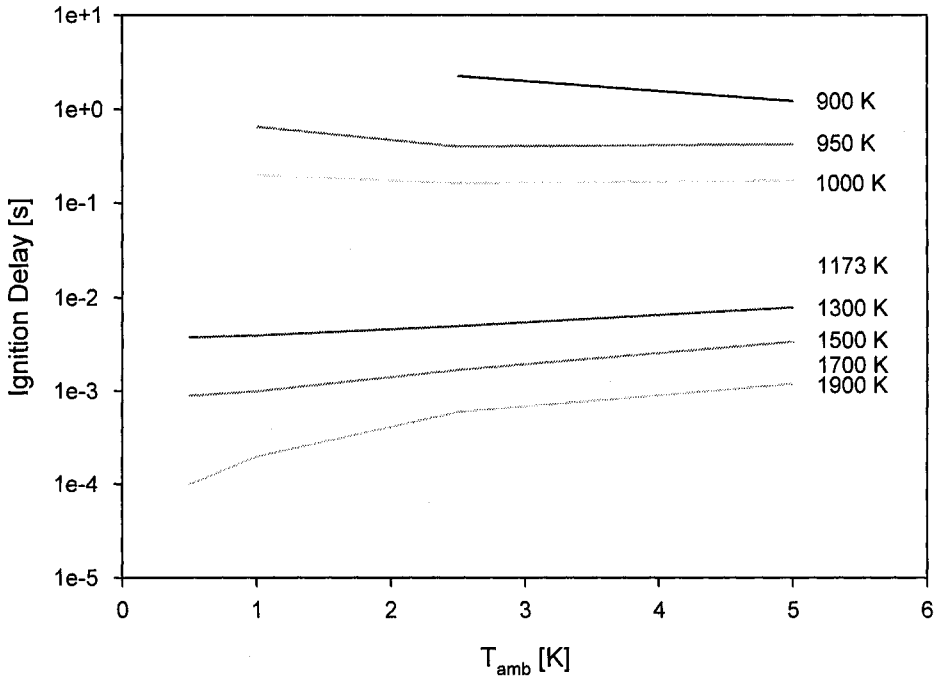

Figure A.2: Ignition delay vs. initial diameter of 0.5 to 5.0 mm methanol droplets in air at 900 to 1900 K. (Droplet emissivity of 0.90, furnace emissivity of 0.3)

A.1.2 – Droplet Emissivity of 0.90 and Furnace Emissivity of 0.2

Table A.2: Ignition delay times (in seconds) for a methanol droplet with droplet emissivity of 0.90 and furnace emissivity of 0.2. (DNI = Did Not Ignite)

Temp (K)	0.5 mm	1.0 mm	2.5 mm	5.0 mm
900	DNI	DNI	2.23	1.22
950	DNI	0.6530	0.4080	0.4310
1000	DNI*	0.2040	0.1630	0.1750
1173	0.0126	0.0137	0.0159	0.0203
1300	3.8e-3	4.0e-3	5.0e-3	7.9e-3
1500	9.0e-4	1.0e-3	1.8e-3	3.4e-3
1700	3.0e-4	4.0e-4	9.0e-4	1.9e-3
1900	1.0e-4	2.0e-4	6.0e-4	1.2e-3

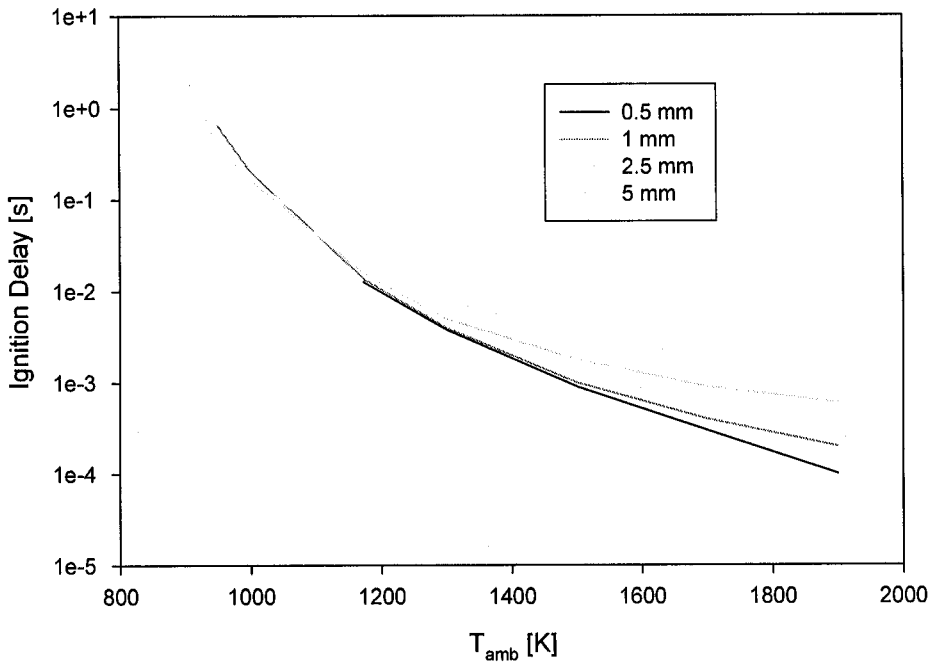

Figure A.3: Ignition delay vs. ambient temperature of 0.5 to 5.0 mm methanol droplets in air at 900 to 1900 K (Droplet emissivity of 0.90, furnace emissivity of 0.2)

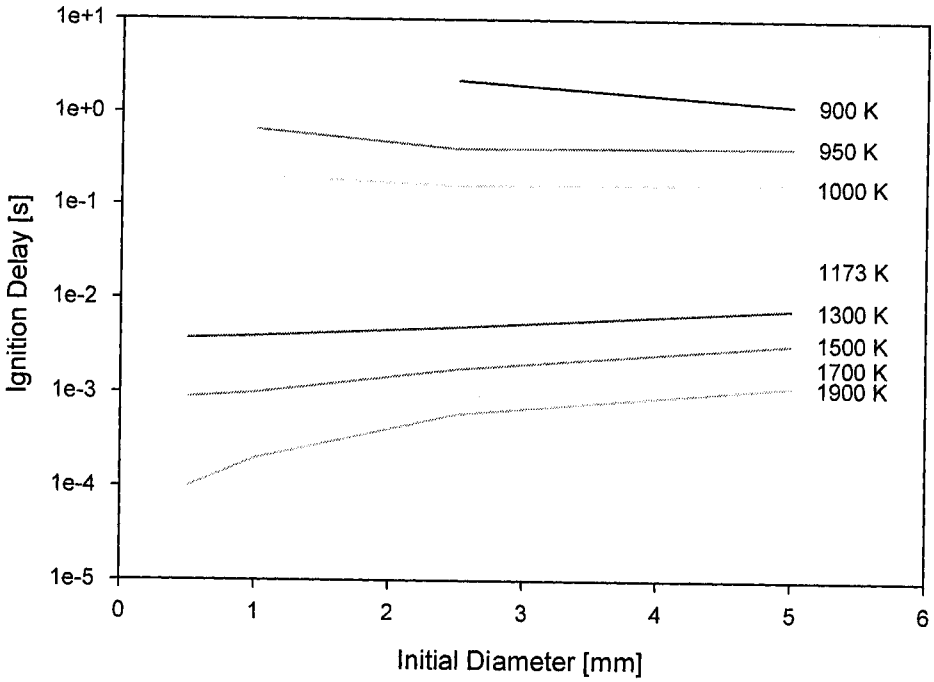

Figure A.4: Ignition delay vs. initial diameter of 0.5 to 5.0 mm methanol droplets in air at 900 to 1900 K. (Droplet emissivity of 0.90, furnace emissivity of 0.2)

A.1.3 – Droplet Emissivity of 0.90 and Furnace Emissivity of 0.05

Table A.3: Ignition delay times (in seconds) for a methanol droplet with droplet emissivity of 0.90 and furnace emissivity of 0.05. (DNI = Did Not Ignite)

Temp (K)	0.5 mm	1.0 mm	2.5 mm	5.0 mm
900	DNI	DNI	2.23	1.22
950	DNI	0.6530	0.4060	0.4290
1000	DNI*	0.2040	0.1600	0.1770
1173	0.0126	0.0137	0.0159	0.0211
1300	3.8e-3	4.0e-3	5.3e-3	7.9e-3
1500	9.0e-4	1.0e-3	1.7e-3	3.3e-3
1700	3.0e-4	4.0e-4	9.0e-4	1.9e-3
1900	4.0e-4	2.0e-4	6.0e-4	1.2e-3

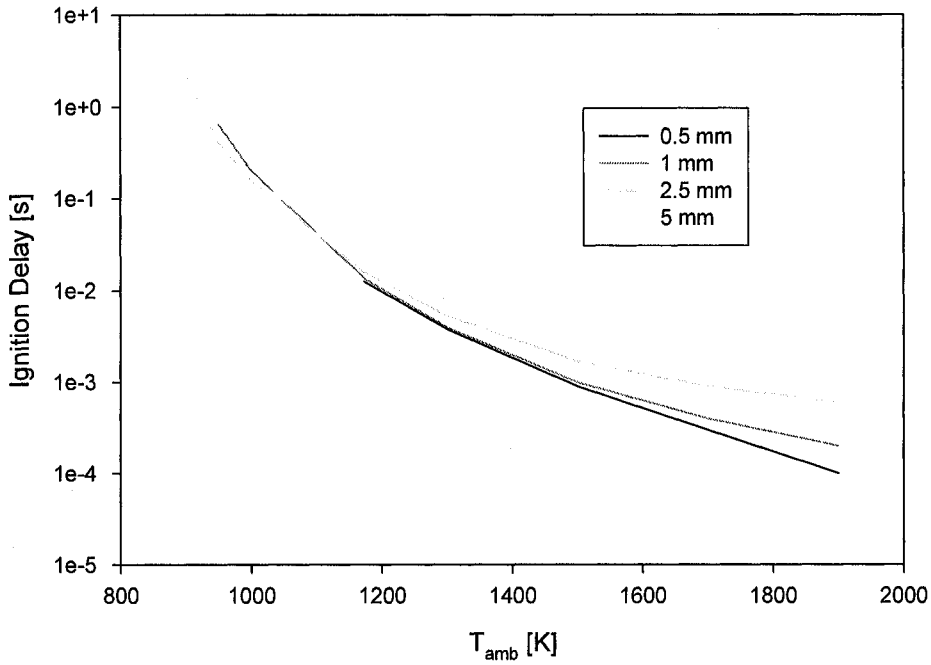

Figure A.5: Ignition delay vs. ambient temperature of 0.5 to 5.0 mm methanol droplets in air at 900 to 1900 K (Droplet emissivity of 0.90, furnace emissivity of 0.05)

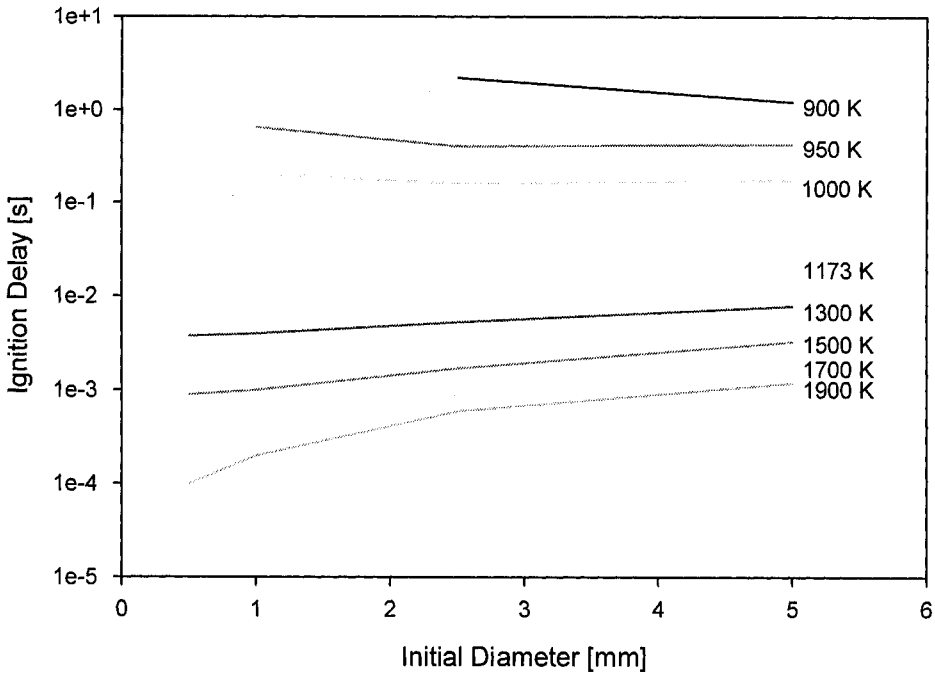

Figure A.6: Ignition delay vs. initial diameter of 0.5 to 5.0 mm methanol droplets in air at 900 to 1900 K. (Droplet emissivity of 0.90, furnace emissivity of 0.05)

A.1.4 – Numerical Model Comparison with and without Radiation

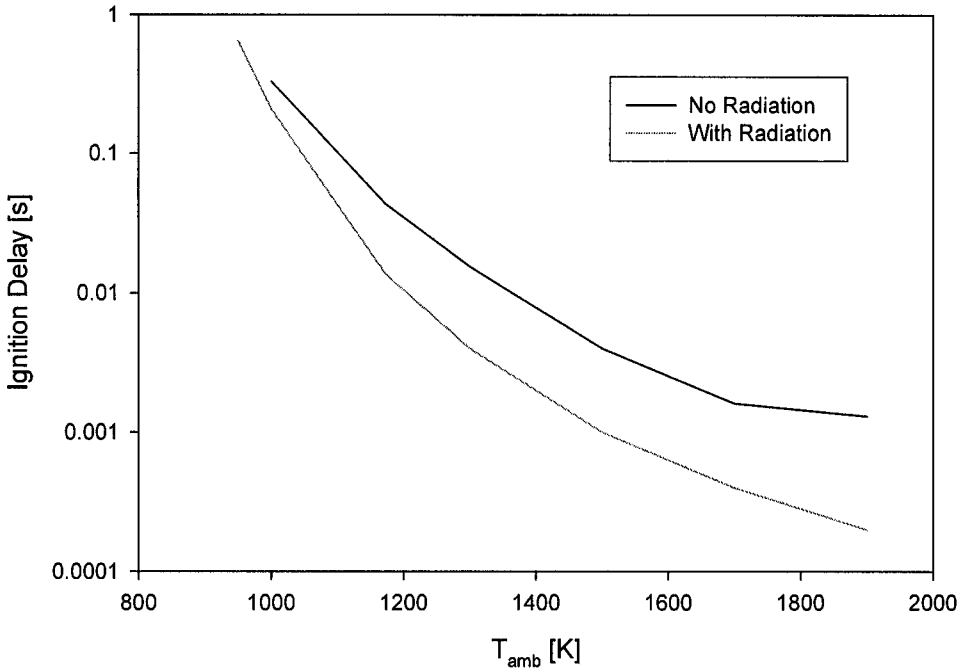

Figure A.7: Radiation effect on the ignition delay of a 1 mm methanol droplet.

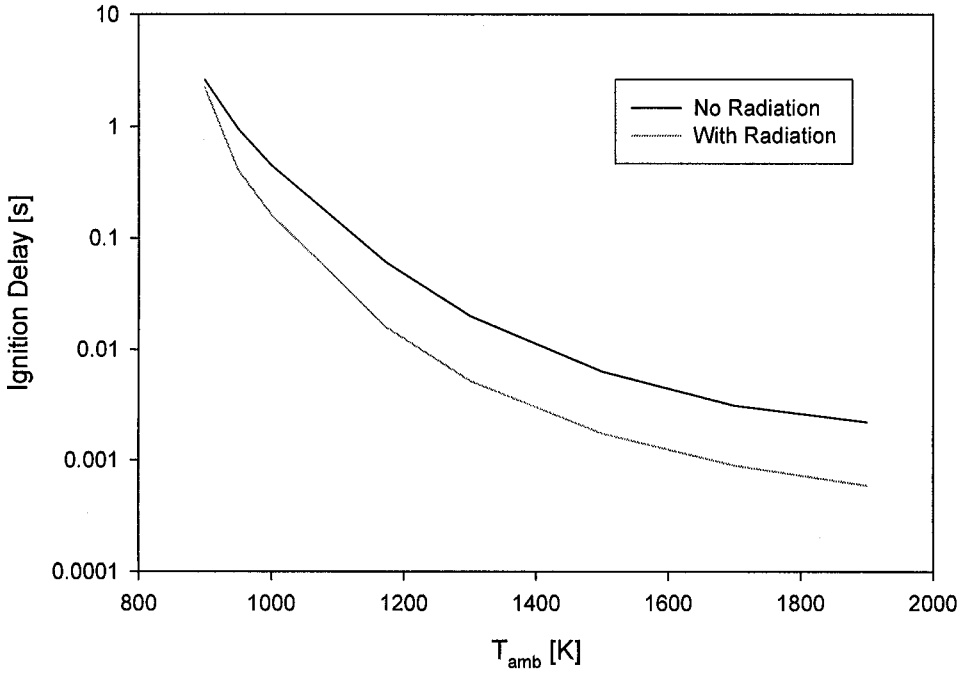

Figure A.8: Radiation effect on the ignition delay of a 2.5 mm methanol droplet.

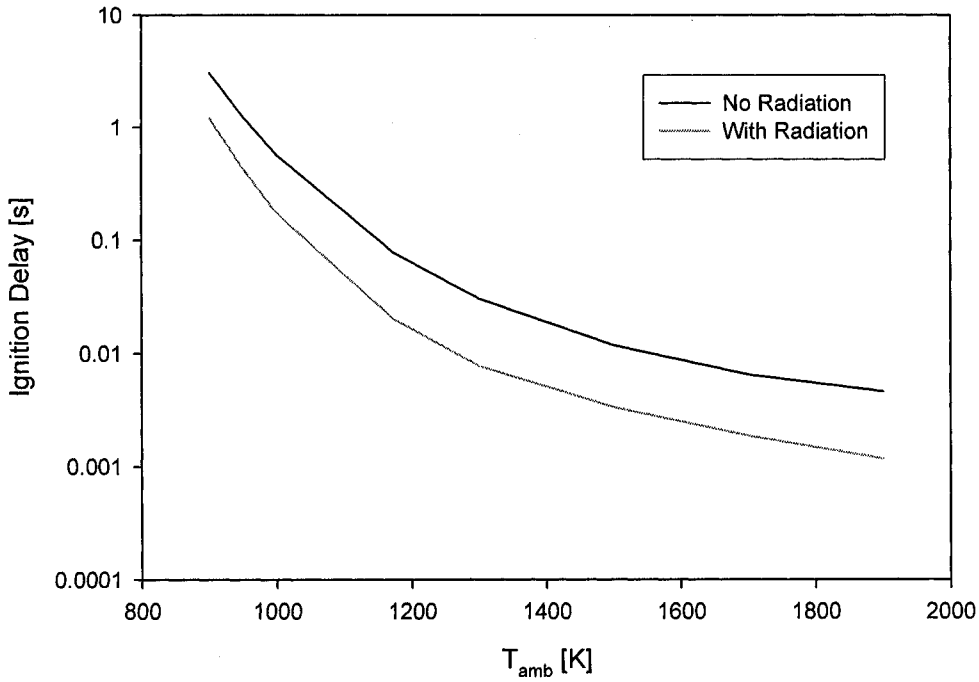

Figure A.9: Radiation effect on the ignition delay of a 5 mm methanol droplet.

Note that the above graphs are calculated using a droplet emissivity of 0.95 and a furnace emissivity of 0.5. Due to the lack of dependency on the emissivities, only one case was needed to fully describe all cases.